NTNU
Norwegian University of
Science and Technology

An Investigation of Sloshing Inside Closed Aquaculture Plants

Mona Tofte

NTNU
Norwegian University of
Science and Technology

An Investigation of Sloshing Inside

Closed Aquaculture Plants

Mona Tofte

Spring 2017

MASTER'S THESIS

Department of Marine Technology

Norwegian University of Science and Technology

Supervisor 1: Professor Trygve Kristiansen

Supervisor 2: David Kristiansen

NTNU

Norwegian University of Science and Technology

M.Sc. thesis

Spring 2017

Mona Tofte

An Investigation of Sloshing Inside Closed Aquaculture Plants

The aquaculture industry has seen extensive technological development over the last years where new fish farm cage designs have been proposed due to greater focus on environmental impact, efficiency and upscaling of the industry. To meet the growing demands, closed fish farm structures have been proposed as a solution. There are several prototypes and planned projects with closed aquaculture plants. Closing the fish farms makes it likely for the phenomenon of sloshing to occur. Sloshing affects the fish welfare, operations and requirements for structural strength.

In that regard, Professor Trygve Kristiansen of the Department of Marine Technology, NTNU, has proposed a thesis concerning the effect of sloshing inside closed fish farm plants exposed to external waves. This subject is an opportunity for the student to work on both numerical and experimental hydrodynamics. The work will involve basic experiments in Lilletanken, as well as numerical work. The waves inside and outside the structure will interact, and sloshing waves are going to be excited. Basic examples will demonstrate this. Theoretical and numerical work will then be used to quantify these effects. Potential flow theory will be assumed.

The work may be carried out in steps as follows:

- Present the governing equations and the basic theory describing the dynamics of a closed rigid aquaculture plant at sea considering two degrees of freedom assuming linear potential theory.
- Re-analyze data from the experiment conducted fall 2016 in the project thesis investigating sloshing inside a closed upright circular cylindrical fish tank subjected to regular waves.
- Create a numerical simulation of the free-surface elevation inside the closed aquaculture plant using linear modal theory assuming prescribed motions of the plant.
- Compare the numerical and experimental free-surface elevation inside the closed aquaculture plant.
- Perform a sensitivity analysis to investigate the sensitivity of the numerical calculated free-surface elevation inside the closed plant regarding the prescribed motions.
- Perform a coupled motion analysis of the given structure including sloshing.

The candidate should in his/her report give a personal contribution to the solution of the problem formulated in this text. All assumptions and conclusions should be supported by mathematical models and/or references to physical effects in a logical manner. The candidate should apply all available sources to find relevant literature and information on the actual problem. The report should be well organized and give a clear presentation of the work and all conclusions. It is important that the text is well written and that tables and figures are used to support the verbal presentation. The report should be complete, but still as short and concise as possible. The final report must contain this text, acknowledgment, summary, main body, conclusion, suggestions for future work, nomenclature, references, and appendices. All figures and tables in the main body must be identified with numbers. References should be given by author name and year in the text, and presented alphabetically by name in the reference list. In the report, it should be possible to identify the work carried out by the candidate and what has been found in the available literature or new studies given to the candidate from other authors. It is important to clearly display the references to the original source for theories and experimental results.

The report must be signed by the candidate.

 The thesis is to be submitted in DAIM.

Supervisor: Professor Trygve Kristiansen

Co-supervisor: David Kristiansen

Start: 15.01.2017

Deadline: 11.06.2017

Preface

This thesis was submitted to the Norwegian University of Science and Technology (NTNU) as a part of my Master of Science degree at the Department of Marine Technology. The work has been carried out spring 2017 in collaboration with my fellow master student, Christian Kosacki, and was a continuation of the project thesis performed fall 2016.

The idea behind the thesis was suggested by Prof. Trygve Kristiansen. The readers of this report should be familiar with basic hydrodynamics.

Trondheim, June 11, 2017

Mona Tofte

Acknowledgment

The work has been carried out under the supervison of Professor Trygve Kristiansen at the Department of Marine Technology, Norwegian University of Science and Technology (NTNU). His excellent guidance and support have been most appreciated and the present work would not have been possible without him.

I would like to thank Terje Rosten and Torgeir Wahl for their advice and help with the experiment conducted fall in 2017 in the small towing tank at NTNU. I would also like to thank Alexander Timokha for help with understanding the theory of sloshing.

Last, but not least, I would like to thank my fellow master candidate, Christian Kosacki, for his collaboration and great discussions throughout the work of this thesis.

O.N.

(MT)

Abstract

In the present work sloshing inside closed aquaculture plants at sea has been investigated by both experimental methods and linear sloshing theory.

An experiment conducted in the student towing tank at NTNU during the project thesis fall 2016 investigating sloshing inside a closed upright circular cylindrical fish tank subjected to regular waves is presented and re-analysed. Two degrees of freedom were considered in the experiment, surge and pitch.

For a closed aquaculture plant with a free-surface, the natural sloshing frequencies and corresponding natural modes are non-trivial solutions of the boundary value problem for the liquid inside the plant with zero plant excitation.

The experimental results showed that violent sloshing occurs for an incoming wave frequency which is 6.4% higher than the natural frequency of the first sloshing mode. This is due to coupling with the motions of the model. At incident wave frequency, the body-fixed response amplitude of the free-surface elevation inside the model is measured to be $3-4$ times larger than the incoming wave amplitude.

The free-surface elevation inside the cage is simulated with linear modal theory, assuming prescribed motions measured in the experiment. Comparing with the experimental free-surface elevation, the numerical results were not satisfactory. Because of unreliable measurements of the motions in the experiment, the sensitivity of the response of the numerical free-surface elevation inside the model was investigated regarding the prescribed motions. The sensitivity of the response of the numerical free-surface elevation inside the fish cage is high in the vicinity of the natural frequency of the first sloshing mode.

Based on the sensitivity analysis, corrections of the motions were made and the free-surface elevation was calculated with the new motions. The numerical and experimental free-surface elevation inside the plant do now coincide for a large frequency domain and the violent sloshing response is predicted well by the linear modal theory. Still, the experimental and numerical results do not fully agree in the vicinity of the natural frequency of the first mode.

Investigation of time series of the experimental free-surface elevation identified rotary

wave motions inside the model known as swirling. A nonlinear analysis of the experimental data was performed and showed that nonlinearities were present in the vicinity of the natural frequency of the first sloshing mode. Resonant sloshing is a highly nonlinear phenomenon and linear sloshing theory has therefore strong limitations when it comes to estimating the sloshing response in the vicinity of the natural frequency of the first sloshing mode. However, linear sloshing theory gives useful results for nonresonant sloshing.

Nomenclature

Bold Roman Letters

F   Sloshing force vector

M   Sloshing moment vector

s   Local body motion vector

U   Body velocity vector

V   Fluid velocity vector

$\mathbf{v}_0$ Translatory velocity vector of origin O

Greek Letters

β_j Modal functions used as generalized coordinates for the liquid motion

Δ Model mass displacement

η_k Tank motion in the k'th degree of freedom

$\iota_{m,i}$ Nondimensional roots of the equation $J'_m(\iota_{m,i}) = 0$

κ Spectral parameter

λ Wave length, or

       scaling factor

λ_{1m} Hydrodynamic coefficient used in the sloshing theory

λ_{2m} Hydrodynamic coefficient used in the sloshing theory

μ_m Hydrodynamic coefficient used in the sloshing theory

Ω Fluid domain

ω Angular wave frequency

ω_{n1} Natural frequency of the first sloshing mode

ω_{n2} Natural frequency of the second sloshing mode

Φ	Toal velocity potential
ρ	Fluid density
Σ	Instantaneous free-surface elevation
σ	Angular frequency
Σ_0	Mean free-surface elevation
σ_n	Natural frequency of mode n
φ	Velocity potential
φ_n	Natural sloshing mode of n'th mode
ξ	Damping coefficient
ζ	Free surface elevation
ζ_a	Incoming wave amplitude

Roman Letters

(θ, r)	Polar coordinates in the tank fixed frame
(x', y', z')	Coordinates in the Earth-fixed frame
(x, y, z)	Coordinates in the body fixed frame
A_{kj}	Added mass in k-direction due to displacement in j-direction
B_{kj}	Potential damping in k-direction due to displacement in j-direction
C_{kj}	Restoring force in k-direction due to displacement in j-direction
D_i	Inner diameter
D_o	Outer diameter
F_k^{ex}	Excitation force in k-direction
F_N	Froude number
f_w	Floater width
F_z	Sample frequency
f_z	z-position of accelerometers
F_{ML}	Pretension in mooring lines
g	Gravity
H	Wave height
h	Internal water height
J_m	Bessel function of the first kind

k	Wave number
k_s	Spring stiffness
L_z	Distance between z-accelerometers
M	Structural mass
M_l	Liquid water mass
N	Number of waves during a wave test
O	Origin of the body fixed coordinate system
O'	Origin of the Earth-fixed coordinate system
p	Fluid pressure
P'_m	Forcing amplitude
p_a	Atmospheric pressure
Q	Instantaneous tank volume
Q_0	Constant tank volume
R_0	Internal tank radius
S_0	Bondary of tank walls
S_B	Boundary of closed aquaculture plant
S_F	Boundary of free-surface
T	Wave period or,
	model draft
t	time
T_m	Natural period of sloshing mode m
u	Fluid velocity in x-direction
v	Fluid velocity in y-direction
w	Fluid velocity in z-direction

Bold Greek Letters

$\boldsymbol{\omega}$	Angular velocity vector of origin O
$\boldsymbol{\Omega}_0$	Stokes-Joukowsky potential

Contents

Chapter 1

Introduction

Norway is the largest producer of Atlantic salmon in the world (ICES, 2017). The long coast with many fjords and islands provide good locations for fish farming with the right water temperature. Still, more food is required with an expected increase in the world population and there is a large potential in increasing the marine food production. Today, the aquaculture industry in Norway is facing challenges such as sea-lice, fish escape and pollution of the surroundings. The commercial farms consist of a circular flexible floater with a net cage, to contain the fish, and moorings. Several new solutions for fish farming are suggested to meet the above-mentioned challenges. One of the suggested concepts is closed fish farms at sea. Closed fish farms is an attempt to control interactions with the environment and therefore avoid sea-lice, fish escape and pollution of the surroundings (Rosten et al., 2013). A closed system typically consists of a floater attached to a containment unit. The flexibility of the structure varies for different concepts of closed systems, depending on the structural design and choice of material. Typical materials used for the containment unit are fiberglass, concrete or a membrane material (Soltveit, 2016).

The hydrodynamical loads on closed fish cages are expected to increase compared to the forces on the commercial net pen designs. The water will no longer flow through the net, but instead meet an impermeable wall. It follows that the hydrodynamical forces go from being dominated by viscous forces to wave diffraction and mass forces (Faltinsen, 1990). Instead of a slender body, the structure is now a floating large-volume structure containing a liquid mass with a free-surface. This makes it likely for the phenomenon of *sloshing* to occur.
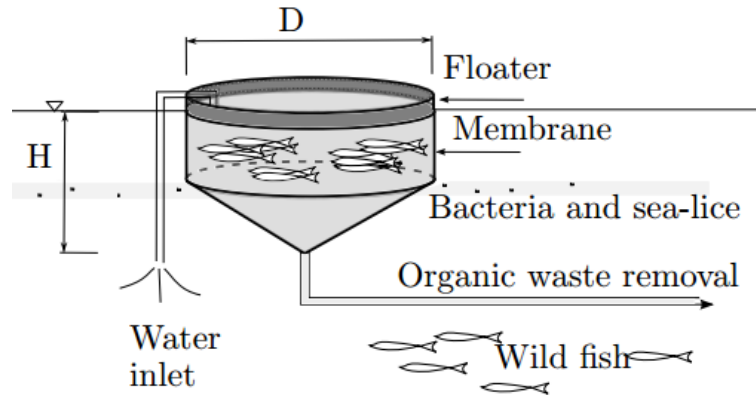
Figure 1.1: Closed flexible fish cage at sea with salmon (Strand et al., 2013).

Sloshing is movement of liquid inside another object, i.e. a tank, and can be the result of resonant excitation of the tank liquid (Faltinsen and Timokha, 2009). Sloshing must be considered for any moving structure containing a liquid with a free-surface. Sloshing can lead to significant hydrodynamical loads on the structure, which must be considered in the design process of closed fish farms. It is therefore of interest to be able to estimate the sloshing response inside closed fish farms. It is important to note that the motions of a closed fish farm at sea and internal liquid sloshing are coupled.

1.1   Background

The dynamical loads and responses for the commercial net pen designs are well known Klebert et al. (2012). For instance, Norsk standard NS9415 provides a general engineering approach for net pen systems. There are also available numerical simulation tools handling the commercial designs. The disadvantage with many simulation tools for net pen systems, is that the results rely on a simplified model of the fish net. Kristiansen and Faltinsen (2014) claims that the hydrodynamical part of the problem is often over-simplified in research of fish nets. It does not make sense to consider a sophisticated structural analysis and at the same time use an over-simplified hydrodynamic model (Kristiansen and Faltinsen, 2014).

The dynamical loads on closed aquaculture structures is not adequately known. According to Rosten et al. (2013) there is no available dynamical analysis tool for closed flexible

aquaculture systems at sea. Fredriksson et al. (2008) investigated possible procedures for designing closed containment systems. Preliminary findings from this study indicates that wave forces could be substantial and little is known about the interaction between the containment units.

Chen and Chiang (2000) performed a complete two-dimensional analysis of wave-induced fully non-linear sloshing fluid in a rigid floating tank and found the interaction between sloshing and coupling effect to be significant for the dynamics of the floating structure.

There are several prototypes and planned projects with closed aquaculture plants. In 2013 a full scale experiment with a closed flexible fish cage was conducted at Molnes by Marine Harvest (Brugrand, 2015). Large internal waves were observed during the project and the fish cage got structural damages. The design of flexible closed fish farms at sea therefore require more knowledge of the hydrodynamical loads and the response of the construction.

1.2 Objectives

The overall goal of this thesis is to investigate the effect of sloshing inside closed aquaculture plants using linear modal theory. The geometry of investigation is an upright circular cylinder with flat bottom. The main objectives of this Master's project are:

1. Present the governing equations and the basic theory describing the dynamics of a closed aquaculture plant at sea considering two degrees of freedom assuming linear potential theory.

2. Present and re-analyse an experiment investigating sloshing inside a closed upright cylindrical fish tank subjected to regular waves conducted in the student towing tank at NTNU during fall 2016.

3. Create a numerical simulation of the free-surface elevation inside the plant using linear modal theory and assuming prescribed motions of the fish cage measured in the experiment.

4. Compare the numerical and experimental results of the free-surface elevation inside the closed aquaculture plant.

5. Perform a sensitivity study to investigate the sensitivity of the numerically calculated free-surface elevation inside the closed plant regarding the prescribed motions.

6. Perform a coupled analysis of surge, pitch and sloshing for the closed aquaculture plant (Not performed in the present work).

1.3 Limitations

In the present work, linear potential flow theory of an incompressible fluid is assumed in all calculations. The free-surface inside the circular cylinder is calculated by linear modal theory assuming prescribed body motions. No complete analysis of a circular closed cage is performed in this work.

A 3D rigid upright circular cylinder with flat bottom is investigated. The work is limited to long-crested, head sea waves with no current and no wind. The model in the experiment were free to move in all six degrees of freedom, still only two degrees of freedom are considered in the present work, surge and pitch.

The model in the experiment was kept as simple as possible, as the main goal of the experiment was only to demonstrate the effect sloshing on the dynamics of the floating circular cylinder. No detailed design of the mooring system and analysis of the stability of the model are done.

1.4 Approach

The first objective is mainly covered by the two books, *Sea Loads on Ship and Offshore Structures* by Faltinsen (1990) and *Sloshing* by Faltinsen and Timokha (2009).

Next, the experiment conducted fall 2016 is presented in Chapter 3 and the raw data are re-analysed using MATLAB. The first harmonic response amplitude operators of the motions and the free-surface elevation inside the model are calculated as explained in Section 3.2.4.

The third objective is carried out by implementing modal theory assuming prescribed body motions in MATLAB. The numerical calculations are based on fourth-order Runge-Kutta method.

Now, it is possible to perform the fourth objective, the calculated free-surface elevation with prescribed motions based on the measurements in the experiment are compared with the experimental free-surface elevation inside the closed aquaculture plant. This is done by comparing the numerical and experimental response amplitude operators of the free-surface elevation inside the model. The phase difference between the numerical and experimental time series of the free-surface elevations is also investigated.

For the fifth objective, the prescribed motions are varied systematically to investigate the sensitivity of the calculated free-surface elevation regarding the prescribed motions.

The seventh objective is not performed in the present work. A suggestion of approach to cover the objective is still given. A coupled analysis of the closed aquaculture plant with two degrees of freedom is performed in the frequency domain. WADAM/WAMIT is used to analyse the outer problem, the wave radiation and diffraction problem, and modal theory evaluates the forces due to the internal liquid.

1.5   Structure of the Report

The rest of the report is organized as follows.

Chapter 2 introduces the dynamics of a closed aquaculture plant assuming linear potential theory. First, governing equations for a fluid domain are described. Coordinate systems and rigid-body motions are also defined. In the next section, linear sloshing theory is presented. The boundary value problem for a liquid containing tank is formulated and the linear natural sloshing modes for a circular upright cylindrical tank are given. Next, the sloshing response in a tank is studied with linear modal theory assuming prescribed tank motions. The forces and moments due the internal fluid are given in terms of added mass coefficients. Finally, a description of the response of a closed aquaculture plant in regular waves in the frequency domain is given.

Chapter 3 presents the experiment investigating sloshing inside a closed upright cylindrical fish tank with flat bottom subjected to regular waves conducted in the small towing tank during fall 2016. First, the test set-up is described. Second, the data processing is explained, the steps of going from raw measurements to results presented in Chapter 5. Last, a brief

discussion of error sources is given.

Chapter 4 gives a description of the approach used for the numerical calculations of the free-surface elevation inside the model and the sensitivity study of the numerical free-surface elevation regarding the prescribed motions. An explanation of the approach to find the corrections of the motions used in the numerical calculations is also given.

Chapter 5 presents the results and findings of the experiment and the numerical calculations before and after adjustments of the prescribed motions measured in the experiment have been made. This includes response amplitude operators (RAOs) of the motions, free-surface elevations and the anchoring forces.

Chapter 6 investigates the presence of swirling and nonlinearities inside the model in the experimental data.

Chapter 7 contains the conclusive summary and recommendations for further work.

Chapter 2

Theory

The aim of this chapter is to give a description of the dynamics of a closed aquaculture plant assuming linear potential theory.

First, the governing equations for evaluating fluid flow problems is given. The coordinate systems and rigid-body motions are defined. Second, a description of sloshing theory is presented. At the end, the equations of motion for a closed aquaculture plant at sea with two degrees of freedom and internal liquid are formulated and the homogenous solution investigated.

2.1   Definitions and Governing Equations

This section presents the basic assumptions and governing equations for evaluating the hydrodynamics of floating structures at sea based on potential theory. The section is based on *Sea Loads on Ship and Offshore Structures* by Faltinsen (1990). At the end, the coordinate systems and rigid-body motions are defined.

The hydrodynamics of a closed floating fish farm can be described by linear potential theory to a large extent. However, nonlinear effects are important in severe sea states. Linear theory therefore assumes small wave steepness; the waves are far from breaking. The wave-induced motions are also assumed to be linearly proportional to the wave amplitude ζ_a (Faltinsen, 1990). Potential theory means assuming incompressible, inviscid and irrotational sea water. A velocity potential, ϕ, is defined and describes the fluid velocity vector

$\mathbf{V}(x, y, z, t) = (u, v, w) = \nabla\phi$ at point (x, y, z) at time t. The vorticity vector is defined as the curl of the velocity vector $\boldsymbol{\omega} = \nabla \times \mathbf{V} = curl(\mathbf{V})$. If the vorticity in fluid flow is zero, fluid particles are not rotating and the flow in that region is called irrotational (Cengel and Cimbala, 2010). Since the water is incompressible, the continuity equation which expresses mass conservation is $\nabla \cdot \mathbf{V} = 0$. Combining the continuity equation and the definition of the velocity potential gives the Laplace equation.

$$\frac{\partial^2 \phi}{\partial x^2} + \frac{\partial^2 \phi}{\partial y^2} + \frac{\partial^2 \phi}{\partial z^2} = 0 \tag{2.1}$$

The velocity potential must satisfy the Laplace equation over the entire fluid domain, Ω, and relevant boundary conditions. This is a boundary value problem for the velocity potential ϕ and is illustrated in Figure 2.1. The goal of the analysis is to find ϕ, which is a solution of the Laplace equation and satisfies the boundary conditions. If ϕ is known, the flow problem is solved and the fluid pressure, p, is given by the Bernoulli equation (2.2). Assuming vertical z-axis to be positive upwards gives

$$p + \rho g z + \rho \frac{\partial \phi}{\partial t} + \frac{\rho}{2} \mathbf{V} \cdot \mathbf{V} = C \tag{2.2}$$

where C is a constant and Φ is time dependent fluid potential. The Bernoulli equation is true for unsteady, incompressible and inviscid flow.
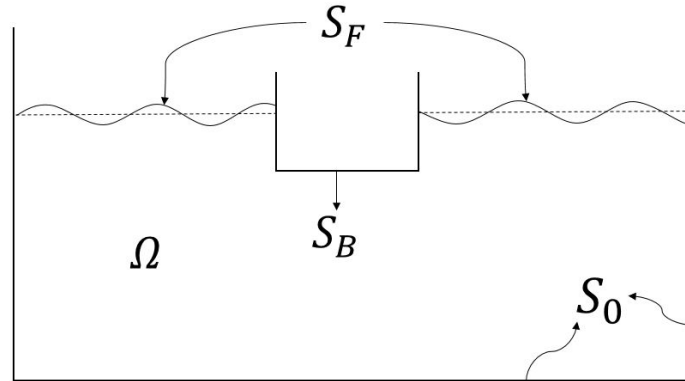

Figure 2.1: The figure gives an overview of the tank control surface, containing the liquid domain, Ω, and its boundaries. The boundaries are divided into tank walls, body boundary and the free-surface, denoted S_0, S_B and S_F respectively

The boundary conditions are criteria for the velocity potential along the boundaries of the investigated fluid domain Ω. First, we have the kinematic boundary condition, which expresses impermeability (Faltinsen, 1990). This means that there can be no fluid flow through a body surface or a wall. For a fixed body in a moving fluid is the body boundary condition

$$\frac{\partial \phi}{\partial n} = 0 \qquad (2.3)$$

on the body surface, S_B. Here are n the normal to the body surface defined positive pointing into the fluid domain. For a moving body with velocity $\mathbf{U}$ is the kinematic boundary condition generalized to

$$\frac{\partial \phi}{\partial n} = \mathbf{U} \cdot \mathbf{n} \qquad (2.4)$$

on S_B. $\mathbf{U}$ can have both translatory and rotary motion effects and can vary for different locations on the body. The kinematic boundary condition for the free-surface is given by assuming that a fluid particle on the free-surface stays on the free-surface (Faltinsen, 1990). The free-surface is defined by $z = \zeta(x, y, t)$. The kinematic free-surface condition is then

$$\frac{\partial \zeta}{\partial t} + \frac{\partial \phi}{\partial x}\frac{\partial \zeta}{\partial x} + \frac{\partial \phi}{\partial y}\frac{\partial \zeta}{\partial y} - \frac{\partial \phi}{\partial z} = 0 \quad \text{on } z = \zeta(x, y, t). \qquad (2.5)$$

In addition to the kinematic condition is there also a dynamic condition for the free-surface. The dynamic free-surface condition is that the fluid pressure is equal to the constant atmospheric pressure p_0 on the free-surface (Faltinsen, 1990). Inserting $C = p_0/\rho$ and the definition of the velocity potential, $V = \nabla \cdot \Phi$, into Equation (2.2) gives

$$g\zeta + \frac{\partial \phi}{\partial t} + \frac{1}{2}\left(\left(\frac{\partial \phi}{\partial x}\right)^2 + \left(\frac{\partial \phi}{\partial y}\right)^2 + \left(\frac{\partial \phi}{\partial z}\right)^2\right) = 0 \quad \text{on } z = \zeta(x, y, t) \qquad (2.6)$$

for fluid with no motion. Both the kinematic and dynamic free-surface conditions in Equation (2.5) and (2.6) are non-linear. Assuming linear theory and no forward speed of the structure or current in the flow gives the linearized free-surface conditions

$$\frac{\partial \zeta}{\partial t} - \frac{\partial \phi}{\partial z} = 0 \quad \text{on } z = 0 \quad \text{(kinematic)} \tag{2.7}$$

$$g\zeta + \frac{\partial \phi}{\partial t} = 0 \quad \text{on } z = 0 \quad \text{(dynamic)} \tag{2.8}$$

Combining the kinematic and dynamic free-surface conditions gives one final condition for the free-surface

$$\frac{\partial^2 \phi}{\partial t^2} + g\frac{\partial \phi}{\partial z} = 0 \quad \text{on } z = 0 \tag{2.9}$$

Before going into further details, the coordinate systems and rigid-body motion modes are defined. A right-handed Earth-fixed inertial coordinate system (x, y, z) with positive z-axis pointing upwards is defined, with $z = 0$ at the undisturbed free surface. This system is denoted $O'x'y'z'$. In addition, a body-fixed coordinate system, denoted $Oxyz$, is defined that coincide with the inertial coordinate system if the body does not move.

Surge, sway and heave are defined as translatory motions of the origin the of body-fixed coordinate system along the x-, y- and z-axis in the inertial coordinate system (Faltinsen and Timokha, 2009). Roll, pitch and yaw are rotations about the same axes and are defined positive according to the right-hand rule, see Figure 2.2. The six body motions are denoted η_k for $k = 1, ...6$. The longitudinal and vertical motions of a point P on the body can be expressed in the inertial coordinate system.

$$\mathbf{s} = (\eta_1 + z\eta_5 - y\eta_6)\mathbf{i} + (\eta_2 - z\eta_4 + x\eta_6)\mathbf{j} + (\eta_3 + y\eta_5 - x\eta_5)\mathbf{k} \tag{2.10}$$

Here are $\mathbf{i}$, $\mathbf{j}$ and $\mathbf{k}$ unit vectors along the x-, y- and z-axis, respectively.
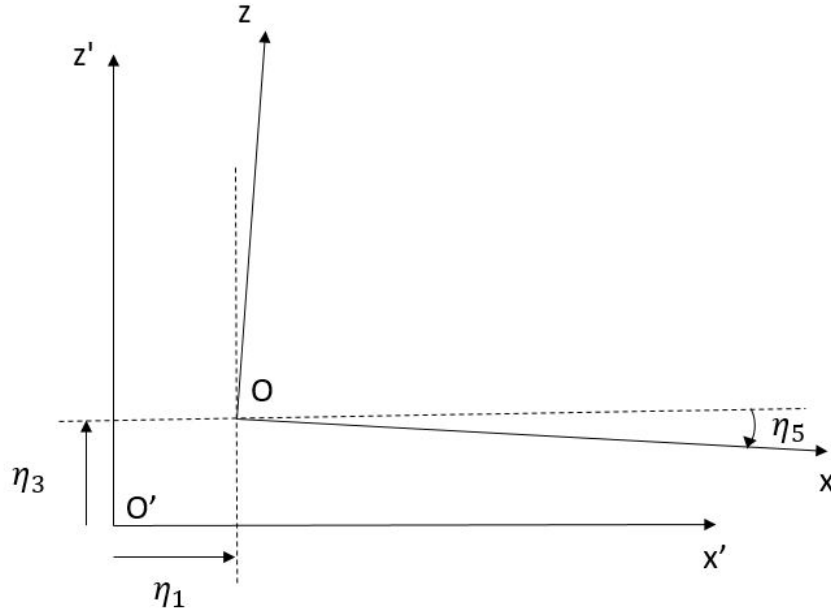
Figure 2.2: Earth- and body-fixed coordinate systems denoted $O'x'y'z'$ and $Oxyz$ respectively (Faltinsen and Timokha, 2009).

2.2   Sloshing

Sloshing is internal waves occurring inside any moving structure containing a liquid with a free-surface and can be the result of resonant excitation of the tank liquid. This section gives an overview of linear sloshing theory. The present section is based on chapter *4 Linear Natural Sloshing Modes* and *5 Linear Modal Theory* in *Sloshing* by Faltinsen and Timokha (2009).

First, the natural sloshing frequencies and modes for a circular cylinder with flat bottom are found. Next, the response of the free-surface elevation inside tanks due to forced motions is mathematically described using linear modal theory. The forces and moments due to sloshing are calculated and given in the frequency-domain.

2.2.1   Linear Natural Sloshing Modes

This section describes how to find the natural sloshing frequencies and modes assuming potential theory. The lowest natural frequency indicates when significant sloshing is expected. For a water tank with a free-surface, the natural sloshing frequencies and corresponding natu-

ral modes are non-trivial solutions for the boundary value problem with zero tank excitation. The natural sloshing modes are a geometric description of the wave components contributing to the free-surface inside the tank.

The boundary value problem for the velocity potential in a liquid containing body is illustrated in Figure 2.3. The problem is linearized by assuming small surface elevations compared to characteristic tank length. In Figure 2.3 are Σ_0 the mean free-surface, Q_0 the tank volume and S_0 the tank surface. With no tank excitation, the velocity potential, ϕ inside the tank must satisfy $\partial\phi/\partial n = 0$ on S_0, where n is the outer normal to S_0. The Laplace equation must be satisfied in the entire fluid domain.
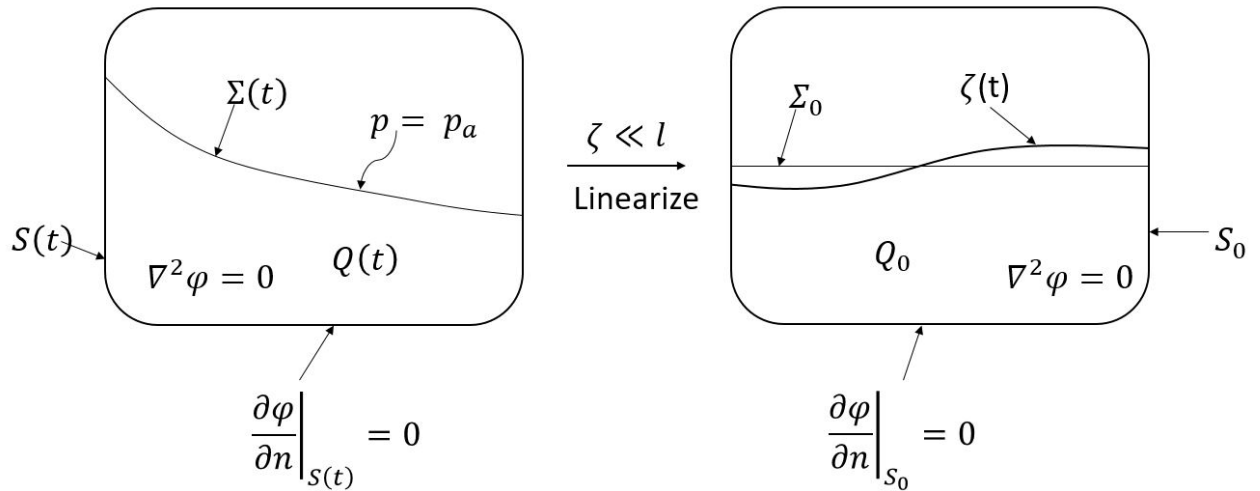
Figure 2.3: Nonlinear problem to the left and linearized boundary value problem to the right. The problem is linearized by assuming small surface elevations compared to characteristic tank length (Kristiansen, 2016).

The mean free-surface must satisfy the kinematic and dynamic free-surface conditions given in Equation (2.9). Constant liquid volume is also required and is expressed as $\int_{\Sigma_0} \zeta \, dxdy = 0$, where $\zeta = \zeta(x,y,t)$ determines the free-surface elevation in the tank. The solution of the linearized boundary value problem in Figure 2.3 can be expressed as time-periodic solutions with circular frequency σ, see Equation (2.11).

$$\phi(x,y,z,t) = \varphi(x,y,z)e^{i\sigma t} \tag{2.11}$$

Inserting Equation (2.11) into the linear sloshing problem and combining the kinematic and dynamic free-surface condition gives the spectral boundary problem defined in Equation (2.12).

There are four equations which define the spectral problem. Laplace equation must be satisfied over the entire fluid domain to ensure conservation of mass. The next requirement is no fluid flow through the tank walls defined by S_0. Combined dynamic and kinematic boundary condition must be satisfied on the mean free-surface, Σ_0. The last equation in (2.12) follows from global conservation of liquid mass in the tank.

$$
\begin{aligned}
\nabla^2 \varphi &= 0 && \text{in } Q_0 \\
\frac{\partial \varphi}{\partial n} &= 0 && \text{on } S_0 \\
\frac{\partial \varphi}{\partial z} &= \kappa \varphi && \text{on } \Sigma_0 \\
\int_{\Sigma_0} \varphi \, dx dy &= 0
\end{aligned}
\tag{2.12}
$$

With the spectral parameter, κ, in the expression for the boundary condition for the mean free-surface. Here is $\kappa = \sigma^2/g$. The system of equations in (2.12) is a homogenous problem. There exists an infinite set of *natural modes*, $\varphi_n(x, y, z)$, and corresponding *natural frequencies*, $\sigma_n = \sqrt{g\kappa_n}$ for $n = 1, 2, 3...$, which are solutions to the spectral problem given in Equation (2.12).

Let's now investigate the natural modes and eigenfrequencies of an upright circular cylindrical tank. The spectral problem for a vertical cylindrical tank is best studied in cylindrical coordinates (r, θ, z). The spectral problem in Equation (2.12) in cylindrical coordinates is given in Equation (2.13). The geometry of the cylinder is defined in Figure 2.4. Here are R_0 the internal tank radius and h the internal liquid height.
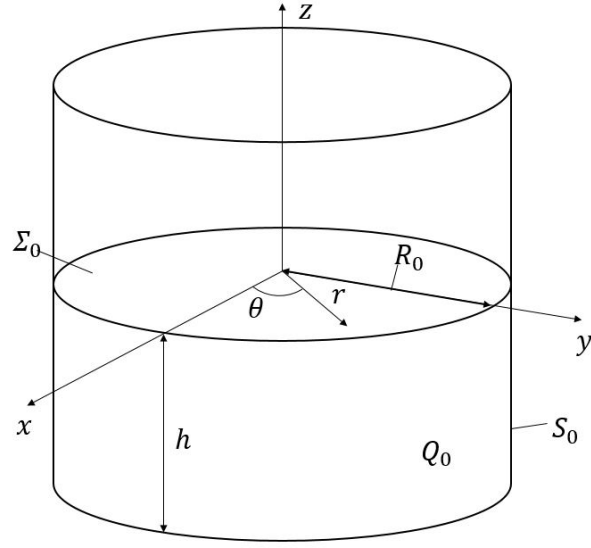
Figure 2.4: Geometry of circular cylinder with flat bottom.

$$\frac{\partial^2 \varphi}{\partial z^2} + \frac{1}{r}\frac{\partial}{\partial r}\left(r\frac{\partial \varphi}{\partial r}\right) + \frac{1}{r^2}\frac{\partial^2 \varphi}{\partial \theta^2} = 0, \qquad 0 \leq r \leq R_0, \qquad -h < z < R_0, \qquad 0 \leq \theta \leq 2\pi$$

$$\frac{\partial \varphi}{\partial r} = 0, \qquad\qquad\qquad\qquad r = R_0, \qquad -h < z < R_0, \qquad 0 \leq \theta \leq 2\pi$$

$$\frac{\partial \varphi}{\partial z} = 0, \qquad\qquad\qquad\qquad r \leq R_0, \qquad z = -h, \qquad 0 \leq \theta \leq 2\pi$$

$$\frac{\partial \varphi}{\partial z} = \kappa\varphi, \qquad\qquad\qquad\qquad r \leq R_0, \qquad z = 0, \qquad 0 \leq \theta \leq 2\pi$$

$$\int_0^{R_0} r \int_0^{2\pi} \varphi(r,\theta,0)d\theta dr = 0.$$

$$(2.13)$$

The boundary value problem defined in Equation (2.13) is solved using separation of variables. Separation of variables are possible due to a simple tank geometry. The solution for the velocity potential is expressed as $\varphi = R(r)\Theta(\theta)Z(z)$ and is inserted into Laplace's equation. The solution is then found by utilizing the boundary conditions.

The solution of the velocity potential defines the natural modes, φ_m, which are given in Equation (2.14). For a circular cylindrical tank the natural solutions of the Laplace equation contain Bessel functions, J_m.

$$\varphi_{m,i}(r,\theta,z) = J_m\left(\iota_{m,i}\frac{r}{R_0}\right)\frac{cosh(\iota_{m,i}(z+h)/R_0)}{cosh(\iota_{m,i}h/R_0)} \times \begin{cases} cos(m\theta) \\ \\ sin(m\theta) \end{cases} \qquad m = 0,1,...\quad i = 1,2,...$$

(2.14)

Here J_m are Bessel functions of the first kind and $\iota_{m,i}$ nondimensional roots of the equation $J'_m(\iota_{m,i}) = 0$. An infinite set of these roots exists for every mode, m. The index i enumerates the roots in ascending order. The surface wave patterns of the natural modes in Equation (2.14) are defined as

$$f_{m,i}(r,\theta) = \varphi_{m,i}(r,\theta,z=0) = J_m\left(\iota_{m,i}\frac{r}{R_0}\right) \times \begin{cases} cos(m\theta) \\ \\ sin(m\theta) \end{cases} \qquad m = 0,1,...\quad i = 1,2,...$$

(2.15)

The corresponding natural frequencies and periods of the sloshing modes are:

$$\sigma_{m,i}^2 R_0/g = R_0\kappa_{m,i} = \iota_{m,i}tanh(\iota_{m,i}h/R_0)$$

(2.16)

$$T_{m,i} = \frac{2\pi}{\sqrt{g\iota_{m,i}tanh(\iota_{m,i}h/R_0)/R_0}}$$

(2.17)

2.2.2 Linear Modal Theory

In linear modal theory the response of the free-surface elevation in tanks due to forced motions is studied. This section aims to give a presentation of the basic assumptions and equations in linear modal theory. First a presentation of the governing equations for the sloshing problem with prescribed rigid body motions is given. Second, the forces and moments due to sloshing are presented and how these can be represented in a frequency domain analysis. Finally, the sloshing problem for a circular cylindrical tank is described.

When sloshing in a tank is studied, it is most convenient to operate with a tank-fixed coordinate system. In Section 2.1, the rigid body motions and two coordinate systems were defined. A tank-fixed and Earth-fixed coordinate system were introduced, denoted respec-

tively as $Oxyz$ and $O'x'y'z'$. The translations and rotations of the tank are denoted η_k for all six degrees of freedom, $k = 1, ...6$. Translatory and angular motions of the tank are now defined in Equation (2.18) and (2.19).

$$\begin{aligned} \mathbf{v_0} &= v_{01}(t) \cdot \mathbf{e_1}(t) + v_{02} \cdot \mathbf{e_2} + v_{03}(t) \cdot \mathbf{e_3} \\ &= \dot{\eta}_1 \mathbf{e_1}(t) + \dot{\eta}_2 \mathbf{e_2}(t) + \dot{\eta}_3 \mathbf{e_3}(t) \end{aligned} \tag{2.18}$$

$$\begin{aligned} \boldsymbol{\omega} &= \omega_1(t) \cdot \mathbf{e_1}(t) + \omega_2 \cdot \mathbf{e_2} + \omega_3(t) \cdot \mathbf{e_3} \\ &= \dot{\eta}_4 \mathbf{e_1}(t) + \dot{\eta}_5 \mathbf{e_2}(t) + \dot{\eta}_6 \mathbf{e_3}(t) \end{aligned} \tag{2.19}$$

Assume a tank with prescribed motions η_k where $k = 1, ...6$. Now, the boundaries defined in the spectral problem, see Equation (2.13), needs to be modified such that they satisfy the prescribed tank motions η_k. The boundary value problem including prescribed tank motions then becomes

$$\begin{aligned} \frac{\partial^2 \Phi}{\partial x^2} + \frac{\partial^2 \Phi}{\partial y^2} + \frac{\partial^2 \Phi}{\partial z^2} &= 0 \qquad \text{in } Q_0 \\ \left. \frac{\partial \Phi}{\partial n} \right|_{S_0} &= (\mathbf{v_0} + \boldsymbol{\omega} \times \mathbf{r}) \cdot n = \mathbf{v_0} \cdot n + \boldsymbol{\omega} \cdot (\mathbf{r} \times \mathbf{n}) \\ \left. \frac{\partial \Phi}{\partial n} \right|_{\Sigma_0} &= \mathbf{v_0} \cdot \mathbf{n} + \boldsymbol{\omega} \cdot (\mathbf{r} \times \mathbf{n}) + \frac{\partial \zeta}{\partial t} \\ \left. \frac{\partial \Phi}{\partial t} \right|_{\Sigma_0} &- g_1 x - g_2 y - g_3 \zeta = 0 \\ \int_{\Sigma_0} \zeta \, dx dy &= 0. \end{aligned} \tag{2.20}$$

The free-surface elevation in the tank can be expressed by a Fourier series, see Equation (2.21). Since the Laplace equation is linear, the superposition principle applies. The velocity potential, ϕ, in Equation (2.22) is therefore decomposed into three parts, translation, rotation and the homogenous solution of the spectral problem.

$$\zeta(x, y, t) = \sum_{i=1}^{\infty} \beta_i(t) \varphi_i(x, y, 0) = \sum_{i=1}^{\infty} \beta_i(t) f_i(x, y) \tag{2.21}$$

$$\Phi(x, y, z, t) = \mathbf{v_0}(t) \cdot \mathbf{r} + \boldsymbol{\omega}(t) \cdot \boldsymbol{\Omega}_0(x, y, z) + \sum_{i=1}^{\infty} R_i(t) \varphi_i(x, y, z) \tag{2.22}$$

Where φ_i are the natural sloshing modes defined by the eigenvalue problem (2.14) for a cylindrical tank. $\boldsymbol{\Omega}_0(x, y, z)$ is the Stokes-Joukowsky potential and is connected to rotational motions of the tank. $\beta_i(t)$ are time-dependent *modal functions* and controls the contribution of each natural mode i in the free-surface elevation. Substitution of the free-surface elevation and velocity potential stated in Equation (2.21) and (2.22), into the kinematic free-surface condition in Equation (2.20) gives the relation:

$$\dot{\beta}_j = \kappa_j R_j \quad \text{for } j \geq 1 \tag{2.23}$$

Due to Equation (2.23), it is sufficient to use β_j as generalized coordinates for liquid motion inside the tank. Finally utilizing the dynamic free-surface condition in boundary value problem (2.20) gives an infinite set of uncoupled linear differential equations for the generalized coordinates β_j, see Equation (2.24). These are called *linear modal equations.*

$$\ddot{\beta}_m + \sigma_m^2 \beta_m = K_m(t), \qquad m = 1, 2, ... \tag{2.24}$$

This is a set of second order differential equations which can be solved numerically using Runge-Kutta 4th order scheme or other appropriate schemes. The right-hand side is prescribed as

$$K_m(t) = -\frac{\lambda_{1m}}{\mu_m}(\ddot{\eta}_1(t) - g\eta_5(t)) - \frac{\lambda_{2m}}{\mu_m}(\ddot{\eta}_2(t) + g\eta_4(t)) - \sum_{k=4}^{6} \frac{\ddot{\eta}_k(t)\lambda_{0(k-3)m}}{\mu_m} \quad m = 1, 2, ... \tag{2.25}$$

Here λ_{1m}, λ_{2m}, μ_m and $\lambda_{0(k-3)m}$ for $k = \{4, 5, 6\}$ are a set of hydrodynamic coefficients which are independent of time. Computation of these need the natural sloshing modes and the Stokes-Joukowski potential:

$$\sigma_m^2 = g\kappa_m$$

$$\mu_m = \frac{\rho}{\kappa_m} \int_{\Sigma_0} \varphi_m^2 \, dx \, dy$$

$$\lambda_{1m} = \rho \int_{\Sigma_0} f_m x \, dx \, dy \tag{2.26}$$

$$\lambda_{2m} = \rho \int_{\Sigma_0} f_m y \, dx \, dy$$

$$\lambda_{0km} = \rho \int_{\Sigma_0} f_m \Omega_{0k} \, dx \, dy, \quad k = 1, 2, 3; \quad m = 1, 2...$$

An example of a solution of Equation (2.24), linear modal equation, is given below for a tank with natural sloshing frequency σ_m. If damping is neglected and the forcing harmonic, $K_m(t) = \sigma^2 P'_m cos(\sigma t)$, with a forcing frequency $\sigma \neq \sigma_m$, will the solution of Equation (2.24) never reach the steady-state solution. For zero initial conditions, $\beta_m(0) = \dot{\beta}_m(0) = 0$ are the solution of Equation (2.24):

$$\beta_m(t) = \frac{P'_m \sigma^2}{\sigma_m^2 - \sigma^2}(cos(\sigma t) - cos(\sigma_m t)) \tag{2.27}$$

This results in a phenomenon called beating. Beating is characterized by larger maximum magnitudes with respect to those in steady-state regimes and a beating period, T_b. $\sigma \to \sigma_m$ causes an infinite beating period. Figure 2.5 shows the beating oscillations for the solution given in Equation (2.27). The solution is calculated by re-writing the linear modal equation into a system of 1. order differential equations. The system of equations is then implemented into MATLAB and solved with the built-in MATLAB function, *ode45.m*. Zero initial conditions are applied.
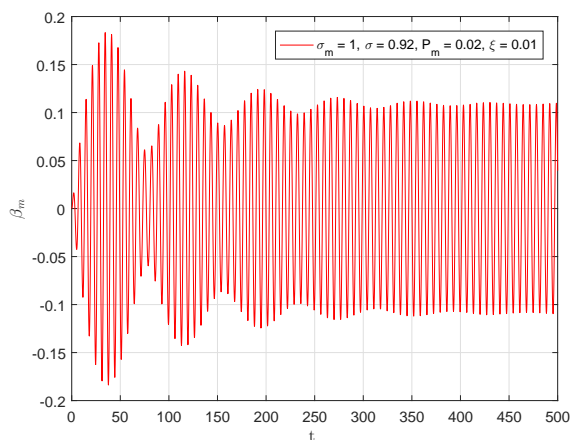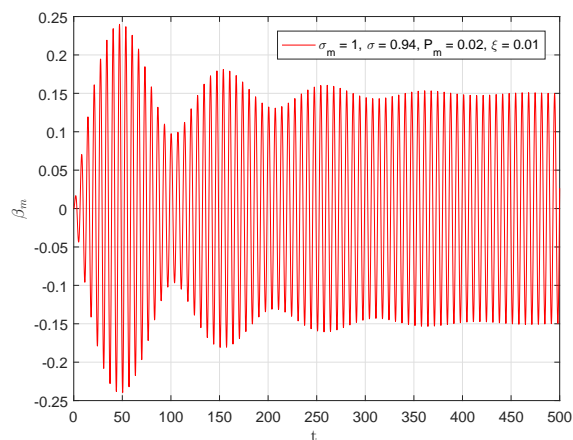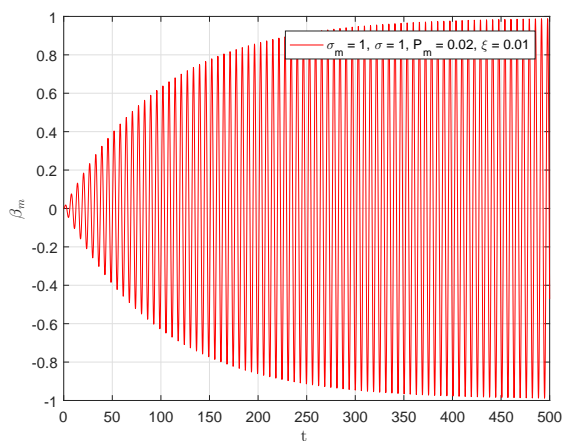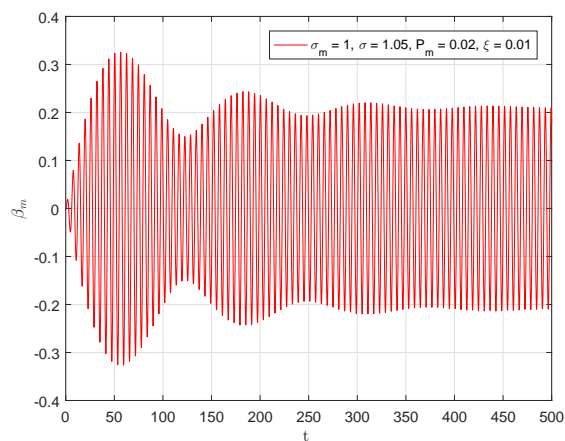
(a) $\sigma = 0.92$

(b) $\sigma = 0.94$

(c) $\sigma = 1.0$

(d) $\sigma = 1.05$
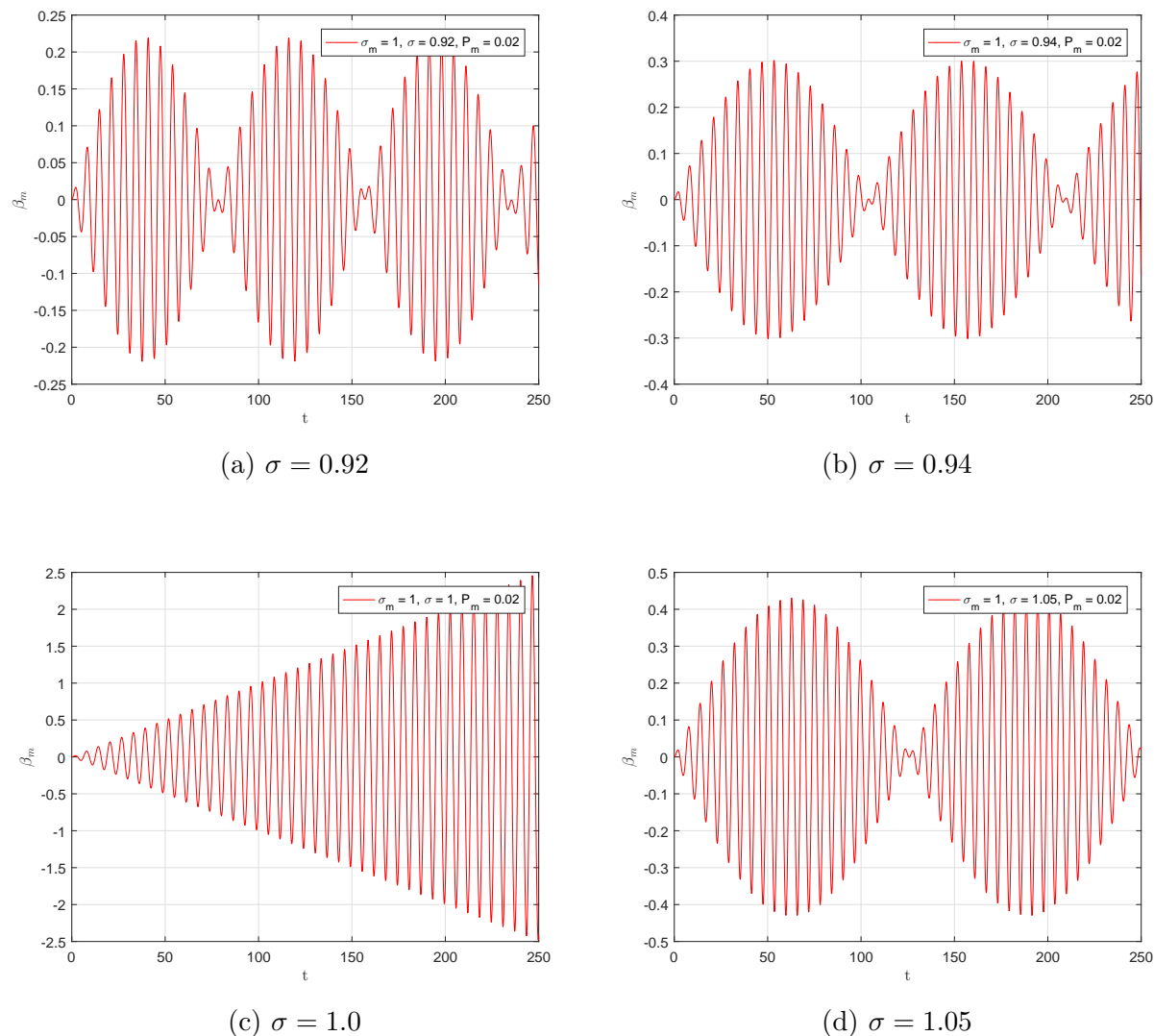
Figure 2.5: Numerical solution of the modal equations (2.24) with harmonic forcing with frequency σ, zero initial conditions, $P'_m = 0.02$ and resonance frequency σ_m found using *ode.45* in MATLAB. Beating oscillations of the generalized coordinates β_m occur.

In reality the liquid motion will be damped due to viscous effects, such as boundary-layer flow along the wetted tank surface and flow separation due to interior structures. Nonlinear effects such as breaking waves can also cause considerable damping. Damping can be accounted for by introducing the term, $2\xi\sigma_m\dot{\beta}_m$, to Equation (2.24):

$$\ddot{\beta}_m + 2\xi\sigma_m\dot{\beta}_m + \sigma_m^2\beta_m = K_m(t), \qquad m = 1, 2, ... \tag{2.28}$$

Equation (2.28) does not satisfy the free-surface condition, Equation (2.9), but Equation (2.28) is a simple way to account for damping and simulates the physical effects well. Figure 2.6 is the same as the abovementioned example presented in Figure 2.5, but now also with damping. The figure shows how the beating oscillations of the generalized coordinates β_m die out and stabilizes approximately at $t = 500$. For larger damping coefficients, ξ, the generalized coordinates stabilizes earlier.

(a) $\sigma = 0.92$

(b) $\sigma = 0.94$

(c) $\sigma = 1.0$

(d) $\sigma = 1.05$

Figure 2.6: Numerical solution of the modal equations (2.28), including damping term $2\xi\sigma_m\dot{\beta}_m$, with harmonic forcing with frequency σ, zero initial conditions, $P'_m = 0.02$ and resonance frequency σ_m found using *ode.45* in MATLAB. The damping coefficient, ξ, is 0.01. Beating oscillations of the generalized coordinates β_m occur. The same plots without damping are given in Figure 2.5.

Sloshing in an Upright Circular Cylinder

The natural sloshing modes and the Stokes-Joukowski potential needs to be known for calculation of the hydrodynamic coefficients for an upright circular cylindrical tank. As seen in Equation (2.14), there are two different natural modes for a circular tank associated with sine and cosine terms. These are denoted by 1 for the cosine and 2 for the sine term:

$$\varphi_{m,n,1}(r, \theta, z) = R_{m,n}(r)\frac{cosh(k_{m,n}(z + h))}{cosh(k_{m,n}h)}cos(m\theta),$$

$$\varphi_{m,n,2}(r, \theta, z) = R_{m,n}(r)\frac{cosh(k_{m,n}(z + h))}{cosh(k_{m,n}h)}sin(m\theta), \tag{2.29}$$

$$m = 0, 1...; \quad n = 1, 2...$$

where

$$R_{m,n}(r) = \frac{J_m(k_{m,n}r)}{J_m(k_{m,n}R_0)}$$

$$\kappa_{m,n} = \frac{\sigma_{m,n}^2}{g} = k_{m,n}tanh(k_{m,n}h). \tag{2.30}$$

Note that the natural sloshing modes in Equation (2.29) are normalized in such a way to provide unit amplitude at the wall of the surface profiles $f_{m,n}(r, \theta) = \varphi_{m,n}(r, \theta, 0)$. This can be seen from Equation (2.30) that $R_{m,n}(r = R_0) = 1$.

The Stokes-Joukowsky potential, $\mathbf{\Omega}$, must then be found. The Laplace equation is linear and the superposition principle therefore applies. The boundary value problem for the Stokes-Joukowsky potential follows by inserting the term $\omega(t)\mathbf{\Omega}_0(x, y, z)$ from Equation (2.22) into the linearized boundary-value problem for the velocity potential Φ, Equation (2.20). Separation of variables is then possible due to the simple tank geometry and the solution are as follows

$$\Omega_{01} = -F(r, z)sin(\theta)$$

$$\Omega_{02} = F(r, z)cos(\theta) \tag{2.31}$$

$$\Omega_{03} = 0$$

with

$$F(r, z) = zr - 4R_0^2 \sum_{j=1}^{\infty} \frac{R_{1,j}(r)}{(\iota_{1,j}^2 - 1)\iota_{1,j}} \times \frac{sinh(k_{1,j}(z + \frac{1}{2}h))}{cosh(\frac{1}{2}k_{1,j}h)}. \tag{2.32}$$

The hydrodynamic coefficients can now be calculated from Equation (2.26). Note the additional indexes due to the 3-dimensional geometry. The only nonzero coefficients are given below:

$$\mu_{1,j,1} = \mu_{1,j,2} = \frac{\rho\pi}{\kappa_{1,j}} \int_0^{R_0} rR_{1,j}^2(r)\, dr$$

$$= \frac{\rho\pi R_2^2}{\kappa_{1,j}} \frac{\iota_{1,j}^2 - 1}{2\iota_{1,j}^2} = \frac{\rho\pi R_2^3(\iota_{1,j}^2 - 1)}{2\iota_{1,j}^3 tanh(\iota_{1,j}h/R_0)}$$

$$\lambda_{1(1,j,1)} = \lambda_{2(1,j,2)} = \rho\pi \int_0^{R_0} r^2 R_{1,j}(r)\, dr = \frac{\rho\pi R_0^3}{\iota_{1,j}^2} \tag{2.33}$$

$$\lambda_{02(1,j,1)} = \lambda_{01(1,j,2)} = \rho\pi \int_0^{R_0} rR_{1,j}(r)F(r,0)\, dr$$

$$= -\frac{2\pi\rho R_0^4}{\iota_{1,j}^3} tanh(\frac{\iota_{1,j}h}{2R_0}).$$

The modal equations (2.24) formulated relative to $\beta_{1,j,1}$ and $\beta_{1,j,2}$ and with the hydrodynamic coefficients for an upright circular cylinder (2.33) are

$$\ddot{\beta}_{1,j,1} + \sigma_{1,j}^2 \beta_{1,j,1} = -P_j[\ddot{\eta}_1(t) - g\eta_5 g(t) - S_j\ddot{\eta}_5(t)]$$
$$\ddot{\beta}_{1,j,2} + \sigma_{1,j}^2 \beta_{1,j,2} = -P_j[\ddot{\eta}_2(t) - g\eta_4 g(t) - S_j\ddot{\eta}_4(t)]. \tag{2.34}$$

Here are

$$P_j = \frac{2\iota_{1,j} tanh(\iota_{1,j}h/R_0)}{\iota_{1,j}^2 - 1}$$

$$S_j = \frac{2R_0 tanh(\iota_{1,j}h/2R_0)}{\iota_{1,j}}. \tag{2.35}$$

Forces and Moments due to Linear Sloshing

A brief description of the forces and moments due to linear sloshing is given in the following. See Faltinsen and Timokha (2009) for more details.

The derivation of linear force due to internal fluid starts with conservation of fluid momentum. Equation (2.36) expresses force in terms of hydrodynamic momentum.

$$\mathbf{F} = -\dot{\mathbf{M}} + M_l \mathbf{g} \tag{2.36}$$

The linearized momentum is

$$\mathbf{M}(t) = \rho \int_{Q_0} \mathbf{v} \, dQ = \rho Vol \, \mathbf{v}_0 + \rho \omega \times \int_{Q_0} \mathbf{r} \, dQ + \rho \int_{Q_0} \mathbf{v}_r \, dQ \tag{2.37}$$

where $\mathbf{v}_r$ is the relative velocity of the liquid and Vol is the liquid volume. Evaluating the integrals in Equation (2.37) and inserting into Equation (2.36) gives the expression for the linear hydrodynamic force in the *tank-fixed* coordinate system:

$$\mathbf{F}(t) = -M_l g \mathbf{e}_3 + \mathbf{e}_1 \left[M_l(g\eta_5 - \ddot{\eta}_1 - \ddot{\eta}_5 z_{lC_0} + \ddot{\eta}_6 y_{lC_0}) - \sum_{j=1}^{\infty} \lambda_{1j} \ddot{\beta}_j \right]$$

$$+ \mathbf{e}_2 \left[M_l(-g\eta_4 - \ddot{\eta}_2 - \ddot{\eta}_6 x_{lC_0} + \ddot{\eta}_4 z_{lC_0}) - \sum_{j=1}^{\infty} \lambda_{2j} \ddot{\beta}_j \right] + \mathbf{e}_3 \left[M_l(-\ddot{\eta}_3 - \ddot{\eta}_4 y_{lC_0} + \ddot{\eta}_5 x_{lC_0} \right] \tag{2.38}$$

The terms $M_l g[\eta_4 \mathbf{e}_1 - \eta_4 \mathbf{e}_2]$ in Equation (2.38) is a consequence of the frozen liquid weight term $-M_l g \mathbf{e}_3$ in the *tank-fixed* coordinate system. Frozen liquid means to replace the liquid with an equivalent solid mass with the same mass distribution as the liquid. The effect of the free-surface is then excluded.

Moments and forces in ship applications are often described in an inertial system; an Earth-fixed coordinate system. It is therefore of interest to express Equation (2.38) in the global inertial coordinate system $O'x'y'z'$.

$$\mathbf{F}(t) = -M_l g \mathbf{e}_3' + \mathbf{e}_1' \left[M_l(-\ddot{\eta}_1 - \ddot{\eta}_5 z_{lC_0} + \ddot{\eta}_6 y_{lC_0}) - \sum_{j=1}^{\infty} \lambda_{1j} \ddot{\beta}_j \right]$$

$$+ \mathbf{e}_2' \left[M_l(-\ddot{\eta}_2 - \ddot{\eta}_6 x_{lC_0} + \ddot{\eta}_4 z_{lC_0}) - \sum_{j=1}^{\infty} \lambda_{2j} \ddot{\beta}_j \right] + \mathbf{e}_3' \left[M_l(-\ddot{\eta}_3 - \ddot{\eta}_4 y_{lC_0} + \ddot{\eta}_5 x_{lC_0} \right] \tag{2.39}$$

The only difference between the force referring to the *tank-fixed* and the inertial coordinate system is the abovementioned weight term. When a tank is completely filled, the mass centre does not move and the β_j-dependent quantities in Equation (2.39) disappears. The linear force in the tank is then equivalent to inertia force due to *frozen* liquid.

The Bernoulli equation gives the hydrodynamic moments relative to x-, y-, and z-axes as

$$\mathbf{M}_o(t) = -\rho \int_{S(t)+\sum(t)} r \times \left(\left[\frac{\partial \Phi}{\partial t} + \frac{1}{2}(\nabla \Phi)^2 - \nabla \Phi \cdot (\mathbf{v}_0 + \omega \times \mathbf{r}) - g \cdot r \right] \mathbf{n} \right) dS \quad (2.40)$$

By linearizing the terms and introducing the generalized coordinates β_j, the resulting hydrodynamic moment takes the form

$$\mathbf{M}_o(t) = [M_l g(x_{lC_0}\mathbf{e}_2 - y_{lC_0}\mathbf{e}_1]$$

$$+ \mathbf{e}_1 \left[M_l(gz_{lC_0}\eta_4 + z_{lC_0}\ddot{\eta}_2 - y_{lC_0}\ddot{\eta}_3) - \sum_{k=4}^{6} J^1_{01(k-3)}\ddot{\eta}_k - \sum_{j=1}^{\infty}(g\lambda_{2j}\beta_j + \lambda_{01j}\ddot{\beta}_j) \right]$$

$$+ \mathbf{e}_2 \left[M_l(gz_{lC_0}\eta_5 + x_{lC_0}\ddot{\eta}_3 - z_{lC_0}\ddot{\eta}_1) - \sum_{k=4}^{6} J^1_{02(k-3)}\ddot{\eta}_k - \sum_{j=1}^{\infty}(-g\lambda_{1j}\beta_j + \lambda_{02j}\ddot{\beta}_j) \right]$$

$$+ \mathbf{e}_3 \left[M_l(-g(x_{lC_0}\eta_4 + y_{lC_0}\eta_5) + y_{lC_0}\ddot{\eta}_1 - x_{lC_0}\ddot{\eta}_2) - \sum_{k=4}^{6} J^1_{03(k-3)}\ddot{\eta}_k - \sum_{j=1}^{\infty}\lambda_{03j}\ddot{\beta}_j \right] \quad (2.41)$$

Computation of the hydrodynamic force and moment require the hydrodynamic coefficients given in Equation (2.26) and the symmetric inertia tensor

$$J^1_{0ij} = \rho \int_{S_0+\sum_0} \Omega_0 \frac{\partial \Omega_{0j}}{\partial n} dS \quad (2.42)$$

In contrast to hydrodynamic force, hydrodynamic moment of a completely filled tank is not the same as for *frozen* liquid. This is due to the symmetric inertia tensor J^1_{0ij} which differs from the tensor for frozen liquid I^0_{ij}. It should be mentioned that for some three-dimensional bodies, the j-summation in Equation (2.39) and (2.41) changes to summations over two indices when the natural modes are naturally enumerated by (j_1, j_2). This will be the case for an upright circular cylinder.

Sloshing in the Frequency-Domain

When analysing coupled sloshing and body motions of a closed floating fish cage in the frequency domain, the effect of sloshing may be represented in terms of either added mass or

restoring coefficients. A combination of added mass and restoring terms may also be used. The equations of body motions refer to motions in the global inertial coordinate system, not the tank-fixed coordinate system. The hydrodynamic forces and moments due to sloshing must therefore be transferred to the global inertial coordinate system in the analysis. Assume motion mode j expressed in the *tank-fixed* coordinate system as

$$\eta_j(t) = \eta_{ja}cos(\sigma t + \epsilon_j), \quad j = 1, ...6. \tag{2.43}$$

and assume harmonic forcing with frequency σ as

$$K_m(t) = \sigma^2 P'_{mj}cos(\sigma t + \epsilon_j) = \sigma^2 \tilde{P}_{mj}\eta_{ja}cos(\sigma t + \epsilon_j). \tag{2.44}$$

The coefficients $\tilde{P}_{mj}$ are found by Equation (2.25) and can be expressed as

$$\tilde{P}_{m1} = \lambda_{1m}/\mu_m, \quad \tilde{P}_{m2} = \lambda_{2m}/\mu_m, \quad \tilde{P}_{m3} = 0,$$
$$\tilde{P}_{m4} = (-g\lambda_{2m}\sigma^{-2} + \lambda_{01m})/\mu_m, \tag{2.45}$$
$$\tilde{P}_{m5} = (g\lambda_{1m}\sigma^{-2} + \lambda_{02m})/\mu_m, \quad \tilde{P}_{m6} = \lambda_{03m}/\mu_m.$$

The linear modal Equations (2.24) with forcing (2.44) have the analytical solution given by (2.27).

The steady-state hydrodynamic force and moment components acting on the tank due to the internal liquid are now denoted F_k for $k = 1, ...6$ and are from now on considered in the *intertial* coordinate system. Therefore, $k = 1, 2, 3$ indicates the force components along the axes x', y' and z' and $k = 4, 5, 6$ indicates the moment components around these axes. The effect of sloshing will now be represented in terms of added mass coefficients. These are defined by the relationship

$$F_k(t) = -A_{kj}\ddot{\eta}_j(t) = A_{kj}[\sigma^2\eta_{ja}cos(\sigma t + \epsilon_j)] \qquad k, j = 1, ...6 \tag{2.46}$$

where A_{kj} is the added mass coefficient for force in k-direction due to acceleration in j-direction.

The added mass coefficients due to the internal liquid are divided into three contributions.

First the liquid is frozen. A solid body with the same geometry and equivalent mass is considered. Second, the tank is completely filled by the liquid and therefore has no free-surface effects. Third, free-surface effects due to linear sloshing. The added mass coefficients can now be found by inserting the analytical solution of $\beta_j(t)$ given in Equation (2.27) into the hydrodynamic forces and moments due to sloshing, given in (2.39) and (2.41). Added mass due to frozen liquid is

$$
\begin{aligned}
&A_{11}^{frozen} = M_l, \quad A_{22}^{frozen} = M_l, \quad A_{33}^{frozen} = M_l \\
&A_{44}^{frozen} = M_l \sigma^{-2} g z_{lC_0} + I_{11}^0 \\
&A_{55}^{frozen} = \sigma^{-2} M_l g z_{lC_0} + I_{22}^0 \\
&A_{15}^{frozen} = M_l z_{lC_0}, \quad A_{16}^{frozen} = -M_l y_{lC_0} \\
&A_{24}^{frozen} = -M_l z_{lC_0}, \quad A_{26}^{frozen} = M_l x_{lC_0} \\
&A_{34}^{frozen} = M_l y_{lC_0}, \quad A_{35}^{frozen} = -M_l x_{lC_0} \\
&A_{42}^{frozen} = -M_l z_{lC_0}, \quad A_{43}^{frozen} = M_l y_{lC_0} \\
&A_{51}^{frozen} = M_l z_{lC_0}, \quad A_{53}^{frozen} = M_l x_{lC_0} \\
&A_{61}^{frozen} = M_l y_{lC_0}, \quad A_{62}^{frozen} = M_l x_{lC_0} \\
&A_{12}^{frozen} = A_{21}^{frozen} = A_{13}^{frozen} = A_{31}^{frozen} \\
&\qquad = A_{14}^{frozen} = A_{41}^{frozen} = A_{23}^{frozen} \\
&\qquad = A_{32}^{frozen} = A_{25}^{frozen} = A_{52}^{frozen} \\
&\qquad = A_{36}^{frozen} = A_{63}^{frozen} = 0 \\
&A_{64}^{frozen} = -M_l g x_{lC_0} \sigma^{-2} + I_{31}^0 \\
&A_{65}^{frozen} = -M_l g y_{lC_0} \sigma^{-2} + I_{32}^0 \\
&A_{45}^{frozen} = I_{12}^0, \quad A_{54}^{frozen} = I_{21}^0 \\
&A_{46}^{frozen} = I_{13}^0, \quad A_{56}^{frozen} = I_{23}^0, \quad A_{66}^{frozen} = I_{33}^0.
\end{aligned}
\tag{2.47}
$$

Here the inertia tensor $\mathbf{I}^0$ is defined by

$$\mathbf{I^0} = \begin{vmatrix} I_{11}^0 & I_{12}^0 & I_{13}^0 \\ I_{21}^0 & I_{22}^0 & I_{23}^0 \\ I_{31}^0 & I_{32}^0 & I_{33}^0 \end{vmatrix} = \rho \begin{vmatrix} \int_{Q_0} (y^2 + z^2)\, dQ & -\int_{Q_0} xy\, dQ & -\int_{Q_0} xz\, dQ \\ -\int_{Q_0} xy\, dQ & \int_{Q_0} (x^2 + z^2)\, dQ & -\int_{Q_0} yz\, dQ \\ -\int_{Q_0} xz\, dQ & -\int_{Q_0} zy\, dQ & \int_{Q_0} (y^2 + x^2)\, dQ \end{vmatrix} \qquad (2.48)$$

where Q_0 is the liquid volume. The added mass for a completely filled tank may be obtained by replacing the intertia tensor I^0 with J_0^1 in Equation (2.47).

$$A_{(3+k)(3+j)}^{filled} = \begin{cases} A_{(3+k)(3+j)}^{frozen} + \left(J_{0ij}^1 - I_{ij}^0\right) & i, j = 1, 2, 3 \\ A_{ij}^{frozen} & i \text{ or } j \leq 3 \end{cases} \qquad (2.49)$$

The added mass coefficients due to the free-surface is

$$A_{1k}^{slosh} = \sum_{m=1}^{\infty} \lambda_{1m} \frac{\tilde{P}_{mk}\sigma^2}{\sigma_m^2 - \sigma^2}, \qquad A_{2k}^{slosh} = \sum_{m=1}^{\infty} \lambda_{2m} \frac{\tilde{P}_{mk}\sigma^2}{\sigma_m^2 - \sigma^2}$$

$$A_{3k}^{slosh} = 0, \quad k = 1, \ldots 6,$$

$$A_{43}^{slosh} = A_{53}^{slosh} = A_{63}^{slosh} = 0$$

$$A_{4(3+j)}^{slosh} = \sum_{m=1}^{\infty} \left(-\frac{g\lambda_{2m}}{\sigma^2} + \lambda_{01m}\right) \frac{\tilde{P}_{m(3+j)}\sigma^2}{\sigma_m^2 - \sigma^2} \qquad j = 1, 2, 3.$$

$$A_{5(3+j)}^{slosh} = \sum_{m=1}^{\infty} \left(\frac{g\lambda_{1m}}{\sigma^2} + \lambda_{02m}\right) \frac{\tilde{P}_{m(3+j)}\sigma^2}{\sigma_m^2 - \sigma^2} \qquad j = 1, 2, 3.$$

$$A_{6(3+j)}^{slosh} = \sum_{m=1}^{\infty} \frac{\lambda_{03m}\tilde{P}_{m(3+j)}\sigma^2}{\sigma_m^2 - \sigma^2} \qquad j = 1, 2, 3,$$

$$A_{41}^{slosh} = \sum_{m=1}^{\infty} \left(-\frac{g\lambda_{2m}}{\sigma^2} + \lambda_{01m}\right) \frac{\tilde{P}_{m1}\sigma^2}{\sigma_m^2 - \sigma^2} \qquad (2.50)$$

$$A_{42}^{slosh} = \sum_{m=1}^{\infty} \left(-\frac{g\lambda_{2m}}{\sigma^2} + \lambda_{01m}\right) \frac{\tilde{P}_{m2}\sigma^2}{\sigma_m^2 - \sigma^2}$$

$$A_{51}^{slosh} = \sum_{m=1}^{\infty} \left(\frac{g\lambda_{1m}}{\sigma^2} + \lambda_{02m}\right) \frac{\tilde{P}_{m1}\sigma^2}{\sigma_m^2 - \sigma^2}$$

$$A_{52}^{slosh} = \sum_{m=1}^{\infty} \left(\frac{g\lambda_{1m}}{\sigma^2} + \lambda_{02m}\right) \frac{\tilde{P}_{m2}\sigma^2}{\sigma_m^2 - \sigma^2}$$

$$A_{61}^{slosh} = \sum_{m=1}^{\infty} \frac{\lambda_{03m}\tilde{P}_{m1}\sigma^2}{\sigma_m^2 - \sigma^2}, \qquad A_{62}^{slosh} = \sum_{m=1}^{\infty} \frac{\lambda_{03m}\tilde{P}_{m2}\sigma^2}{\sigma_m^2 - \sigma^2}$$

The final added mass coefficients due to the liquid to be included in the equations of motion for the floating body are given as

$$A_{ij} = A_{ij}^{filled} + A_{ij}^{slosh}. \tag{2.51}$$

Be careful of not including the mass of the liquid, M_l in Equation (2.47), twice in the equations of motion.

2.3   Response in Regular Waves

In this section the dynamics of closed aquaculture plants are investigated using linear potential theory. This is done by studying coupled sloshing and tank motions in the frequency domain. The aim of this section is to describe an approach for a coupled analysis with motions and sloshing for closed aquaculture plants.

Figure 2.7 displays a floating closed cage modelled as a system consisting of a body with two degrees of freedom, surge and pitch. The mass of the body is M and the mass of the internal liquid is M_l. Positive directions of the motions are given in the figure according to a right-hand coordinate system.
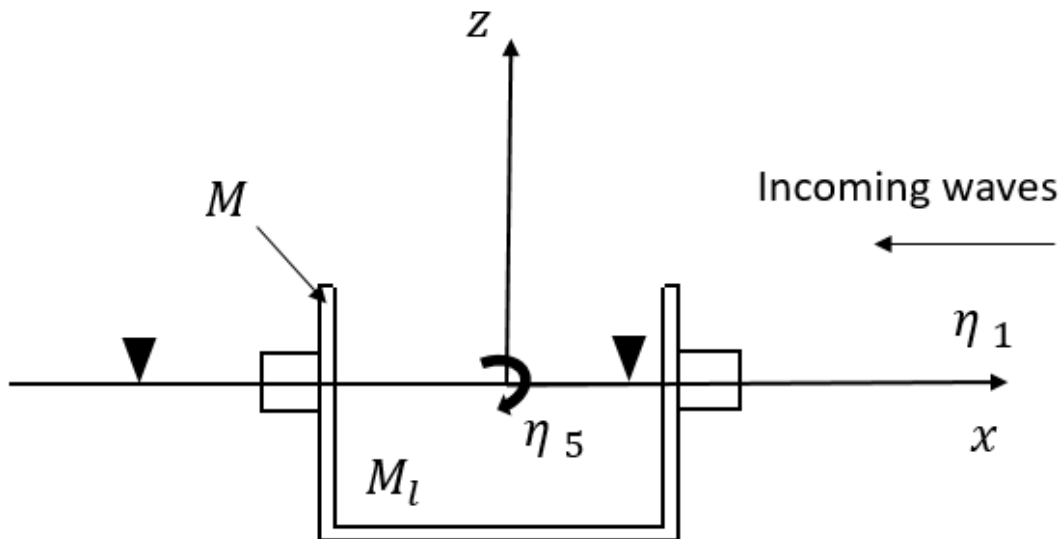
Figure 2.7: Freely floating closed fish cage with mass M and internal liquid with mass M_l. Two degrees of freedom are considered, surge and pitch.

Applying Newton's second law on the body with mass M, in each degree of freedom results in a system of equations consisting of two coupled equations of motion (2.52).

$$\sum F_1 = M\ddot{\eta}_1 + M_{Zg}\ddot{\eta}_5$$
$$\sum F_5 = I_5\ddot{\eta}_5 + M_{Zg}\ddot{\eta}_1$$

(2.52)

Here the mass matrix of the closed aquaculture cage is:

$$\mathbf{M}_c = \begin{bmatrix} M & M_{Zg} \\ M_{Zg} & I_5 \end{bmatrix}$$

(2.53)

The sum of forces and moments is calculated about the origin of the body-fixed coordinate system, O, specified in Section 2.1. Further, the forces and moments are divided into contributions from the exterior water and the internal liquid.

$$\sum F_k = F_k^i + F_k^e \qquad \text{for} \quad k = 1, 5$$

(2.54)

Here i and e are denoting *internal* and *exterior* forces, respectively.

Exterior Problem

Let's first investigate the forces from the outer water. According to Faltinsen (1990) the hydrodynamic problem for a floating body in regular waves is usually dealt into two sub-problems:

A) The forces and moments on the body when the body is not allowed to move and there are incoming regular waves. The hydrodynamic loads are called wave excitation loads, $F_{ex,k}$ and can be divided into Froude-Kriloff and diffraction forces and moments.

B) The forces and moments when the body is forced to oscillate with the incoming wave frequency in any degree of freedom. There are no incoming waves. The hydrodynamic loads are then divided into added mass, damping and restoring terms.

The total hydrodynamical forces from the exterior water on the closed cage, in direction

k, are then

$$F_k^e = -A_{k1}^e \ddot{\eta}_1 - A_{k5}^e \ddot{\eta}_5 - B_{k1}^e \ddot{\eta}_1 - B_{k5}^e \ddot{\eta}_5 - C_{k1}^e \ddot{\eta}_1 - C_{k5}^e \ddot{\eta}_5 + F_{ex,k}^e \qquad (2.55)$$

Where A_{kj}, B_{kj} and C_{kj} are the added mass, damping and restoring coefficients in direction k due to motion in direction j. The added mass and damping coefficients are frequency dependent, $A_{kj} = A_{kj}(\omega)$ and $B_{kj} = B_{kj}(\omega)$. Assuming linear theory, the coefficients and excitation forces can be found using WADAM/WAMIT.

Internal Problem

The internal forces on the structure with mass M due to the contained liquid with mass M_l are described in Section 2.2.2 under the title "Sloshing in the Frequency Domain". Here the effect of sloshing is represented in terms of added mass coefficients divided into three terms: *frozen*, *filled* and *slohs*. Frozen represents the forces from an equivalent solid body mass of M_l. The filled term is connected to the Stokes-Joukowsky potential. Last, slosh represent the effect of the free-surface, the effect of sloshing.

Note that the forces from the mass of the water are included in the internal problem. Also, a correction of the restoring term due a quasi-steady moment is included in A_{55}. This is due the effect of the free-surface leading to a destabilizing moment because of change in location of centre of gravity. This effect is represented as an added mass term, as the relation between restoring and added mass is $-\omega^2 A_{kj} = C_{kj}$.

Coupled Problem

The hydrodynamic forces on the body have now been found and are inserted into (2.52). The coupled equation of rigid body motions and sloshing is now written as

$$
\begin{aligned}
(M + A_{11})\ddot{\eta}_1 + (M_{Zg} + A_{15})\ddot{\eta}_5 + B_{11}\dot{\eta}_1 + B_{15}\dot{\eta}_5 + C_{11}\eta_1 + C_{15}\eta_5 = F_{ex,1} \\
(M_{Zg} + A_{51})\ddot{\eta}_1 + (I_5 + A_{55})\ddot{\eta}_5 + B_{51}\dot{\eta}_1 + B_{55}\dot{\eta}_5 + C_{51}\eta_1 + C_{55}\eta_5 = F_{ex,5}
\end{aligned}
\qquad (2.56)
$$

with $A_{kj} = A_{kj}^e + A_{kj}^i$, $B_{kj} = B_{kj}^e + B_{kj}^i$ and $C_{kj} = C_{kj}^e + C_{kj}^i$.

The coupled equations of motion can be solved assuming harmonic wave excitation loads, $F_{ex,k} = \bar{F}_{ex,k} e^{-i\omega t}$, and motions in phase with the excitation $\eta_k = \bar{\eta}_k e^{-i\omega t}$. Substituting this into Equation (2.56) and dividing by $e^{-i\omega t}$ gives

$$
\begin{aligned}
-(M + A_{11})\omega^2 \bar{\eta}_1 - (M_{Zg} + A_{15})\omega^2 \bar{\eta}_5 - B_{11} i\omega \bar{\eta}_1 - B_{15} i\omega \bar{\eta}_5 + C_{11} \bar{\eta}_1 + C_{15} \bar{\eta}_5 &= \bar{F}_{ex,1} \\
-(M_{Zg} + A_{51})\omega^2 \bar{\eta}_1 - (I_5 + A_{55})\omega^2 \bar{\eta}_5 - B_{51} i\omega \bar{\eta}_1 - B_{55} i\omega \bar{\eta}_5 + C_{51} \bar{\eta}_1 + C_{55} \bar{\eta}_5 &= \bar{F}_{ex,5}.
\end{aligned}
\tag{2.57}
$$

The equations are re-written in matrix form:

$$
\begin{bmatrix}
-(M_{11} + A_{11})\omega^2 - B_{11}i\omega + C_{11} & -(M_{15} + A_{15})\omega^2 - B_{15}i\omega + C_{15} \\
-(M_{51} + A_{51})\omega^2 - B_{51}i\omega + C_{51} & -(M_{55} + A_{55})\omega^2 - B_{55}i\omega + C_{55}
\end{bmatrix}
\begin{bmatrix}
\bar{\eta}_1 \\
\bar{\eta}_5
\end{bmatrix}
=
\begin{bmatrix}
\bar{F}_{ex,1} \\
\bar{F}_{ex,5}
\end{bmatrix}
\tag{2.58}
$$

Solving the homogenous system of equations gives the coupled eigenfrequencies of the system, the frequency for wich significant sloshing is expected. To obtain a non-trivial solution to the system the determinant of the coefficients matrix has to be zero.

$$
\det
\begin{bmatrix}
-(M_{11} + A_{11})\omega^2 - B_{11}i\omega + C_{11} & -(M_{15} + A_{15})\omega^2 - B_{15}i\omega + C_{15} \\
-(M_{51} + A_{51})\omega^2 - B_{51}i\omega + C_{51} & -(M_{55} + A_{55})\omega^2 - B_{55}i\omega + C_{55}
\end{bmatrix}
= 0
\tag{2.59}
$$

This gives Equation (2.60) which must be solved with respect to ω. Remember that the added mass and damping frequencies are frequency dependent.

$$
\begin{aligned}
\left(-(M_{11} + A_{11})\omega^2 - B_{11}i\omega + C_{11} \right) & \left(-(M_{55} + A_{55})\omega^2 - B_{55}i\omega + C_{55} \right) \\
- \left(-(M_{15} + A_{15})\omega^2 - B_{15}i\omega + C_{15} \right) & \left(-(M_{55} + A_{55})\omega^2 - B_{55}i\omega + C_{55} \right) = 0
\end{aligned}
\tag{2.60}
$$

The response amplitudes for η_1 and η_5 can also be found by solving Equation (2.58) by multiplying with the inverse of the coefficient matrix on each side of the equation for each wave frequency ω.

Chapter 3

Experiment

An experiment was performed in November 2016 during the pre-project for the present work. A model of a closed fish cage subjected to waves was considered. The geometry of an upright circular cylinder was used in the experiment. The model consisted of a floater and a containment unit kept in position by horizontal linear springs and therefore free to move in six degrees of freedom.

The aim of the experiment was to investigate the effects of sloshing on the dynamics of a closed fish cage considering waves with full scale periods $3.6\text{s} - 7.2\text{s}$. Later, the results will be compared with linear modal theory. The model was tested in regular waves with 81 different wave periods and three different wave steepnesses for each period.

Following sections describe the experimental test set-up, test conditions, instrumentation, the process of data acquisition and a brief discussion of error sources.

3.1   Test set-up

The experiment took place in the small towing tank in Trondheim at Marine Technology Centre at NTNU. The tank was 2.5m wide with a water depth of 1m. A single paddle wavemaker was placed in one end of the tank and a wave beach, for the waves to be absorbed, was located in the other end. The model was placed in the middle of the tank and was kept in position by four mooring lines. Figure 3.1 shows the experiment set-up.
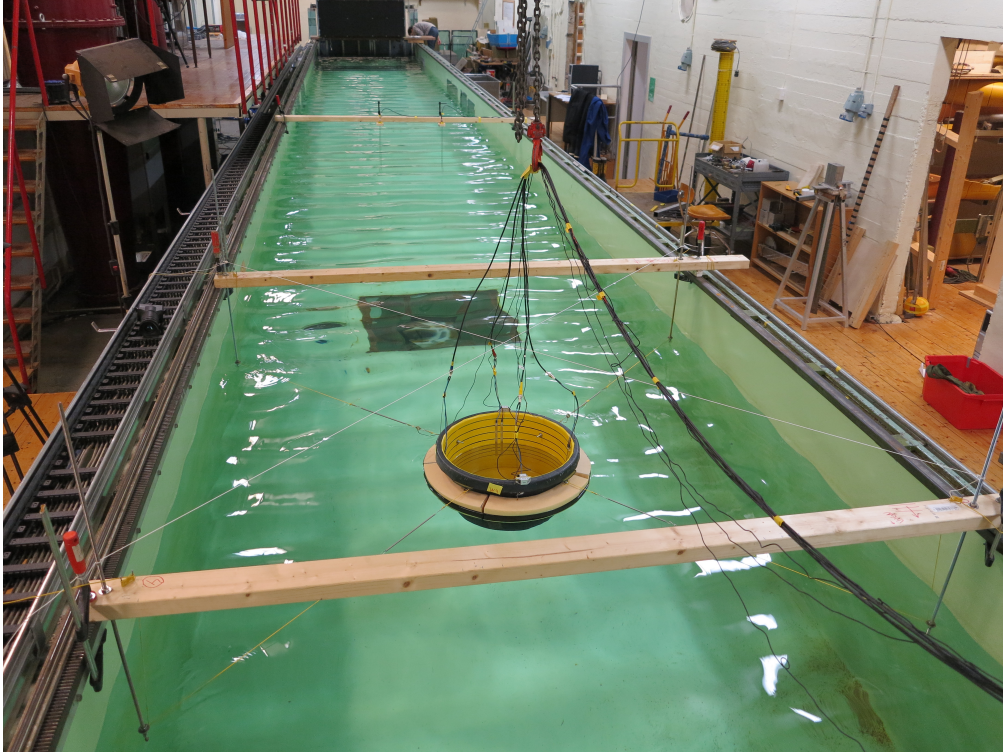
Figure 3.1: The test set-up for a cylindrical closed fish cage in the small towing tank at NTNU.

The dimensions for the model was chosen based on the size of the bucket used to model the closed cage. The model scale was then set to 1 : 81, based on dimensions of suggested concepts closed fish farms. These concepts shapes and sizes vary, but reasonable dimensions are a diameter of $D \simeq 40$m and a diameter to draft ratio of $D/T \simeq 0.5$ (Soltveit, 2016). In addition, the model was loaded with weights to balance the buoyancy force. The main dimensions of the test set-up are listed both in full scale and model scale in Table 3.1.

Table 3.1: Model and full scale dimensions used in the experiment with scale $1 : 81$. The key parameters of the test set-up are visualized in Figure 3.2a.

Quantity	Term	Full scale	Model scale
Internal diameter [m]	D_i	39.12	0.483
Outer diameter [m]	D_o	39.61	0.489
Internal water height [m]	h	19.2	0.237
Draft [m]	T	20.7	0.255
Floater width [m]	f_w	6.5	0.080
z-position of accelerometers [m]	f_z	11.58	0.143
Spring stiffness [N/m]	k_s	$72.2 \cdot 10^6$	136
Pretension mooring lines [N]	F_{ML}	$5.63 \cdot 10^6$	10.6
Period of first sloshing mode [s]	$T_{1,1}$	6.72	0.74
Period of second sloshing mode [s]	$T_{2,1}$	3.84	0.42
Mass displacement [kg]	Δ_{total}	$30.98 \cdot 10^6$	58.3
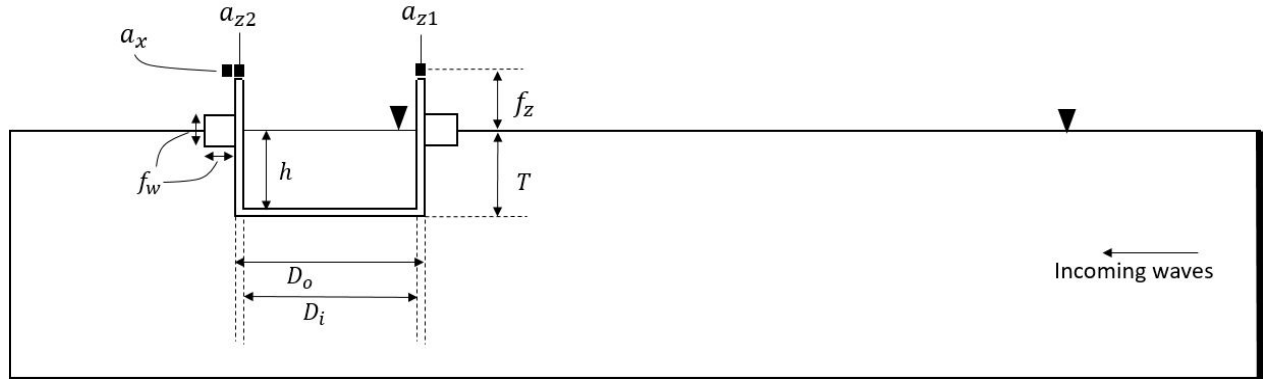
(a) Key parameters of the model geometry for the closed fish farm. The values are listed in Table 3.1. Also notice the accelerometers mounted on the top of the model.
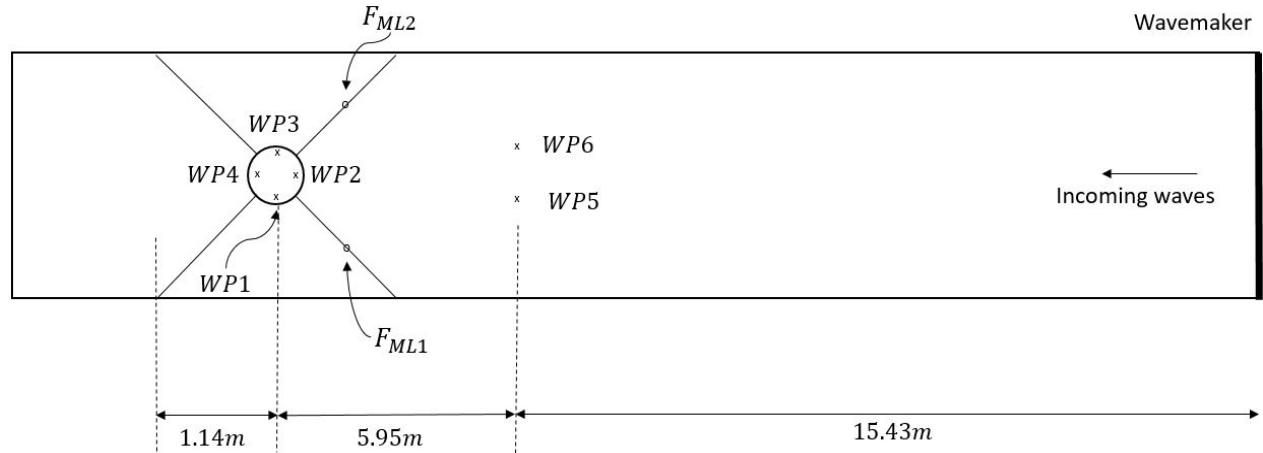
(b) Overview of instrumentation in the test set-up. There were six wave probes measuring the free-surface elevation and two force sensors measuring the forces in the mooring lines.

Figure 3.2: Overview of the test set-up from above and the side.

The incoming wave period and steepness were varied during the test. The test matrix is presented in Table 3.2. 81 wave tests were performed with wave periods in the range of $3.6\text{s} - 7.2\text{s}$ with step 0.045s for three wave steepnesses $H/\lambda = \{1/60, 1/45, 1/30\}$, in total 243 wave tests. Each wave test consisted of $N = 100$ waves and between each test, there was a $t_0 = 180\text{s}$ pause for the waves to die out.

Table 3.2: Full scale test matrix. Here T and λ/H denotes wave period and steepness. N is the number of waves generated by the wavemaker for each wave period and t_0 is the length of pause between each tested wave period.

T_{min} [s]	T_{max} [s]	$\Delta(T)$ [s]	$(\lambda/H)_{min}$	$(\lambda/H)_{max}$	$\Delta(\lambda/H)$	N	t_0 [s]
3.6	7.2	0.045	60	30	15	100	180

Six wave probes denoted by $WP1 - WP6$ were mounted for measurement of the free-surface elevation. Further, model was equipped with sensors measuring the forces in mooring line 1 and 2 denoted F_{ML1} and F_{ML2}. $WP1 - WP4$ were metal tape wave probes while $WP5 - WP6$ were standard capacitance probes with two metal bars 1cm apart. In addition, the model was mounted with three accelerometers for measurement of pitch and surge accelerations. Two accelerometers measured the z-acceleration at the top of each side of the bucket, the last accelerometer measured the x-acceleration. All transducers used in the experiment are shown in Figure 3.3 and Figure 3.2. All the sensors are also listed and explained in Table 3.3. The measurements were sampled with a frequiency of $F_s = 50\text{Hz}$.

Table 3.3: Explanation of all the sensors in the experiment illustrated in Figure 3.2.

Sensor	Unit	Explanation
WP(1-4)	m	Free-surface elevation inside the model at four points
WP(5-6)	m	Free-surface elevation in the tank measuring the incoming waves
$F_{ML(1-2)}$	N	Force in mooring line 1 and 2
a_x	m/s^2	Acceleration in body-fixed x-direction
$a_{z(1-2)}$	m/s^2	Acceleration in body-fixed z-direction
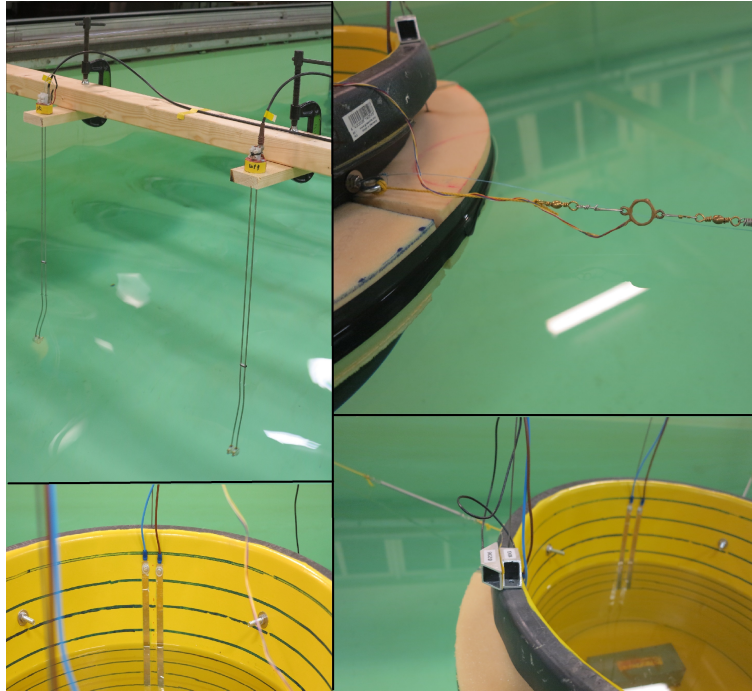
Figure 3.3: Overview of the sensors in the model test. WP(5-6) in the upper left corner, force in mooring line 1 in the upper right corner, WP2 in the lower left corner and x- and z-accelerometers in the lower right corner.

3.2 Data Acquisition

Following data was collected during the experiment; internal free-surface elevation inside the model, free-surface elevation measuring the incoming waves in the tank, force in mooring lines and the z- and x-acceleration of the bucket. The data was logged in time series with a sampling rate of 50Hz and exported to bin-files by the log software, CATMAN. This section will give an overview of the calibration process, the data filtering and the post-processing done in MATLAB.

3.2.1 Calibration

The sensors were calibrated from volts to relevant physical unit. All the transducers were linear. The calibration of the wave probes, force transducers and accelerometers was performed by employees at NTNU.

3.2.2   Calculations of Motions

Surge, pitch and heave motion were calculated from the accelerations in the x- and z-directions. The positive directions of the accelerations were defined during the calibration and are given in Figure 3.4.
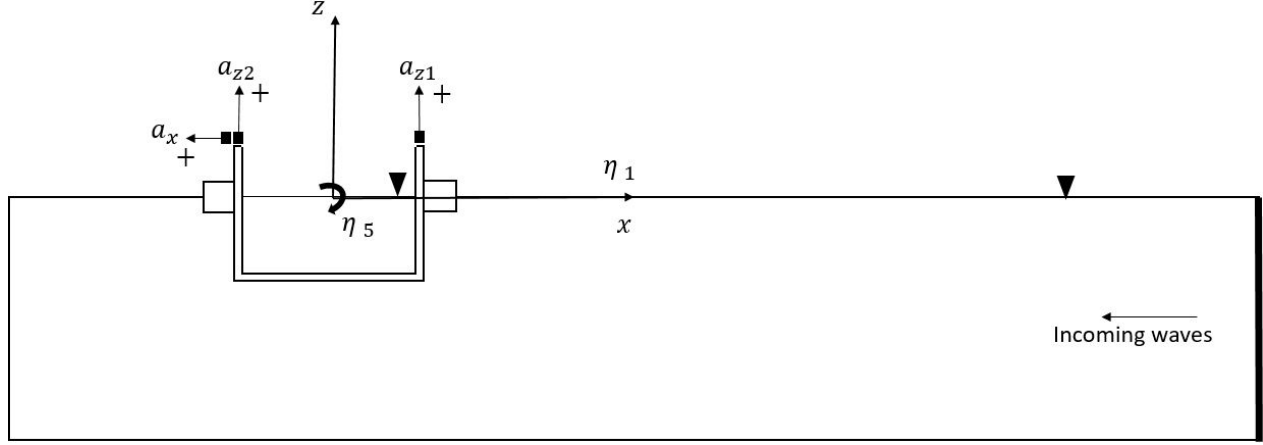
Figure 3.4: Positive directions of the accelerometers and motions.

The directions of the body motions surge, pitch and heave were defined according to the definition of the rigid body motions given in Section 2.1 in the MATLAB post-processing script. A right-handed body-fixed coordinate system were placed with $z = 0$ on the free-surface of the liquid inside the model, see Figure 3.4. The motions are defined according to the right-hand rule. Since the z-accelerometers were located at the model with a horizontal distance, L_z, the pitch acceleration can be found as:

$$\ddot{\eta}_5 = \frac{a_{z2} - a_{z1}}{L_z} \tag{3.1}$$

The measured x-acceleration were the local acceleration, s_1, along the body-fixed x-axis. The surge acceleration was corrected for pitch motion, see Equation (2.10) for motion in x-direction of any point on the body. In addition, the measured x-acceleration must be corrected for the gravity. This is due to that a part of the gravitational acceleration is measured when the model is pitching, see Figure 3.5.
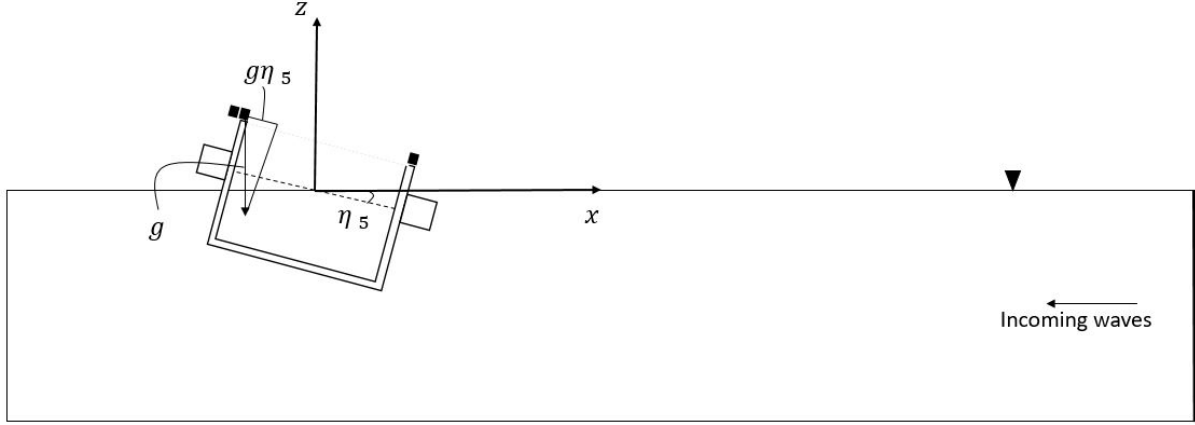
Figure 3.5: This figure illustrates why the measured x-acceleration must be corrected for a component of the gravity. For constant pitch angle η_5 and no other motion, there is no surge acceleration. Still a component of $-g\eta_5$ is measured by the x-accelerometer due to gravity.

The final surge acceleration is

$$\ddot{\eta}_1 = -a_x - g\eta_5 + f_z\ddot{\eta}_5 \tag{3.2}$$

where f_z is the z-position of the z-accelerometers in the body-fixed coordinate system (see Figure 3.2a). Finally, the heave acceleration was found as the mean acceleration in z-direction:

$$\ddot{\eta}_3 = \frac{1}{2}(a_{z1} + a_{z2}) \tag{3.3}$$

For a harmonic motion $\eta = cos(\omega t)$ with frequency ω, the acceleration is given as $\ddot{\eta} = -\omega^2 cos(\omega t)$. Surge, pitch and heave can therefore be found by dividing the acceleration with $-\omega^2$. The calculation was done in the frequency domain applying fast Fourier transform.

3.2.3 Scaling

The Froude number is defined as the ratio between inertia and gravity forces (Steen, 2014):

$$F_N = \frac{U}{\sqrt{gL}}. \tag{3.4}$$

Froude scaling is applied and geometrical similarity with scale ratio $\lambda = D_F/D_M = 81$ assumed. Requiring equality in Froude number gives following relations between model and

full scale fish farm for the physical parameters presented in Table 3.4.

Table 3.4: Froude scaling table from Steen (2014). The applied scaling factor is $\lambda = 81$.

Physical Parameter	Unit	Multiplication factor
Length	[m]	λ
Strucural mass	[kg]	$\lambda^3 \rho_F / \rho_M$
Force	[N]	$\lambda^3 \rho_F / \rho_M$
Moment	[Nm]	$\lambda^4 \rho_F / \rho_M$
Acceleration	[m/s^2]	$a_F = a_M$
Time	[s]	$\sqrt{\lambda}$

Unless otherwise is specified, all results are presented in full scale using Froude scaling.

3.2.4 Calculation of Response Amplitude Operator

As mentioned above, all the data was collected in time series. Three wave steepnesses were tested in the experiment, each steepness with 81 different waves with full scale wave periods ranging from $3.6 - 7.2$s (see test matrix in Table 3.2). Figure 3.6 shows the raw data before processing. The time series of the internal free-surface elevation measured by WP2 and the incoming waves measured by WP6 are shown.
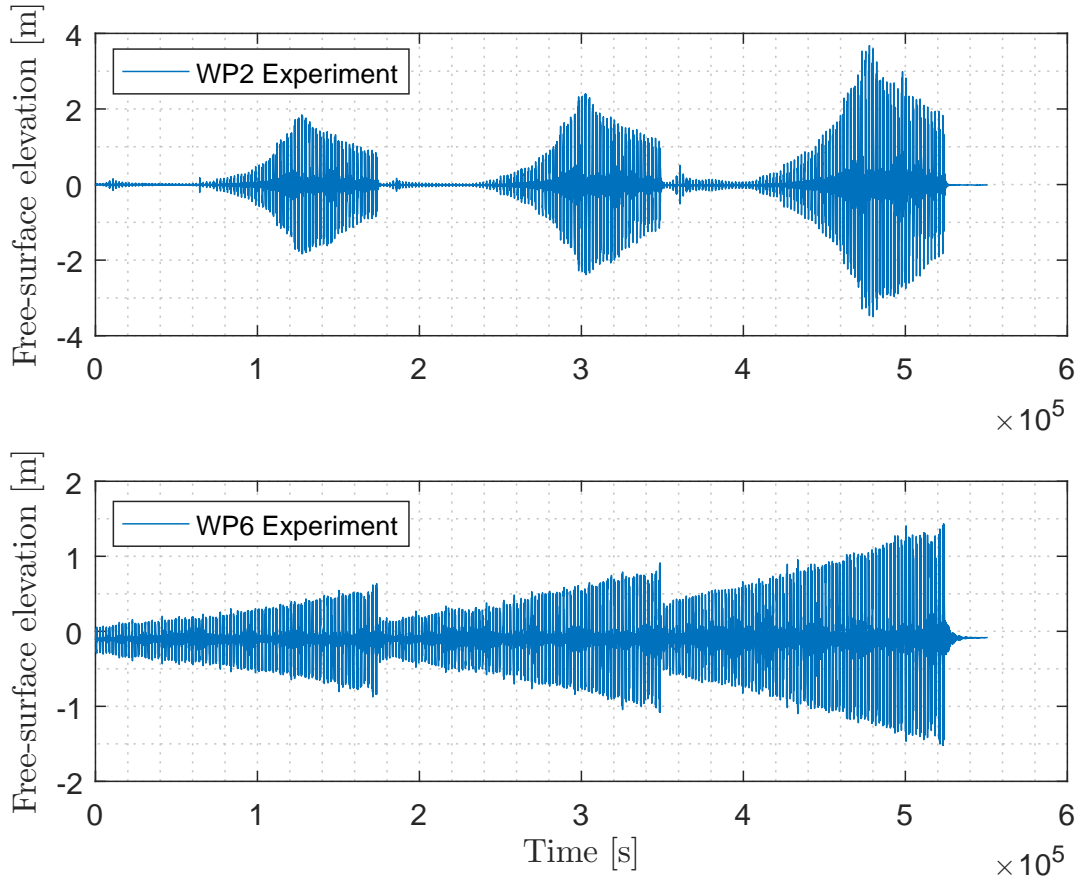
Figure 3.6: Full scale time series of raw data for all three steepnesses measured at wave probe 2 and 6. Each steepness has 81 waves tests with wave period varying from $3.6 - 7.2$s, in total 243 wave tests. WP2 is the free-surface elevation inside the model and WP6 the incoming waves. See Figure 3.2b for specific location of WP2 and WP6.

The response amplitude operator (RAO) is now defined as the amplitude of the response, $|X|$ divided by the amplitude of the forcing term, in this case the incoming wave amplitude ζ_a.

$$RAO_X = \left|\frac{X}{\zeta_a}\right| \tag{3.5}$$

The response amplitude operators (RAOs) were calculated for the motions, mooring line forces and the free-surface elevations at WP$(1-4)$. Data from the time series of each wave test was selected and bandpass filtered, marked in orange in Figure 3.8, with cutoff frequencies $\pm 7\%$ of the incoming wave frequency ω. This is called the first harmonic of the signal. The

second and third harmonics of the signal were also found. This was done by bandpass filtering the selected data with cutoff frequencies $\pm 7\%$ of 2ω and 3ω. Figure 3.7 shows how the first harmonic of the signal at WP2 is found for a single wave test using bandpassfiltering.
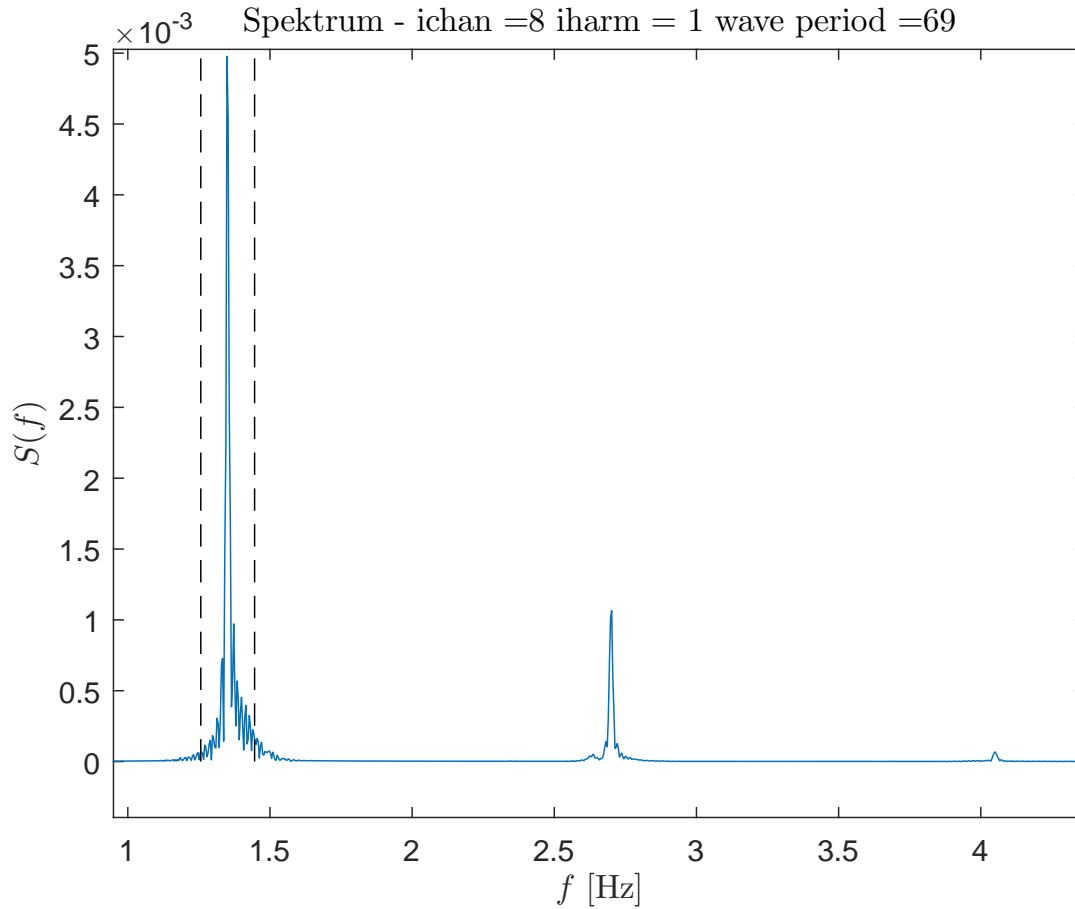
Figure 3.7: This figure shows the spectrum for the signal measured at WP2 for incoming wave frequency $\omega = 0.94\text{rad/s}$ and wave steepness $H/\lambda = 1/60$. The figure illustrates how the first harmonic part of the signal is found by bandpass filtering. The black dashed lines marks the cutoff frequencies used in the bandpass filter. For the second and third harmonics the filter cuts around the second and third peak in the spectrum.

The RAOs for the first, second and third harmonics of the motions and free-surface elevation inside the model were then calculated. This was done by calculating the average amplitude of a selection of 20 periods of the bandpass filtered data, which is marked yellow in Figure 3.8. Finally, the amplitude of the response were normalized with the incident wave amplitude for each wave test, as according to Equation (3.5). Pitch was divided by $\zeta_a k$, to get a nondimensional RAO. The results are presented in Chapter 5.
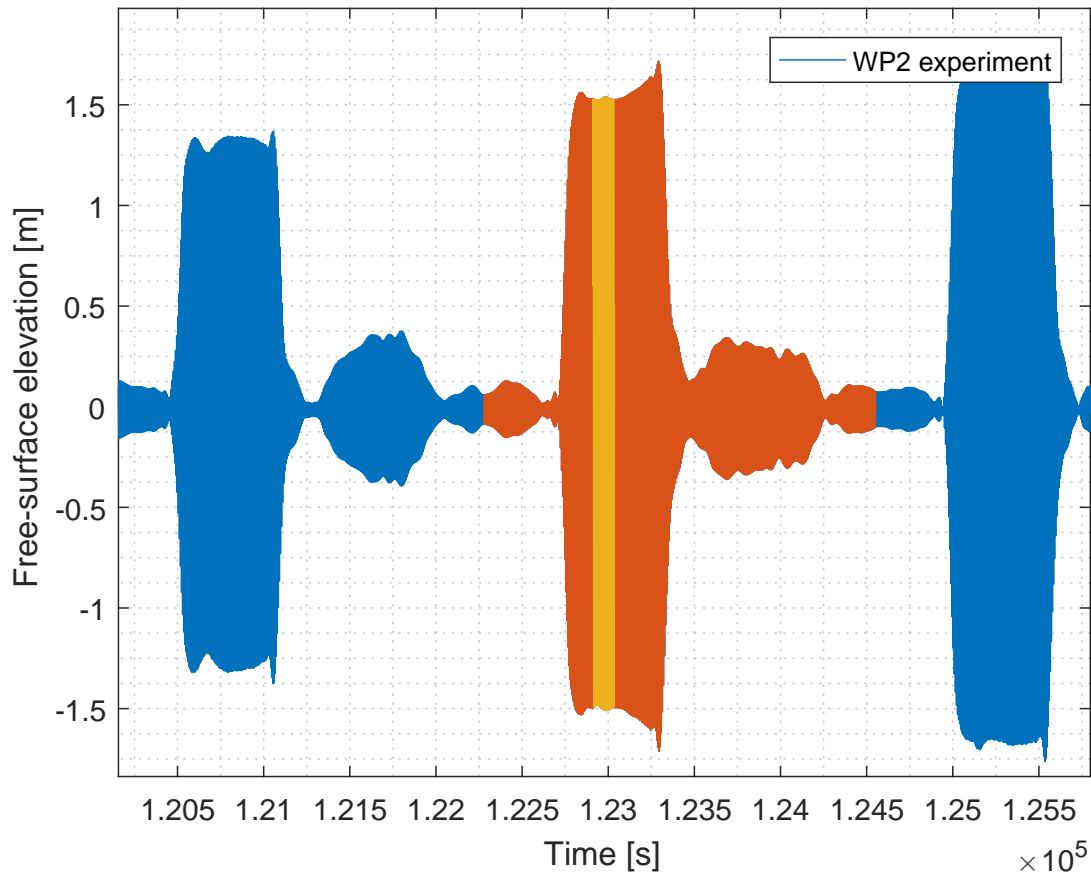
Figure 3.8: Time series of the free-surface elevation measured at WP2 for an arbitrary wave test. The figure illustrates how the amplitude of each wave test is found. The orange part of the signal is bandpass filtered and the amplitude is calculated based on 20 periods of the signal marked with yellow. This is done for all 3×81 wave tests.

3.3 Discussion of Error Sources

There are two types of errors, precision and bias errors. The precision error cannot be calculated as the experiment was only done once without any repetitions. Bias errors are not straight forward to quantify, but an attempt to identify the main errors is given.

Calibration of sensors

Calibration of accelerometers, wave probes and force sensors were only performed once a

couple of days before the experiment was conducted. The calibration factor could therefore be different when the experiment was performed. There is no easy way to estimate this effect.

Model inaccuracies

For simplicity, the model used for the containment unit was a plastic bucket. This bucket was not upright cylindrical but cone shaped, with a flat bottom. In the water surface, the diameter at the internal free-surface was 0.48m while the diameter at the bottom of the bucket was 0.42m, in model scale. This should be kept in mind later, when comparing with results based on numerical calculations for an upright circular cylinder.

Another effect of unknown significance was a slight uneven floater geometry. The floater was carved out by hand and the uncertainty of f_w is estimated to be $\pm$1cm in model scale.

Tank wall effects

The small towing tank was 2.5m and the model diameter was 0.48m in the water line. When the model moved, waves were created due to wave radiation, which were reflected at the tank walls and affected the heave of the model.

A similar experiment with a model of a closed fish farm subjected to waves was conducted by SINTEF Ocean in the SJØFLO project during spring 2017 (SINTEF, 2016). Figure 3.9 is from project SJØFLO and shows the effect of tank walls on the heave RAO for a rigid upright circular cylinder with diameter 1.5m and draft 0.75m.
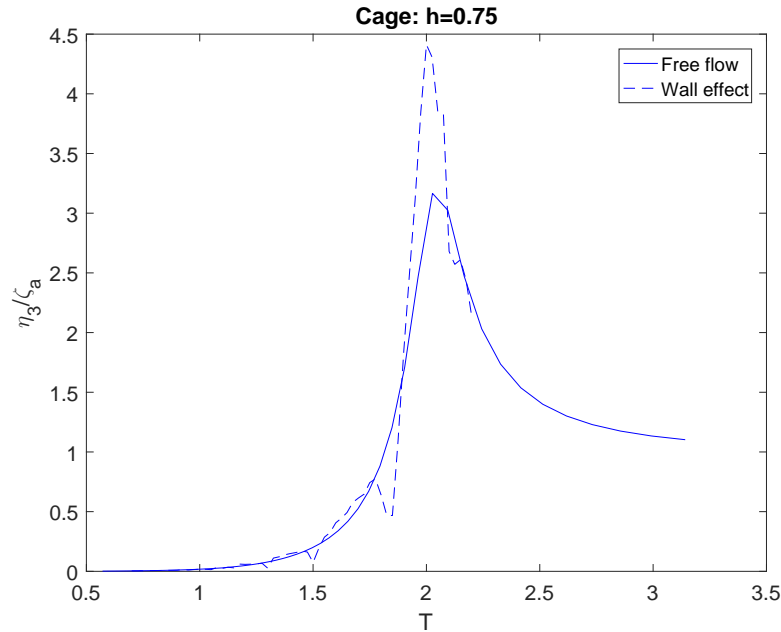
Figure 3.9: Heave response amplitude operator with and without wall effects for an rigid upright circular cylinder with diameter 1.5m and draft 0.75m. The x-axis is incoming wave period T. The calculations is done by Per Christian Endresen during project SJØFLO conducted by SINTEF Ocean AS spring 2017 (SINTEF, 2016).

The RAO with wall effects has larger response for $T = 2.05$s, the natural period of heave. The natural period of heave for the present experiment was higher than the investigated range of wave periods $T = (3.6 - 7.2)$ in full scale. For wave periods lower than the natural period of heave in Figure 3.9, the heave response is cancelled for incoming waves with $T = 1.8$s and $T = 1.5$s. This is expected to be the wall effects in the present experiment as well.

The waves reflected from the walls submerged the floater for some incoming wave frequencies causing lateral instabilities to the model, see Figure 3.10a. Figure 3.10b shows how the floater is submerged to the right, introducing nonlinear damping to the system.
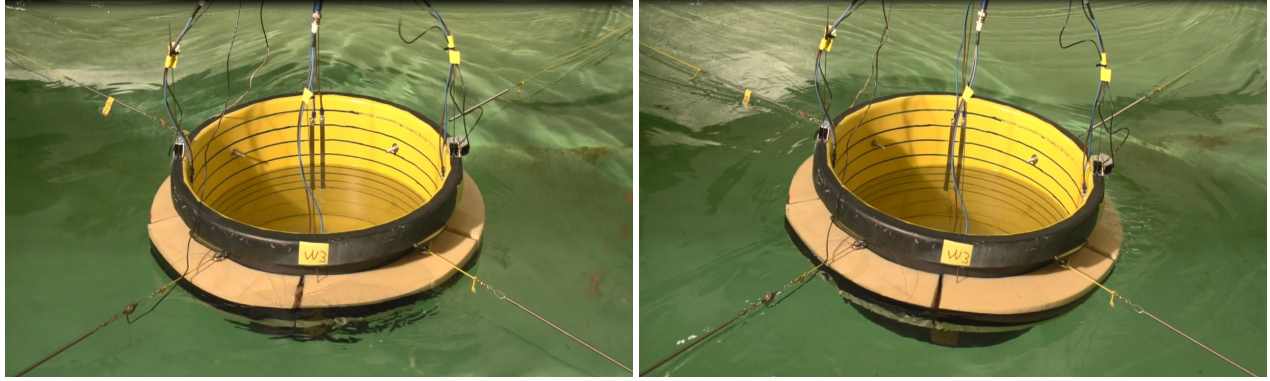
(a) $\omega = 0.94$rad/s
Submerged floater in front.

(b) $\omega = 0.87$rad/s
Submerged floater to the right.

Figure 3.10: Snapshots of the model for two different wave tests. See how the floater is submerged in front at picture (a) and to the right in picture (b). The waves are coming from the left in the pictures. The wave steepness is $H/\lambda = 1/30$.

Waves generated by the model were also reflected by the wavemaker and then came back to the model during a wave test. At the other side, the wave beach damped out the reflected waves. Each wave test consisted of $N = 100$ wave periods, see Table 3.2. When the reflected waves from the wavemaker reached the model, depends on the wave propagation speed which vary with the wave frequency. This was handled when selecting the data for calculation of the response amplitude operators (see Section 3.2.4).

Chapter 4

Method

The following chapter gives a description of the approach for the numerical investigation of the free-surface elevation inside the upright circular cylinder. Linear modal sloshing theory described in Section 2.2.2, assuming prescribed motions, was implemented in MATLAB. The prescribed motions were the results for surge and pitch measured in the experiment. The aim was to simulate the free-surface elevation of the liquid inside the fish cage measured during the experiment.

First the implementation in MATLAB and the numerical solution of the modal equations (2.34) are explained. Second, a sensitivity analysis of the free-surface elevation with respect to the prescribed motions are presented.

4.1   Numerical Calculations

The geometry of investigation was an upright circular cylinder with dimensions given in Table 4.1.

Table 4.1: Model and full scale dimensions defining the geometry used in the numerical calculations. The scale is 1 : 81.

Quantity	Term	Full scale	Model scale
Internal diameter [m]	D_{MT}	38.88	0.480
Internal water height [m]	h_{MT}	19.2	0.237

Surge and pitch measured in the experiment were assumed as the prescribed motions of

the fish cage. Heave does not excite sloshing according to linear modal theory (Faltinsen and Timokha, 2009). The motions were inserted into the modal equations for upright circular cylinder given in Equation (2.34). Only the first equation was used, because it was assumed that the regular incoming waves in the experiment only induced motions in the xz-plane. The modal equations were solved using the built-in MATLAB-function, *ode45(...)*, which is based on explicit fourth-order Runge-Kutta method. In addition the term $2\xi\sigma_m\dot{\beta}_m$ was included in the modal equations to simulate damping, see Equation (2.28). The modal equations are second-order ordinary differential equations (ODEs). Rewriting the ODEs to a system of first-order equations of the form $\dot{\boldsymbol{\beta}} = \mathbf{f}(t, \boldsymbol{\beta})$ gives:

$$
\begin{aligned}
\text{I.)} \quad & \dot{\beta}_{1,j,1}^{(1)} = \beta_{1,j,1}^{(2)} \\
\text{II.)} \quad & \dot{\beta}_{1,j,1}^{(2)} = -P_j[\ddot{\eta}_1(t) - g\eta_5 g(t) - S_j\ddot{\eta}_5(t)] - 2\xi\sigma_{1,j}\beta_{1,j,1}^{(2)} - \sigma_{1,j}^2\beta_{1,j,1}^{(1)}
\end{aligned}
\tag{4.1}
$$

with inital conditions $\boldsymbol{\beta}(t_0) = \boldsymbol{\beta_0}$. Classical Runge-Kutta of fourth-order is then as following (Kreyszig, 2006):

1. Intial values:

$$\boldsymbol{\beta}(t_0) = \boldsymbol{\beta_0}$$

2. For each step $n = 0, 1..., (N-1)$ four auxiliary quantities are calculated:

$$
\begin{aligned}
k_1 &= \Delta t\mathbf{f}(t_n, \boldsymbol{\beta}_n) \\
k_2 &= \Delta t\mathbf{f}(t_n + \tfrac{1}{2}\Delta t, \boldsymbol{\beta}_n + \tfrac{1}{2}\mathbf{k}_1) \\
k_3 &= \Delta t\mathbf{f}(t_n + \tfrac{1}{2}\Delta t, \boldsymbol{\beta}_n + \tfrac{1}{2}\mathbf{k}_2) \\
k_2 &= \Delta t\mathbf{f}(t_n + \Delta t, \boldsymbol{\beta}_n + \mathbf{k}_3)
\end{aligned}
$$

3. The new value, which is an approximation of $\boldsymbol{\beta}(t)$ at t_{n+1} is

$$\boldsymbol{\beta}_{n+1} = \boldsymbol{\beta}_n + \tfrac{1}{6}(\mathbf{k}_1 + 2\mathbf{k}_2 + 2\mathbf{k}_3 + \mathbf{k}_4)$$

.

The system of equations given in (4.1) was then solved with *ode45(...)* in MATLAB from

time t_0 to t_f with zero initial conditions, i.e. $\beta_0^{(1)} = 0$ and $\beta_0^{(2)} = 0$. When the generalized coordinates, $\beta_{1,j,1}(t)$ in Equation (2.34) are found and the natural modes for an upright cylinder are known, see Equation (2.29), the free-surface elevation due to sloshing can be found. The free-surface was finally calculated by Equation (2.21), by summation over j. The damping was, $\xi = 0.01$, for all the numerical calculations of the free-surface.

In order to save computation time the free-surface elevation was calculated one by one for each wave test. This was done by selecting a time window for each wave test for which the free-surface elevation was calculated with modal theory using surge and pitch measured in the experiment. Figure 5.5 shows an example of a wave test measured during the experiment and the computed response in a selected time window. The starting point of the time window was chosen such that the beating oscillations die out before the wave test starts. The end time, t_f, was set to 20s after the data window from which the response amplitudes were found, this data window is marked with black dashed lines in Figure 4.1. This was done to avoid the filtering, performed to obtain the first, second and third harmonics of the signal, to affect the results of the response amplitudes. See Section 3.2.4 for closer explanation of calculation of the response amplitude operators.
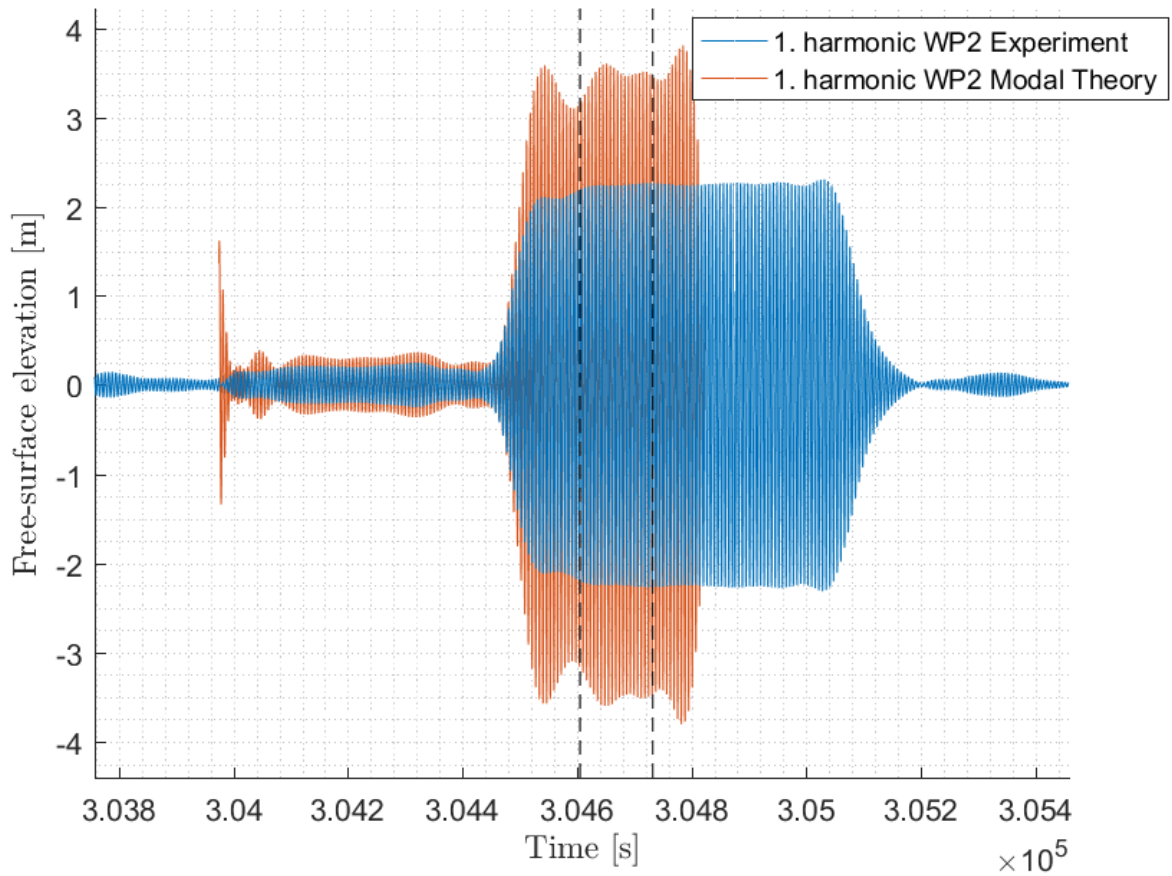
Figure 4.1: Calculated and experimental first harmonic body-fixed free-surface elevation at WP2 for an arbitrary wave test. This figure illustrates for what part of a wave test the free-surface elevation was calculated. The black dashed lines mark the data for which the response amplitudes were calculated. The numerical simulation was stopped before the wave test was over in order to save computational time.

4.2 Sensitivity Analysis

The sensitivity of the response of the internal free-surface calculated with modal theory regarding the prescribed motions was studied. Because of poor agreement between experimental and numerical results, see Section 5.2.2, it was of interest to investigate if this was due to errors in the measured accelerations.

There were no repetitions of the experiment and it was therefore not possible to estimate the precision error of the motions. In addition, the accelerometers were only calibrated once a couple of days before the model test were conducted. Two accelerometers were used to

measure the z-acceleration, while only one accelerometer was used for the x-acceleration. Surge is therefore least reliable. It was therefore of interest to study the calculated modal response of the free-surface elevation when varying the prescribed motions, surge and pitch from the experiment.

The present section gives a description of the procedure in the sensitivity study. Only wave tests with wave steepness $H/\lambda = 1/60$ were investigated. First, the z-position of the z-accelerometers, f_z in Figure 3.2a, was varied. Second, surge was multiplied with a varying amplification factor, $\eta_1 = factor \cdot \eta_{1,Exp}$.

4.2.1   Position of z-accelerometer - f_z

There was some uncertainty related to where on the 2cm high accelerometer the measurement was done. The response of the free-surface elevation at WP2 with $f_z = (8.91 - 12.15)$m in model scale was therefore calculated. The results are presented in Figure 4.2. Varying f_z affects the surge motion, see Equation (3.2).

(a) RAO   (b) Ratio between RAOs
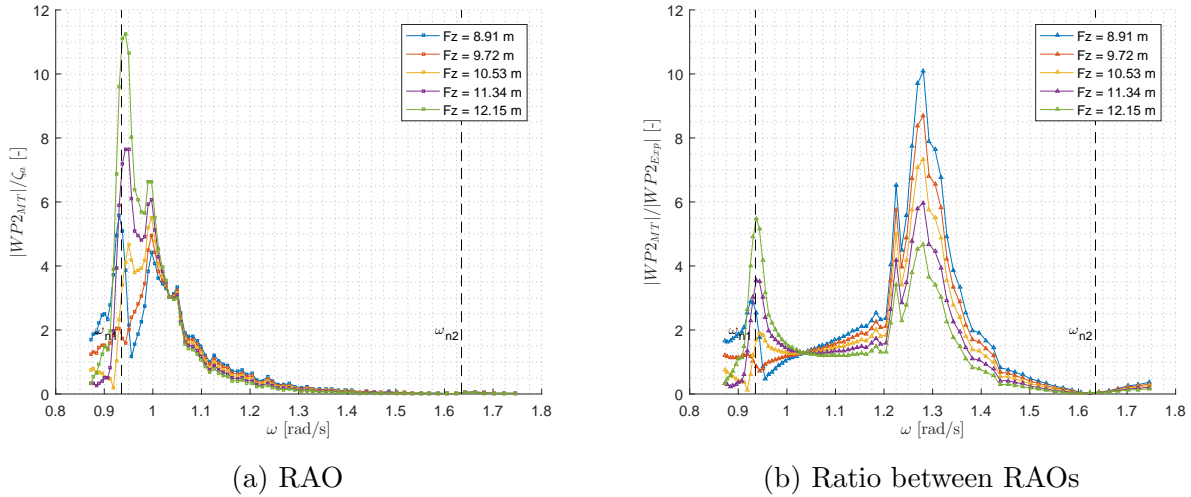
Figure 4.2: Figure (a) shows plots of the calculated first harmonic RAO for the free-surface elevation at WP2 with varying position of the z-accelerometers, f_z. Figure (b) displays the ratio between the numerical and experimental RAOs. The original value of f_z was 11.53m, see Table 3.1. The damping in the modal equations is $\xi = 0.01$. The wave steepness is $H/\lambda = 1/60$ for all runs. The linear natural frequencies of the first and second sloshing modes are the dashed lines marked as ω_{n1} and ω_{n2}, respectively.

Figure 4.2a shows how sensitive the response of the free-surface elevation is near the

natural frequency of the first mode when varying f_z. For $\omega = 0.94$, the response vary from 2m to 11m when $f_z = (8.9 - 12.2)$m. For frequencies larger than 1.05rad/s, the response is rather stable.

In Figure 4.2b at $\omega = 1.03$ there is a point for which the ratio between calculated and experimental RAO for the free-surface elevation at WP2 is constant for varying f_z. Equation (3.2) implies zero pitch motion for the incident wave frequency. There is therefore only surge motion at $\omega = 1.03$rad/s.

4.2.2 Surge Amplification Factor

Surge were multiplied with a factor varying from $0.7 - 1.3$ with step 0.2 while studying the numerical response at WP2. The results are presented in Figure 4.3.

(a) RAO   (b) Ratio between RAOs
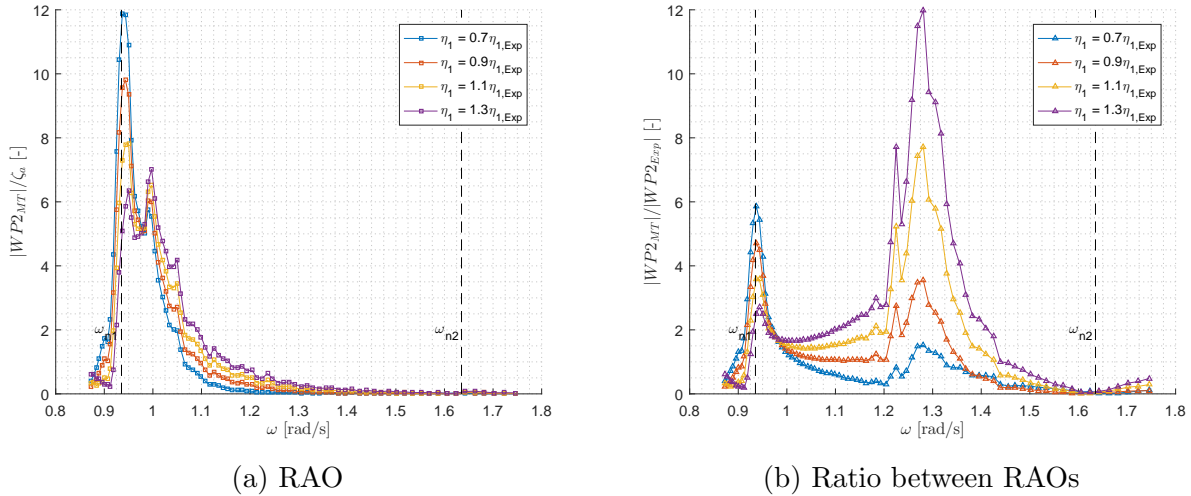
Figure 4.3: Figure (a) shows plot of the calculated first harmonic RAO for the free-surface elevation at WP2 with varying a factor multiplied with surge motion. Figure (b) displays the ratio between the numerical and experimental RAOs. The surge amplification factor varies from $0.7 - 1.3$. The wave steepness is $H/\lambda = 1/60$ for all runs.

Figure 4.3a shows the same trend as Figure 4.2a. The response is very sensitive near the frequency of the first sloshing mode, $\omega = 0.94$rad/s. In Figure 4.3a, the response varies from 6m to 12m when surge is multiplied with a factor of $(0.7 - 1.3)$.

Using a similar argument as above, Figure 4.3b indicates pure pitch for $\omega = 0.98$rad/s, as the ratio between the experimental and numerical RAOs do not change for varying surge

amplification factors.

4.2.3   Correction of Motions

Figure 4.2b and 4.3b both have a point where the ratio between the RAOs does not change for varying f_z and surge.

f_z and the surge amplification factor were chosen such that the ratio between calculated and experimental response of the free-surface elevation at WP2 is equal to unity at the points of pure surge and pitch. This means that the numerical and experimental free-surface elevation are equal for pure surge and pitch motion at the incident wave frequencies. This occurs when $f_z = 9.315$m and $\eta_1 = 0.8\eta_{1,Exp}$ and is shown in Figure 4.4.
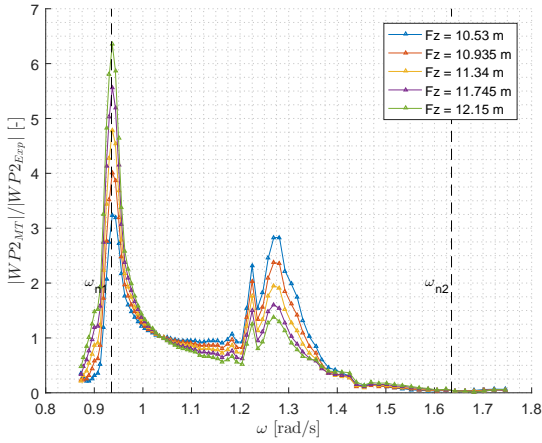
(a) Varying f_z with $\eta_1 = 0.8\eta_{1,Exp}$.   (b) Varying surge with $f_z = 9.315$.
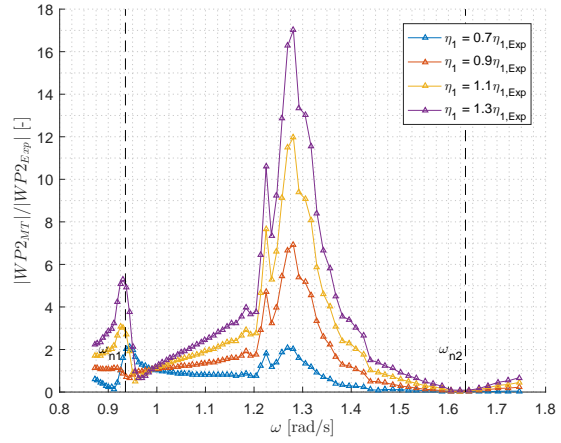
Figure 4.4: Plot of the ratio betweeen the numerical and experimental first harmonic RAOs of the free-surface elevation at WP2. In plot a) f_z is varying and in plot b) surge is varying. The points of pure surge and pitch are now both at $y = 1$. The wave steepness is $H/\lambda = 1/60$ for all runs.

The motions were corrected based on the adjustments of f_z and surge and the free-surface elevation was re-calculated. The final numerical results are presented in Chapter 5.

Chapter 5

Results

The following chapter presents the results and findings from the experiment, numerical calculations before and after adjustments of the motions have been made. Each section is organized by displaying the results followed by a discussion of the findings. A comparison between the calculated and experimental results is done both before and after corrections have been made.

First values of the natural sloshing frequencies are given. Further, the experimental and numerical results before adjustments of motions have been made are presented. For the experiment, this includes the response amplitudes of the free-surface elevation at WP2, surge, pitch and heave, and time series of the free-surface elevation inside the model. The, the results of the numerical free-surface elevation are presented and compared with the experimental results.

Next, the experimental and numerical results after the adjustments of motions have been made are presented. For the experiment, this means the surge motion, as this is the only changed result. The results of the free-surface elevation after the adjustments from the sensitivity study are then presented and also compared with the experimental results.

All the following results are presented in full scale, assuming Froude scaling and geometrical similarity with scale ratio $\lambda = 81$. All free-surface elevations are presented in a body-fixed coordinate system pointing positive upwards with $z = 0$ on the free-surface of the internal tank liquid, see Figure 3.4. The free-surface elevation calculations include only one sloshing mode with damping $\xi = 0.01$ for all calculations. Surge, pitch and heave are

presented according the definitions given in Section 2.1.

Additional results of the experiment are presented in Appendix A.

5.1   Natural Sloshing Frequencies

Table 5.1 presents the natural frequencies of the first and the second sloshing modes for an upright circular cylinder given in Equation (2.16). The geometry of investigation has an internal diameter of 39.6m and an internal water height of 19.2m.

Table 5.1: Full scale natural sloshing frequencies of the cylinder of investigation. The geometry is defined in Table 4.1.

Quantity	Term	Value
Natural frequency of the first sloshing mode [rad/s]	ω_{n1}	0.94
Natural frequency of the second sloshing mode [rad/s]	ω_{n2}	1.64

According to Faltinsen and Timokha (2009) significant sloshing is expected when the system forcing frequency is in the vicinity of lowest natural frequency. In practice, this is when the frequency of the incoming waves in the experiment are in the vicinity of the first natural sloshing frequency, $\omega_{n1} = 0.94$rad/s. The second natural sloshing mode has less energy than the first mode. This can be understood by the fact that the first mode has more mass in motion than the second mode, see Equation (2.29) for the shape of the modes.

The system, the moored model with internal liquid, has a natural frequency in addition to the natural frequencies of the sloshing. As explained in Section 2.3, this is a *coupled* natural frequency due to coupling between the body motions and sloshing. The coupled natural frequency can be found by solving the homogenous equations of motions (see Equation (2.60)). This frequency is expected to affect the response of the free-surface elevation in the following sections.

5.2   Preliminary Results

Preliminary results of the sloshing experiment and the numerical calculations are presented in this section, (i.e. the motions from the experiment are presented as they were measured

originally). The numerical calculations are based on the motions before adjustments have been made.

First, RAOs of the free-surface elevation at WP2, surge, pitch and heave motion are presented. Time series of the free-surface elevation at WP2 for four wave tests with different incoming wave frequencies are also given. Second, the free-surface elevation is calculated, assuming prescribed motions measured during the experiment without any corrections. At the end, a comparison between the numerical and experimental results is given.

5.2.1 Sloshing Experiment

Figure 5.1 displays the first harmonic response of the free-surface elevation at WP2, surge, pitch and heave motions plotted against incoming wave frequency. The RAOs are calculated according to the description in Section 3.2.4. See Appendix A for RAOs of all the wave probes, $WP(1 - 4)$.

Figure 5.1a presents the RAO of the body-fixed free-surface elevation at WP2 for all three wave steepnesses. Significant sloshing occurs for incoming wave frequencies around 1rad/s. For these incoming wave frequencies, the internal wave amplitudes are measured to be approximately $3 - 4.5$ times larger than the amplitudes of the incoming waves. There are also internal waves for $\omega = 1.65$rad/s, but the response amplitude is smaller or equal to the incoming wave amplitude ζ_a.

The two peaks in Figure 5.1a indicates trigging of the first and the second natural sloshing modes, which are marked with black dashed lines in the figure. The sloshing peak is located at $\omega = 1.0$rad/s, which is 6.4% of the calculated natural sloshing frequency of the first mode. This indicates that the frequency for when significant sloshing occurs is affected by coupling with the motions of the system and that the coupled system frequency is $\omega = 1.00$rad/s. See Section 2.3 for more details about the coupled system. The location of the calculated natural sloshing frequency of the second mode coincide with the response in the experiment.
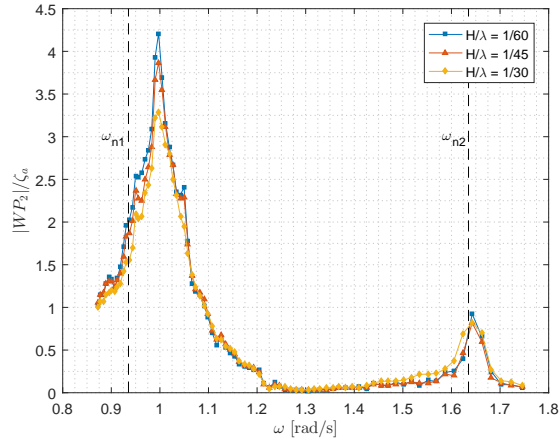
(a) Body-fixed free-surface elevation at $WP2$.
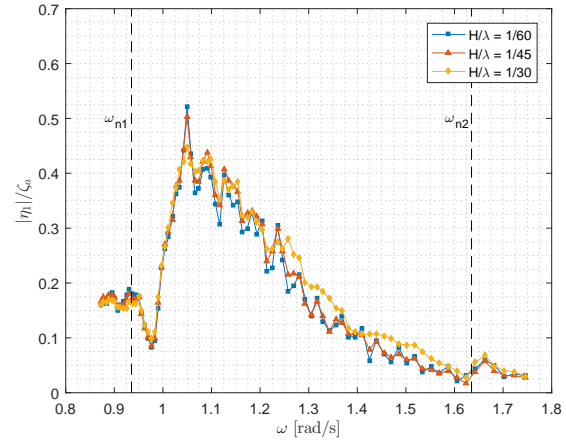
(b) Surge motion
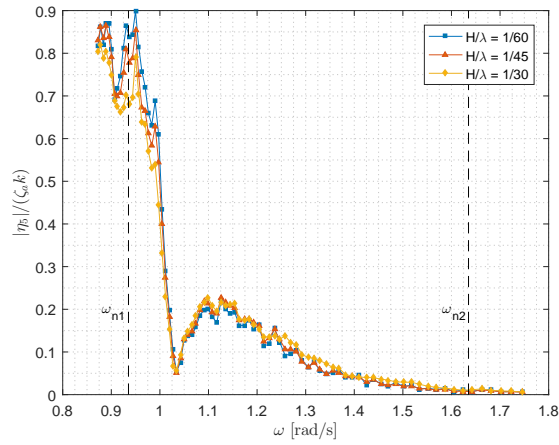
(c) Pitch motion
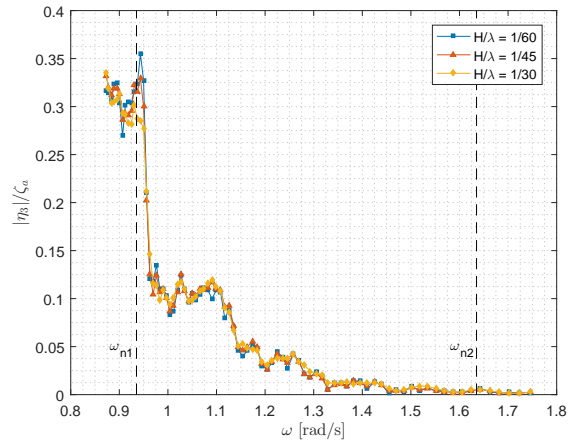
(d) Heave motion

Figure 5.1: First harmonic response amplitudes for the body-fixed free-surface elevation at WP2, surge, pitch and heave motion. WP2, surge and heave are made dimensionless by dividing by incoming wave amplitude and pitch is divided with $k\zeta_a$. ω is incoming wave frequency. Each plot has data for three wave steepnesses, $H/\lambda = \{1/60, 1/45, 1/30\}$. The linear natural frequencies of the first and second sloshing modes, ω_{n1} and ω_{n2}, are marked with dashed lines in the plots.

Surge and pitch in Figure 5.1b and 5.1c have a drop for $\omega = 0.98 \mathrm{rad/s}$ and $\omega = 1.03 \mathrm{rad/s}$, respectively. For pure surge motion the linear sloshing force is either $0 \deg$ or $180 \deg$ out of phase with the surge motion. This can be seen from Equation (2.38). For pure surge motion the expression for the linear sloshing force only contains the terms $\ddot{\eta}_1$ and $\ddot{\beta}_j$. $\ddot{\eta}_1$ is $180 \deg$ out of phase with surge and $\ddot{\beta}_j$ will either be $0 \deg$ or $180 \deg$ out of phase with the surge motion, since this is an undamped oscillator. According to linear sloshing theory, if only

surge motion was allowed, the sloshing force would cause zero surge for $\omega = \omega_{n1}$, while in reality, due to damping, the surge motion will have a minimum in the vicinity of ω_{n1} which can be seen from the results in Figure 5.1c. A similar argument regarding sloshing force and cancellation can be made for pure pitch motion. The points of pure surge and pitch found in the sensitivity analysis in Section 4.2 corresponds with the points of minimum surge and pitch in Figure 5.1b and 5.1c.

For incoming wave frequency $\omega = 1\mathrm{rad/s}$, large-amplitude sloshing occurs and this violates the assumption of small surface elevations in Figure 2.3. Rognebakke and Faltinsen (2003) found that the linear sloshing model fails in predicting the frequency of minimum sway motion for pure sway motion, since large amplitude sloshing at resonance invalidates the assumption of a constant natural frequency for the internal fluid motion.

Finally, Figure 5.1d shows the response of heave motion for all three wave steepnesses. The heave motion increase with decreasing incoming wave frequency reaching a non-dimensional value of 0.3 at the frequency of the first natural sloshing mode. According to linear sloshing theory heave cannot excite sloshing, while heave can excite sloshing according to non-linear sloshing theory. The slight drops in the heave RAO at $\omega = 1.00\mathrm{rad/s}$ and $\omega = 1.15\mathrm{rad/s}$ indicates resembles the wall effects shown in Figure 3.9.

Figure 5.2 displays time series of WP2 for four different wave tests. Case (a) has beating, while the other wave tests have steady oscillations.
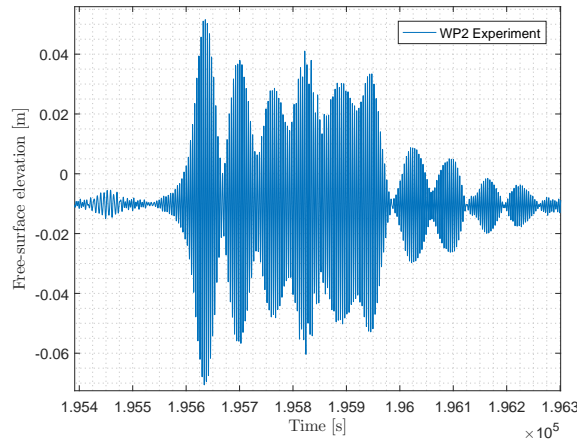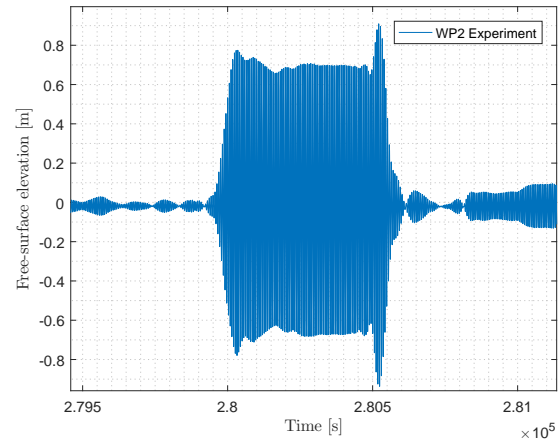
(a) $\omega = 1.55\text{rad/s}$ (b) $\omega = 1.07\text{rad/s}$
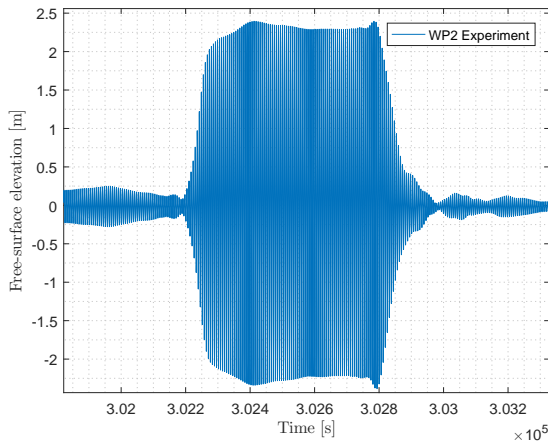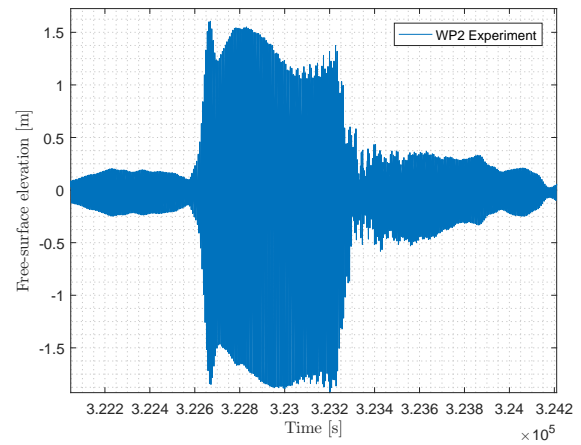
(c) $\omega = 1.00\text{rad/s}$ (d) $\omega = 0.94\text{rad/s}$

Figure 5.2: Time series of the raw signal at WP2 for four wave tests with incoming wave frequency ω with wave steepness $H/\lambda = 1/45$.

Comparing WP2 and WP4

Figure 5.3 displays the first harmonic body-fixed free-surface elevation measured at WP2 and WP4, see Figure 3.2b for locations of the wave probes. The responses of the two wave probes coincide well for all frequencies. Measurements from WP2 are used for further investigation in the present work.
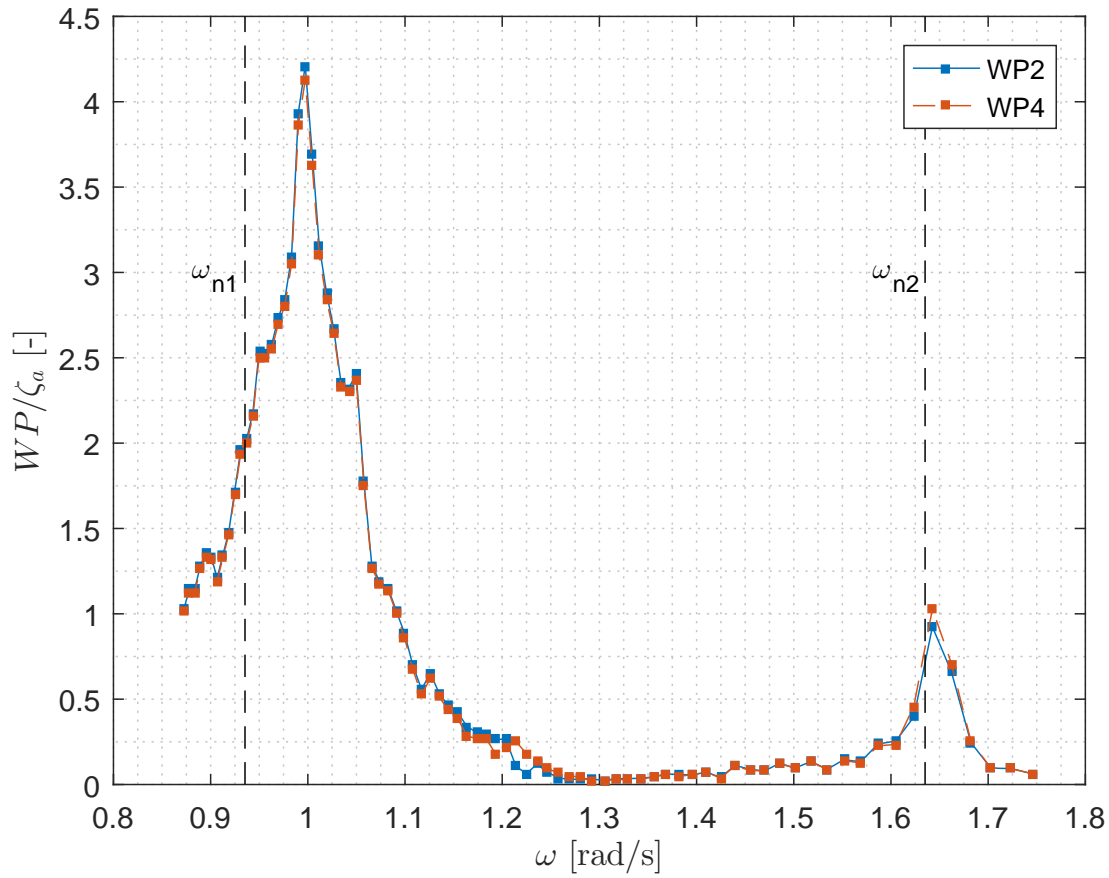
Figure 5.3: First harmonic response amplitude operator of the body-fixed free-surface elevation at WP2 and WP4 with wave steepness $H/\lambda = 1/60$. ω is incoming wave frequency. The linear natural frequencies of the first and second sloshing modes are marked as ω_{n1} and ω_{n2}, respectively.

Anchoring Forces

Figure 5.4 shows the first harmonic in-line force responses of mooring line 1 and 2 for all three wave steepnesses. The forces has a minimum for $\omega = 1$rad/s, which is the same frequency as when significant sloshing occurs. This is due to the sloshing force cancelling surge and pitch motions, as explained in Figure 5.1b and 5.1c. Minimum surge and pitch occur for $\omega = 0.98$rad/s and $\omega = 1.03$rad/s. The mooring forces are affected by the local coupled motion at the fixing points of the mooring lines, see Equation (2.10), which is at a minimum at $\omega = 1$rad/s.

(a) Mooring line 1   (b) Mooring line 2
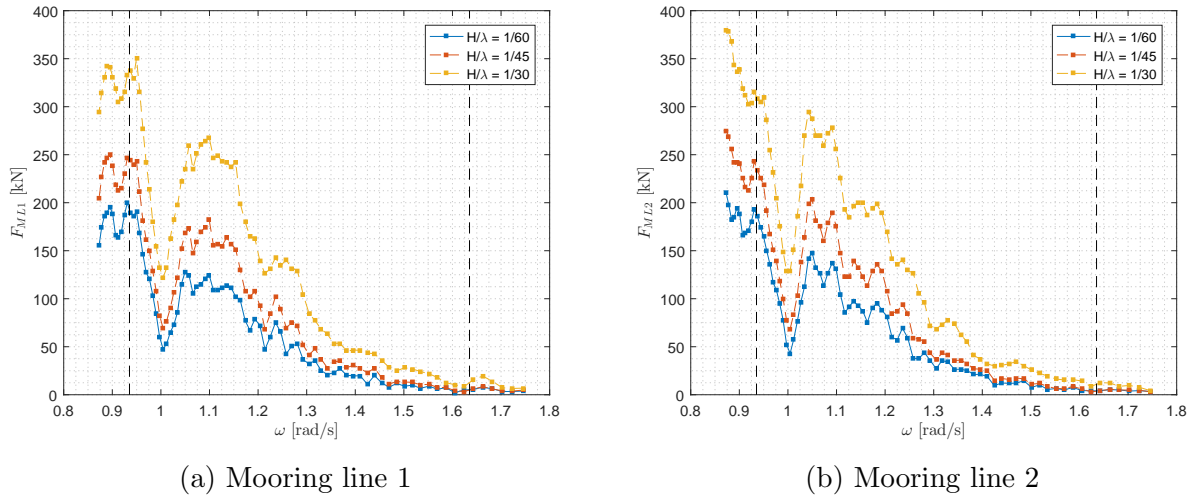
Figure 5.4: First harmonic response amplitudes for force in mooring line 1 and 2 for all three wave steepnesses, see Figure 3.2b for locations of the force sensors.

5.2.2 Numerical Calculations

The following section presents the free-surface elevation according to modal theory. The response was calculated as described in Section 4.1, assuming prescribed motions measured in the experiment, without any corrections, and with damping $\xi = 0.01$. Only the response of the first sloshing mode was included in the calculations.

Figure 5.5 shows the calculated and experimental time series of the first harmonic signal of WP2 for all three wave steepnesses. In the beginning of the time series the response is small, modal theory has no peak for small wave frequencies. This is because only the first sloshing mode was included in the calculations. The response calculated with modal theory follows the increasing trend of the experiment well, but when the response in the experiment start decreasing, the response from the modal theory continues to grow.
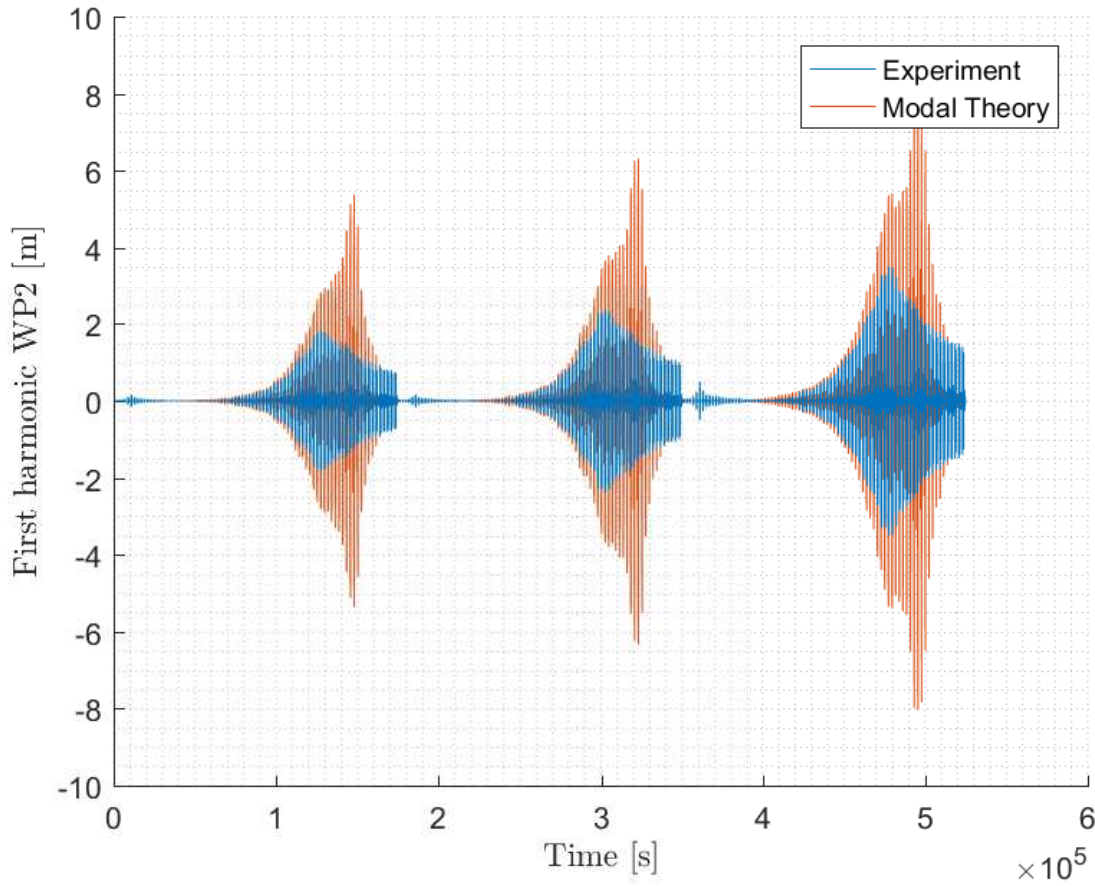
Figure 5.5: Time series of the first harmonic response of the body-fixed free-surface eleva-tion at WP2 from the experiment and modal theory calculations. There are three wave steepnesses, each with 81 wave tests with wave periods in the range $3.6 - 7.2$s.

Figure 5.6 is based on the time series of the response calculated with modal theory in Figure 5.5 and shows the first harmonic response amplitudes for the free-surface elevation at WP2, for all three wave steepnesses, assuming prescribed motions. For comparison, the experimental RAOs for the free-surface elevation at WP2 for all three wave steepnesses, (Figure 5.1a), are plotted with dashed lines. The numerical response has peaks for incoming wave frequencies $\omega = 0.94$rad/s and $\omega = 1.00$rad/s, while the corresponding response from the experiment only has a peak for $\omega = 1.00$rad/s. The two peaks are related to the natural sloshing frequency of the first mode and the natural system frequency.
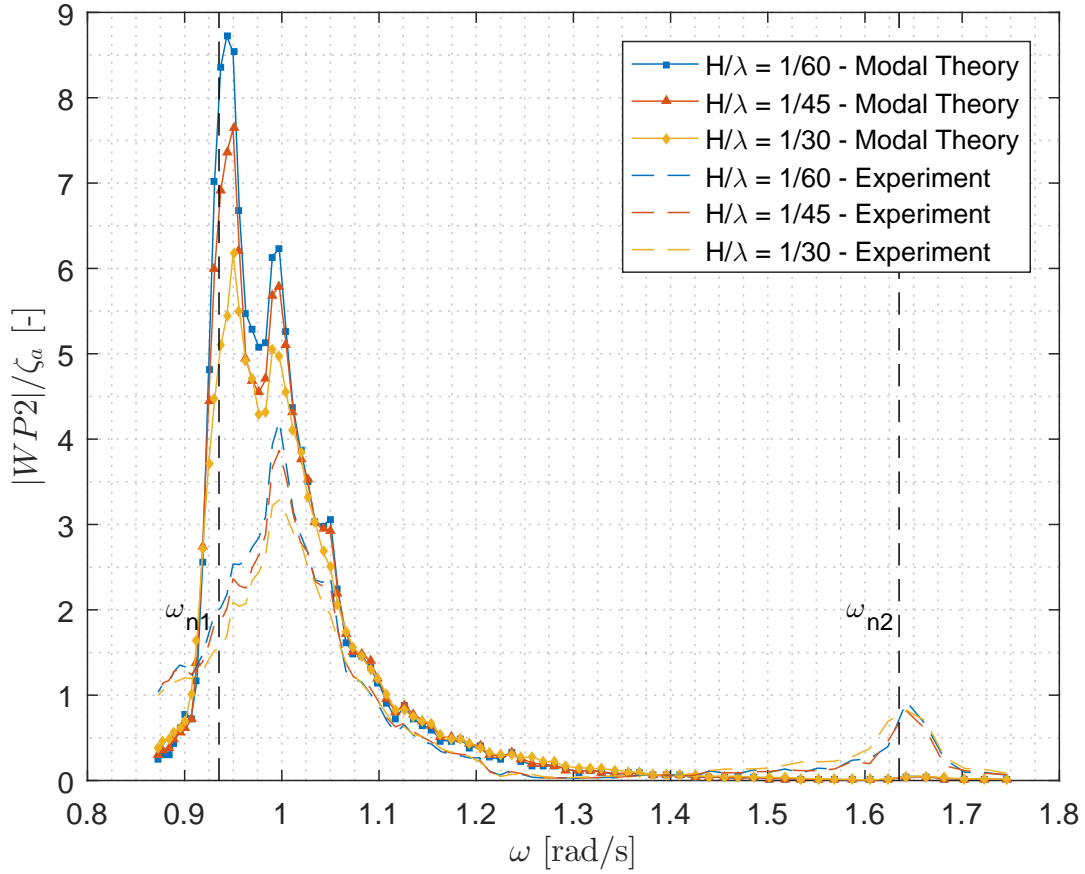
Figure 5.6: Response amplitude operators of first harmonic body-fixed free-surface elevation at WP2 calculated by modal theory assuming prescribed original motions measured in the experiment. For comparison, the experimental RAOs of the free-surface elevation are plotted with dashed lines. The linear natural frequencies of the first and second sloshing modes, ω_{n1} and ω_{n2}, are marked with dashed lines.

In figure 5.7, the phase difference between the two time series in Figure 5.5, the experimental and numerical free-surface elevation, is given. For incoming wave frequencies $\omega = 1.02 - 1.2\text{rad/s}$, the phase difference is $-20\,\text{deg}$. The experimental and numerical free-surface elevation at WP2 correspond well for these wave frequencies. For the natural frequency of the first sloshing mode, $\omega = 0.94\text{rad/s}$, the numerical response amplitude at WP2 in Figure 5.6 is four times larger than the experimental value. For frequencies larger than 1.2rad/s the response is small and this leads to large percentage error between the numerical and experimental results. For frequencies larger than 1.5rad/s the numerical response are in poor agreement with the experimental measurements, this is because only the

first sloshing mode was included in the numerical calculations.
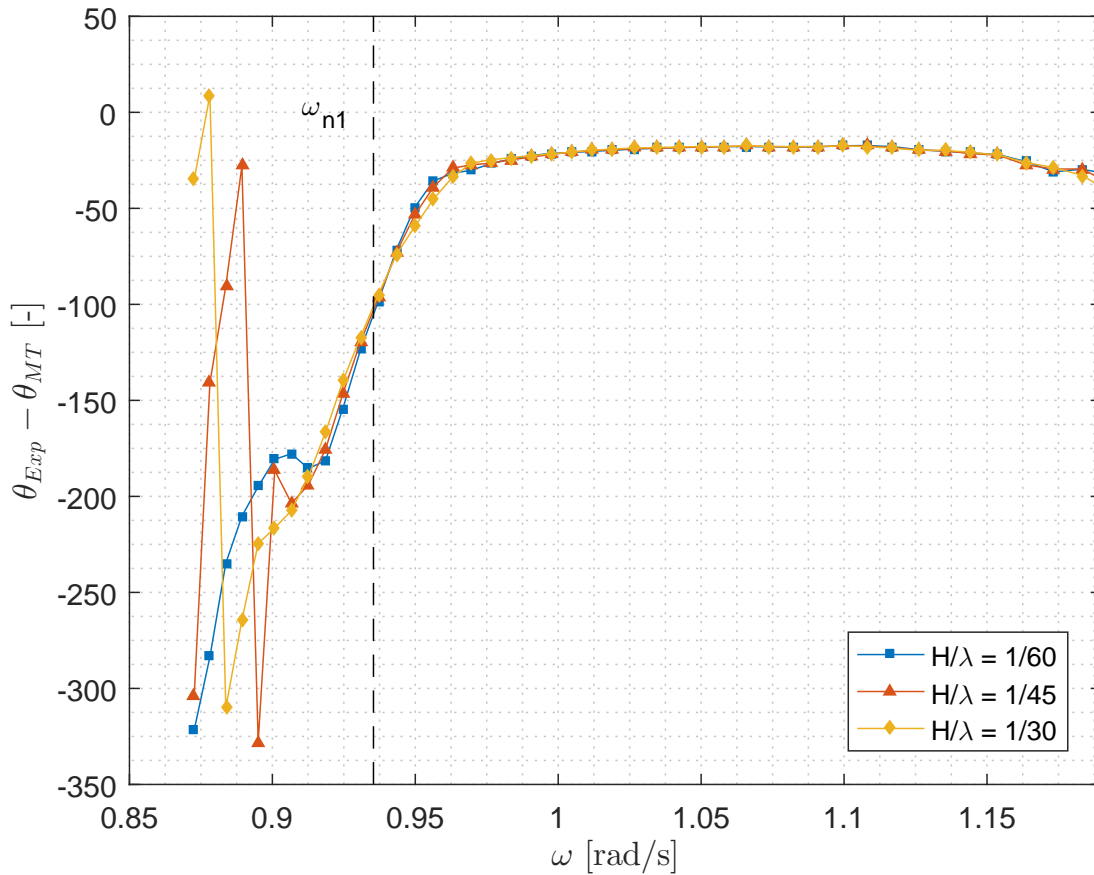
Figure 5.7: Phase difference between experimental and calculated results of the first harmonic response of the body-fixed free-surface at $WP2$. All three wave steepnesses are plotted.

Time series of the calculated and experimental first harmonic body-fixed free-surface elevation at WP2 from two wave tests are presented in Figure 5.8. Figure 5.8a and 5.8b shows that the calculated free-surface elevation does not become steady during the simulated time. In Figure 5.8b, the incoming wave frequency is equal to the first natural sloshing frequency. According to modal theory the sloshing response is infinite for forcing with frequency equal to the first natural sloshing frequency. This is illustrated in Figure 2.5c. In Figure 2.6c it was shown that it takes 500s for the response to become steady, i.e. the beating oscillations die out, when the damping coefficient is $\xi = 0.01$ in the modal equations (2.28). While the experimental response in Figure 5.8b are steady after approximately 130s. This indicates

that the damping in the numerical calculations for frequency $\omega = 0.94$rad/s is too small, or that energy in the experiment was transferred from the first mode to higher modes.

Figure 5.8c and 5.8d display time series of the experimental and numerical response at WP2 for the same two wave tests as Figure 5.8a and 5.8b. The phase differences, which is found in Figure 5.7, are -20 deg and -98 deg for $\omega = 1.00$rad/s and $\omega = 0.94$rad/s, respectively.

(a) $\omega = 1.00$rad/s

(b) $\omega = 0.94$rad/s

(c) $\omega = 1.00$rad/s

(d) $\omega = 0.94$rad/s
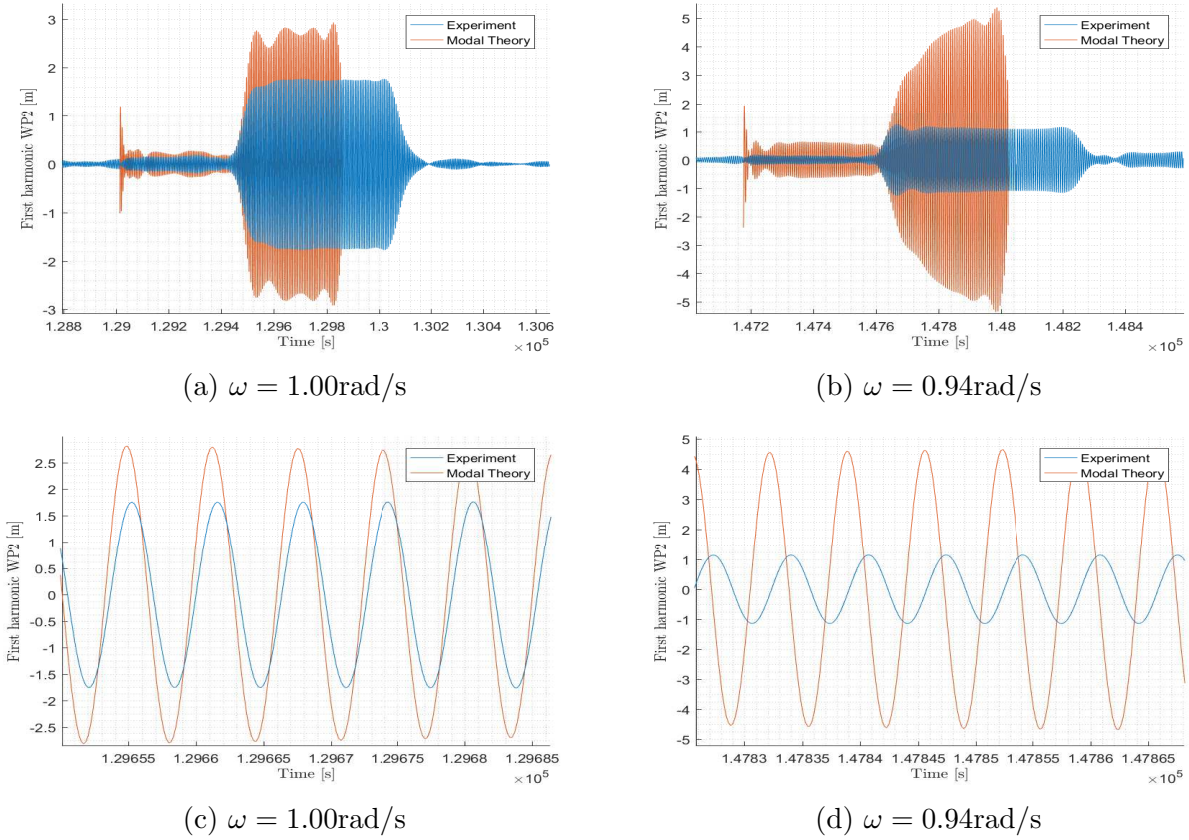
Figure 5.8: Times series of calculated and experimental first harmonic free-surface elevation for incoming wave frequency ω and wave steepness $H/\lambda = 1/60$. The damping is $\xi = 0.01$. The numerical simulation is stopped before the wave test is over to save computational time.

5.3 Corrected Results

The motions in the sloshing experiment are now re-analysed with corrected motions as described in Section 4.2; $\eta_1 = 0.8\eta_{1,Exp}$ and $f_z = 9.315$m. Table 5.2 gives an overview of the corrections and their original values in full scale.

Table 5.2: Full scale corrections of motions. η_1 is the surge motion and f_z the z-position of the z-accelerometers in body-fixed coordinates.

Quantity	Orignal value	Corrected value
f_z	11.58m	9.32m
η_1	η_1	$0.8\eta_1$

The corrections affect the surge motion and the experimental response amplitude operator of the surge motion are therefore re-presented. Further, the response of the free-surface at WP2 was re-calculated based on the corrected motions and presented. Only wave steepness $H/\lambda = 1/60$ was investigated for the numerical calculations, as the corrections of motions were based on this wave steepness.

5.3.1 Sloshing Experiment

Surge is now multiplied with 0.8 and $f_z = 9.315$m. Only surge motion is affected by the corrections and is therefore presented here. The other results, all but the RAO of surge, are as presented in Section 5.2.1.

The RAO of corrected surge motions is presented in Figure 5.9. The drop in surge motion at $\omega = 0.98$rad/s is now slightly more rounded compared to before corrections were made (see Figure 5.1b).
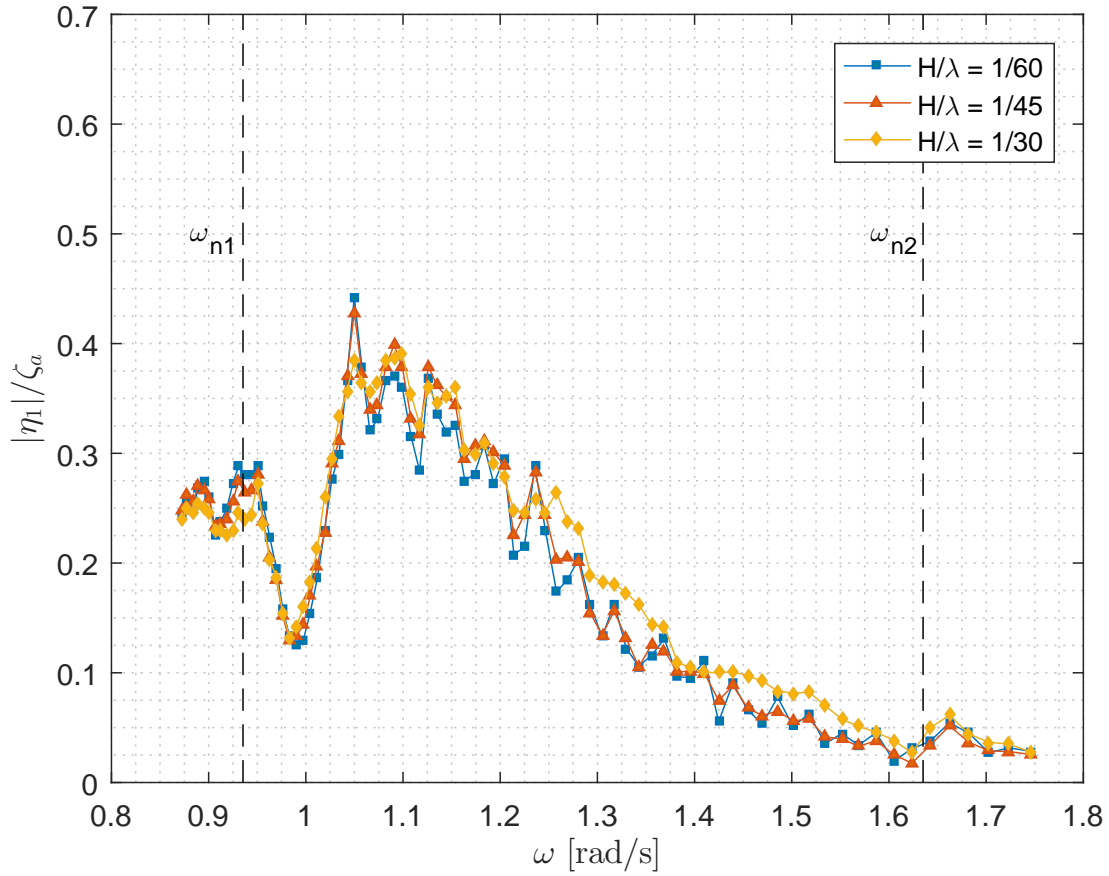
Figure 5.9: RAO of first harmonic surge motion for all three wave steepnesses after adjustments of motions have been made. The linear natural frequencies of the first and second sloshing modes are marked as ω_{n1} and ω_{n2}, respectively.

5.3.2   Numerical Results

The free-surface elevation at WP2 for wave steepness $H/\lambda = 1/60$ was calculated with the corrections from Section 4.2; $\eta_1 = 0.8\eta_{1,Exp}$ and $f_z = 9.315$m. The response was calculated as described in Section 3.2.4, assuming prescribed corrected motions and with damping $\xi = 0.01$. Only the response of the first sloshing mode was included in the calculations.

Figure 5.10 shows the calculated and experimental time series of the first harmonic free-surface elevation at WP2 for wave steepness $H/\lambda = 1/60$. The peak in the time serie calculated by the modal theory in is now gone, comparing with Figure 5.5.
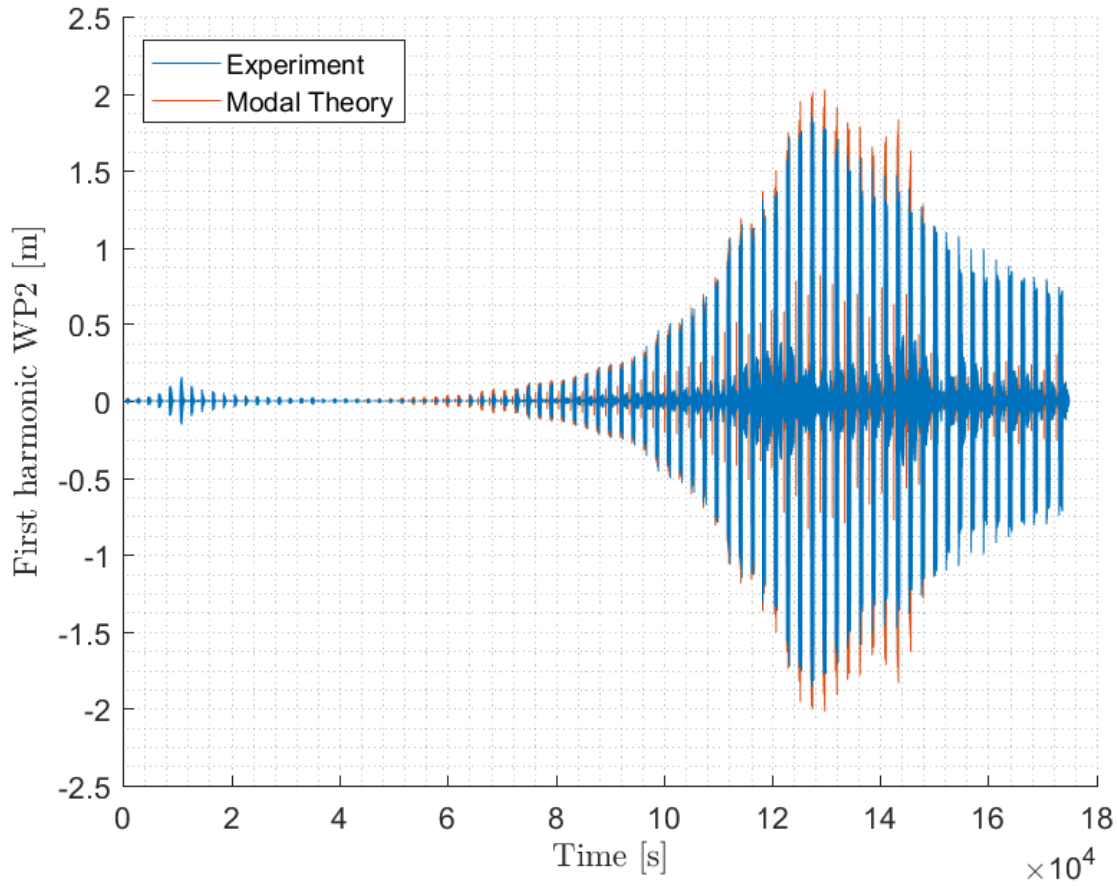
Figure 5.10: Time series of the first harmonic response of WP2 from the experiment and modal theory after adjustments of the motions have been made for wave steepness $H/\lambda = 1/60$.

The RAO of the calculated free-surface elevation at WP2 for wave steepness $H/\lambda = 1/60$ is presented in Figure 5.11. For comparison, the experimental RAO is also plotted with dashed lines. The peak in numerical response at $\omega = 0.93$rad/s is gone and has been replaced with a drop, compared to the response before the correction of motions presented in Figure 5.6. This indicates that the response of the free-surface is sensitive of the prescribed motions in vicinity of the lowest natural sloshing frequency. In addition, the sloshing response is smaller for wave frequencies around $\omega = 1$rad/s. Sloshing is not triggered in the numerical calculations at the natural frequency of the second mode, this is because only the first mode was included in the calculations.
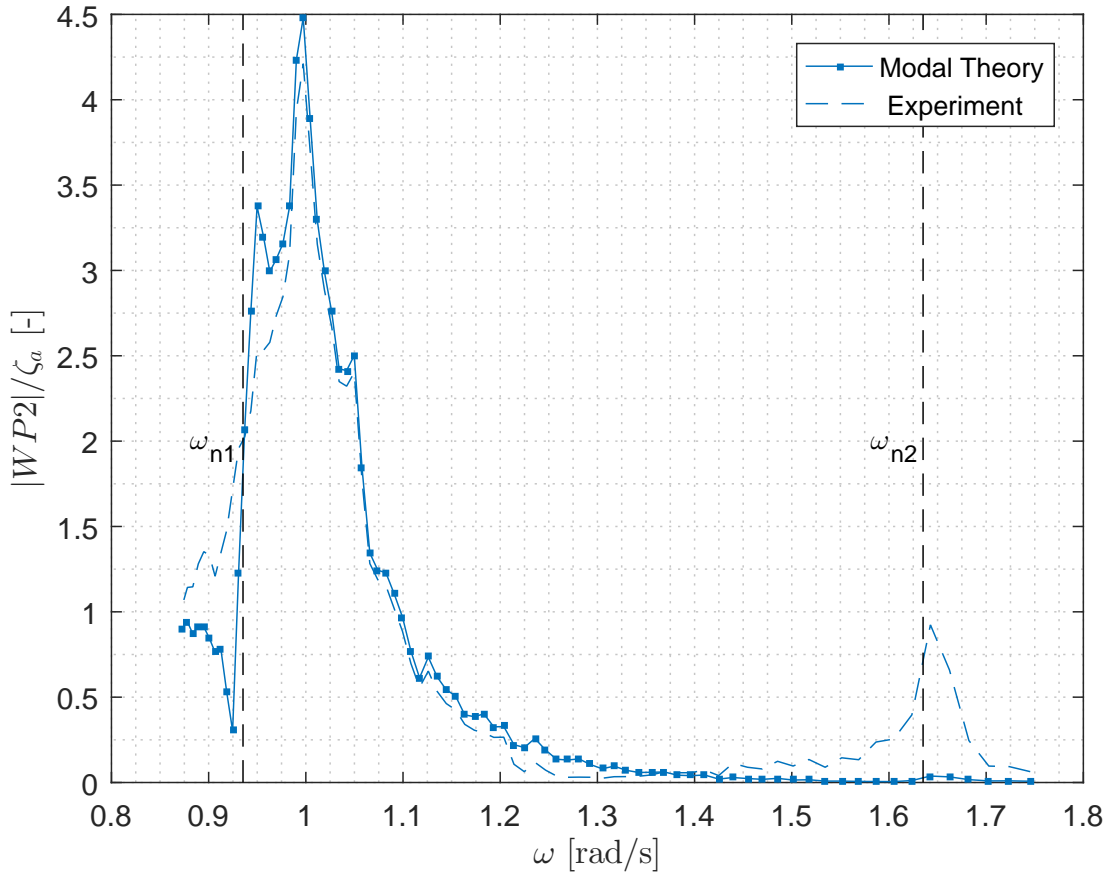
Figure 5.11: RAO of the calculated first harmonic of the free-surface elevation at WP2 for wave steepness $H/\lambda = 1/60$ after adjustments of the motions have been made (see Section 4.2). Corrections of the prescribed motions $\eta_1 = 0.8\eta_{1,Exp}$ and $f_z = 9.315$m are applied. For comparison, the experimental RAO is plotted with dashed lines.

The numerical response amplitudes in Figure 5.11 do now coincide better with the experimental results for a large frequency domain, $\omega = (0.97 - 1.2)$rad/s and the numerical results gives good predictions of the severe sloshing occuring at $\omega = 1$rad/s.

The phase difference between the numerical and experimental free-surface elevation at WP2, after adjustments of the motions have been made, is displayed in Figure 5.12. The phase difference still has a jump at $\omega = \omega_{n1}$, the natural frequency of the first sloshing mode. For $\omega = (0.97 - 1.2)$rad/s, the phase difference is -20 deg. One possible reason for the -20 deg phase difference, is delay between the logging of accelerations and free-surface elevation at the wave probes. The phase difference cannot be explained at the current point and needs further investigation.
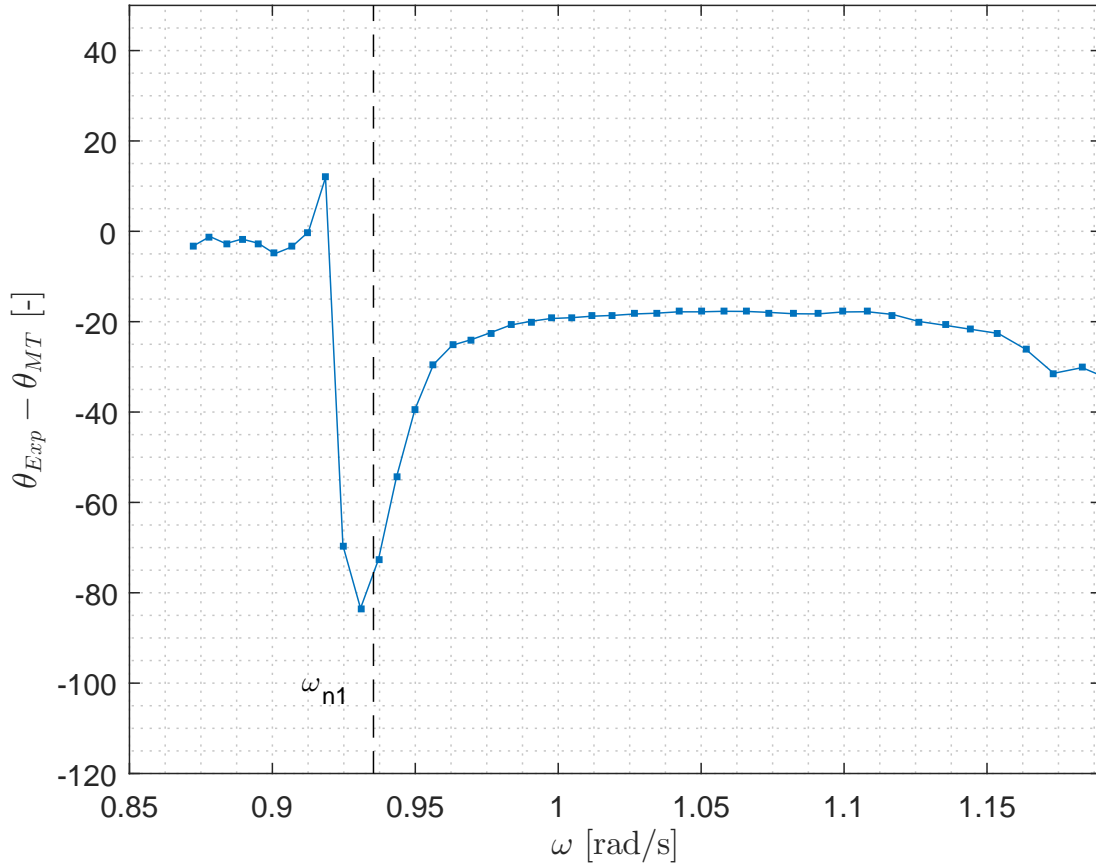
Figure 5.12: Phase difference between numerical and experimental first harmonic body-fixed free-surface elevation at WP2 for wave steepness $H/\lambda = 1/60$ after adjustments of the motions have been made (see Section 4.2).

Time series of the first harmonic calculated and experimental free-surface elevation at WP2 from two wave tests are presented in Figure 5.13. See Figure 5.8 for comparison of the same time series before the adjustments of the motions are made. The calculated free-surface elevation in Figure 5.13b does now become steady during the simulation and is not increasing linearly with time as in Figure 5.8b. This indicates that the calculated free-surface elevation is sensitive regarding to surge motion.
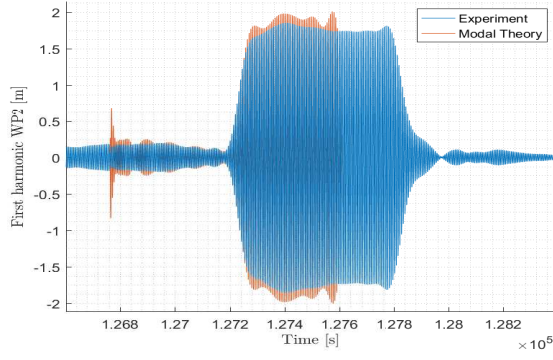
(a) $\omega = 1.00\text{rad/s}$
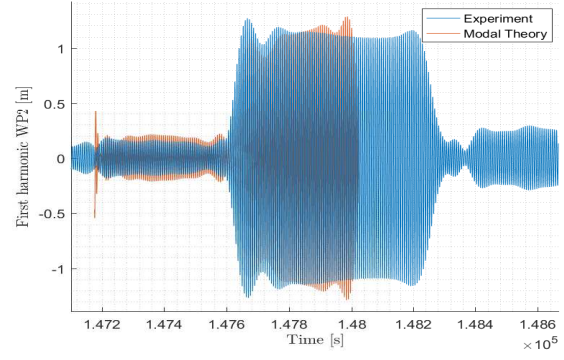
(b) $\omega = 0.94\text{rad/s}$
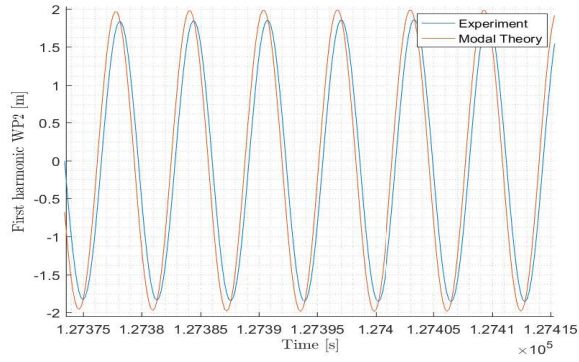
(c) $\omega = 1.00\text{rad/s}$
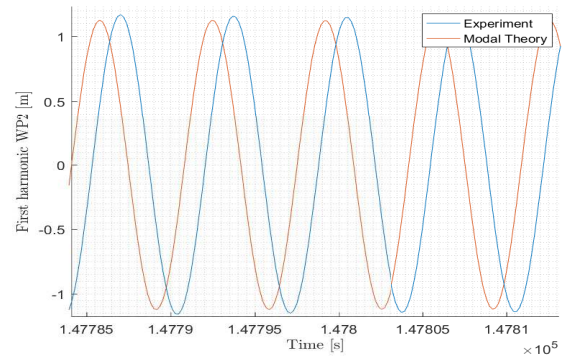
(d) $\omega = 0.94\text{rad/s}$

Figure 5.13: Times series of calculated and experimental first harmonic free-surface elevation for incoming wave frequency ω and wave steepness $H/\lambda = 1/45$ after adjustments of the motions have been made. Damping is $\xi = 0.01$. The numerical simulation is stopped before the wave test is over to save computational time.

Chapter 6

Discussion

Although significant improvement was made with the corrections of the body motions, the numerical and experimental results for the free-surface at WP2 do not fully agree in the vicinity of the natural frequency of the first sloshing mode, neither before nor after corrections have been made. This indicates that linear modal sloshing theory is not able to simulate the experimental free-surface elevation at WP2 correctly by assuming prescribed motions measured during the experiment. The following chapter continue to study the experimental results and a discussion of possible reasons for the difference between the numerical and experimental results is given.

First, time series of the free-surface elevation at all the wave probes were studied regarding swirling. Transverse waves inside the model was observed during the experiment and it is therefore of interest to study swirling. Second, nonlinearities are investigated for the experimental internal free-surface elevation.

The aim of this chapter is to investigate to what extent, and for which tests, the criteria of linear modal theory is satisfied in the experiment, and for those that do not satisfy the linear criteria well, to identify the main reasons for this.

6.1   Swirling Analysis

Swirling was investigated by plotting time series of the free-surface elevation inside the model measured by WP1-4. Swirling is rotary wave motions and may occur during harmonic hor-

izontal excitation of liquid motion in symmetric tanks when the forcing period is near the highest natural period (Faltinsen and Timokha, 2009).

(a) $\omega = 1.64\text{rad/s}$

(b) $\omega = 1.00\text{rad/s}$

(c) $\omega = 0.97\text{rad/s}$

(d) $\omega = 0.94\text{rad/s}$
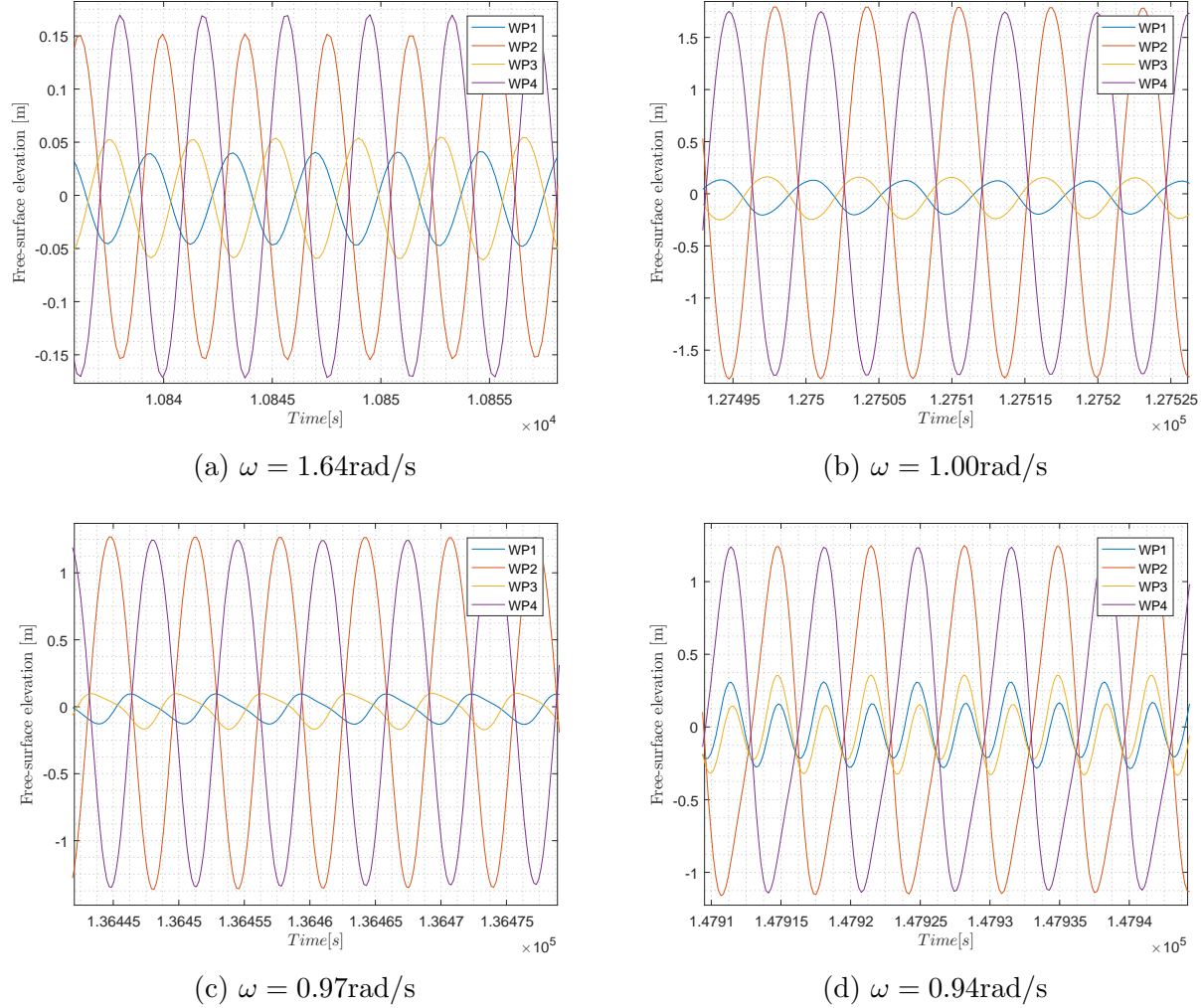
Figure 6.1: Full scale time series from the experiment of the free-surface elevation of the raw signal of WP(1-4) in body-fixed coordinates for four wave tests with wave steepness $H/\lambda = 1/60$. Notice the varying amplitude for wave probes 1 and 3 in (b) and how the wave elevation at wave probe 2 and 4 are skewed. This indicates nonlinear free-surface elevation.

Figure 6.1 shows time series of four wave tests with four different wave frequencies at $H/\lambda = 1/60$. If there was no swirling for any of the wave tests, the wave probes {WP1,WP3} and {WP2,WP4} would be either in phase or 180 deg out of phase with each other. In Figure 6.1c, the wave probes are 90 deg out of phase and this indicates swirling. The rotating wave is small, as the elevations at WP1 and WP3 are small. The phase between the wave probes vary for each incoming wave frequency in Figure 6.1. This indicates that both longitudinal

and transverse waves inside the model, as well as swirling, occurs simultaneously for some of the wave tests.

6.2   Nonlinear Analysis

Following section investigates nonlinear effects of the experimental free-surface elevation inside the model. The aim of the section is to identify whether the free-surface elevation is nonlinear and for what wave frequencies the nonlinearities occur.

First, time series of the free-surface elevation were studied with respect to nonlinearities. Examples of nonlinear free-surface elevation at WP2 from the experiment are given in Figure 6.2.
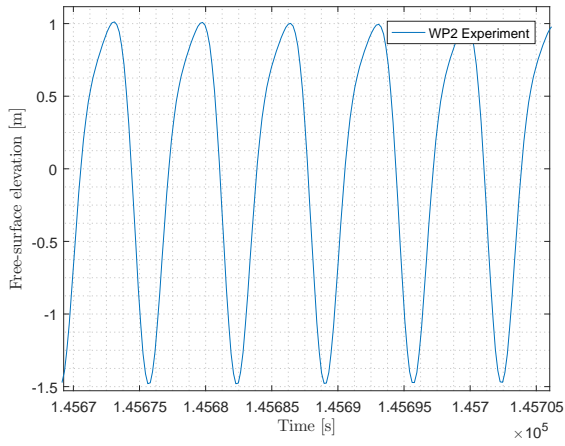
(a) $H/\lambda = 1/60$
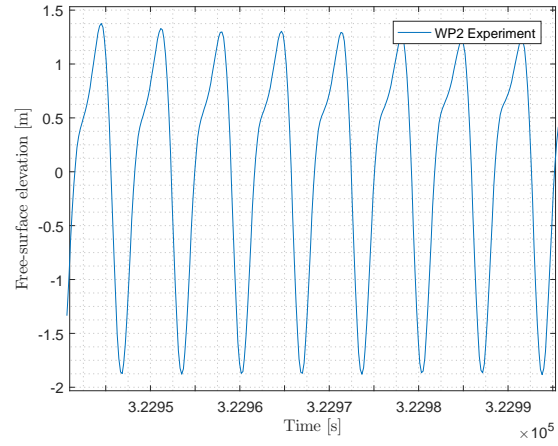
(b) $H/\lambda = 1/45$
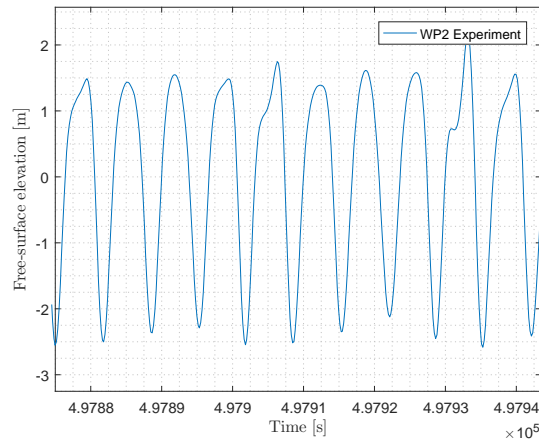
(c) $H/\lambda = 1/30$

Figure 6.2: Time series of the raw signal from the experiment of WP2 at $\omega = 0.94 \text{rad/s}$ for the three different wave steepnesses. The free-surface elevation is clearly nonlinear for all three wave steepnesses, and the nonlinearities becomes more pronounced with increasing wave steepness.

Further, the first and second harmonic response amplitudes for wave probe 2 for all three wave steepnesses were plotted. Second harmonic wave components are present in the vicinity of the natural sloshing frequency of the first mode, $\omega = 0.94 \text{rad/s}$ for all three wave steepnesses.
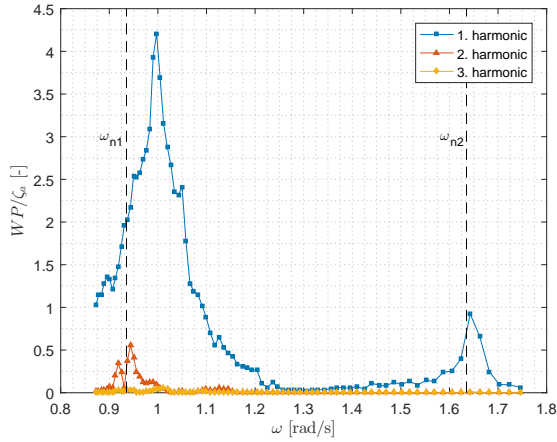
(a) $H/\lambda = 1/60$
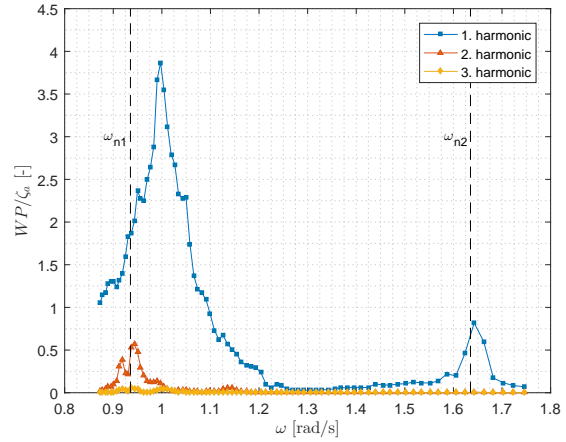
(b) $H/\lambda = 1/45$
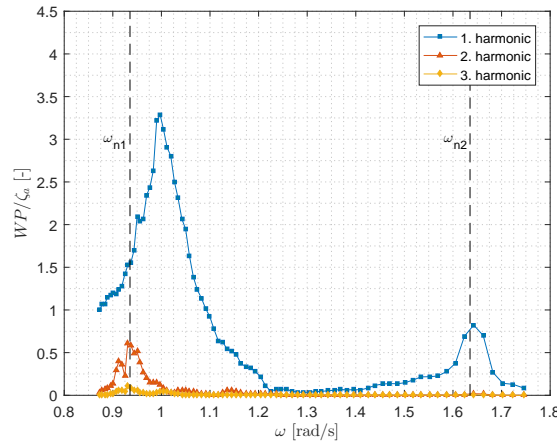
(c) $H/\lambda = 1/30$

Figure 6.3: RAOs for the first, second and third harmonics of the experimental body-fixed free-surface elevation at WP2 for all three wave steepnesses. All the harmonic components are linearized by dividing with the incoming wave amplitude, ζ_a.

Figure 6.4 displays the RAOs of the first and second harmonics of the experimental body-fixed free-surface elevation at WP2 for all three wave steepnesses, for better comparison of the data in Figure 6.3.

The ratios between the values of the RAO for the first and second harmonics at $\omega = 0.94$rad/s are in the range of $(0.25 - 0.33)$ for the three steepnesses. To evaluate whether the second harmonics of WP2 are significant, i.e. if the nonlinearities are significant, one must consider the kinetic energy of the first and the second modes. If the response amplitudes of the first and second harmonics were the same, the second harmonic would have more energy

because this wave component has double as large frequency, 2ω, as the first harmonic wave component.
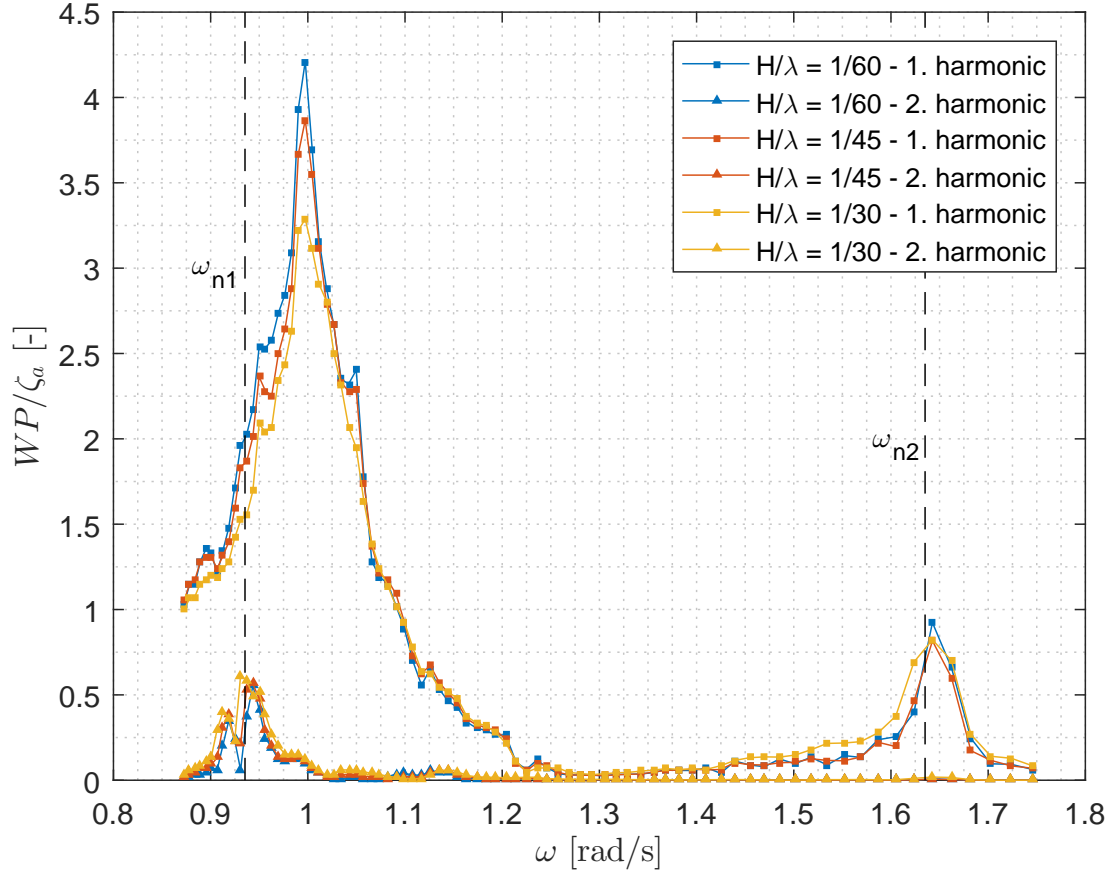
Figure 6.4: RAOs of the first and second harmonics of the experimental body-fixed free-surface elevation at WP2 for all three wave steepnesses. The linear natural frequencies of the first and second sloshing modes are marked as ω_{n1} and ω_{n2}, respectively.

In Figure 6.4, for $\omega = 0.94\text{rad/s}$ the second harmonic response is approximately the same for all wave steepness, while the first harmonic response clearly decreases. This illustrates how the energy is transferred to higher modes in the vicinity of the natural frequency of the first sloshing mode due to nonlinear effects and indicates that other additional wave components are present. The spectrums of the raw signal for the body-fixed free-surface elevation at WP2 for $\omega = 0.94\text{rad/s}$ for all the wave steepnesses were therefore inspected and presented in Figure 6.5. Figure 6.5 shows that for increasing wave steepness, more of the energy are transferred to higher frequencies other than 2ω components. This is the reason

why the first harmonic response in Figure 6.4 decreases for increasing wave steepness, while the 2ω components are approximately the same. This corresponds with the time series in Figure 6.2, where the nonlinearities are more pronounced with increasing wave steepness.

(a) $H/\lambda = 1/60$

(b) $H/\lambda = 1/45$

(c) $H/\lambda = 1/30$
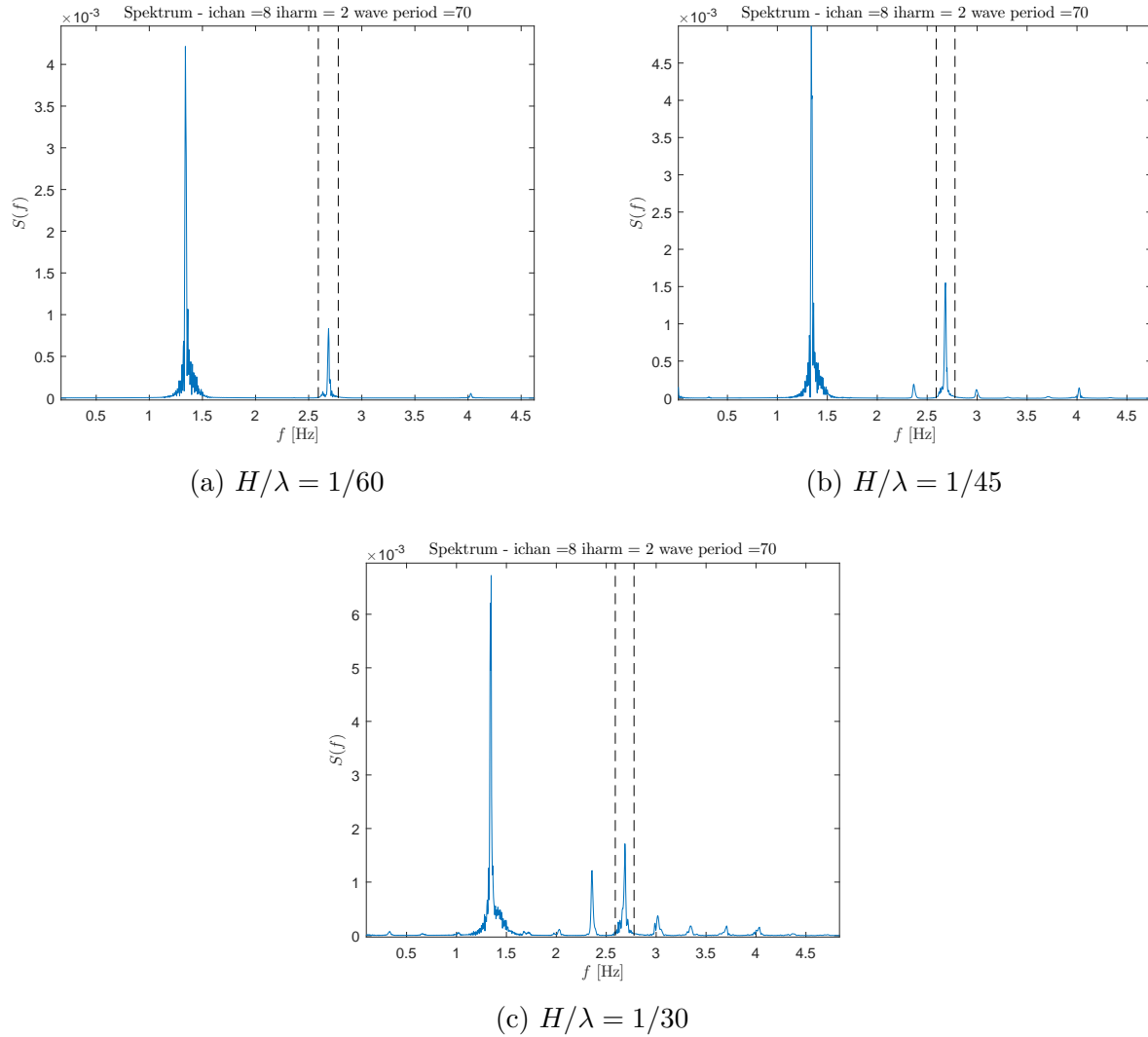
Figure 6.5: Spectrum of time series of the body-fixed free-surface elevation at WP2 for $\omega = 0.94$rad/s. The dashed lines show the cutoff frequencies in the bandpass filtering for the second harmonic RAOs. Notice that more wave components are present with increasing wave steepness.

Figure 6.6 displays the first, second and third harmonics of the body-fixed free-surface elevation at WP1 for wave steepness $H/\lambda = 1/60$. As mentioned above, if the response amplitude of the first and second harmonic free-surface elevation were the same, would the 2ω wave component contain more energy. The plot shows that the second harmonic response

of the free-surface elevation is approximately 0.4 for $\omega = 0.94$rad/s, the natural sloshing frequency of the first mode, while the first harmonic response is only 0.1. The nonlinear effects are therefore clearly dominating at WP1 in the vicinity of the natural sloshing frequency of the first mode.
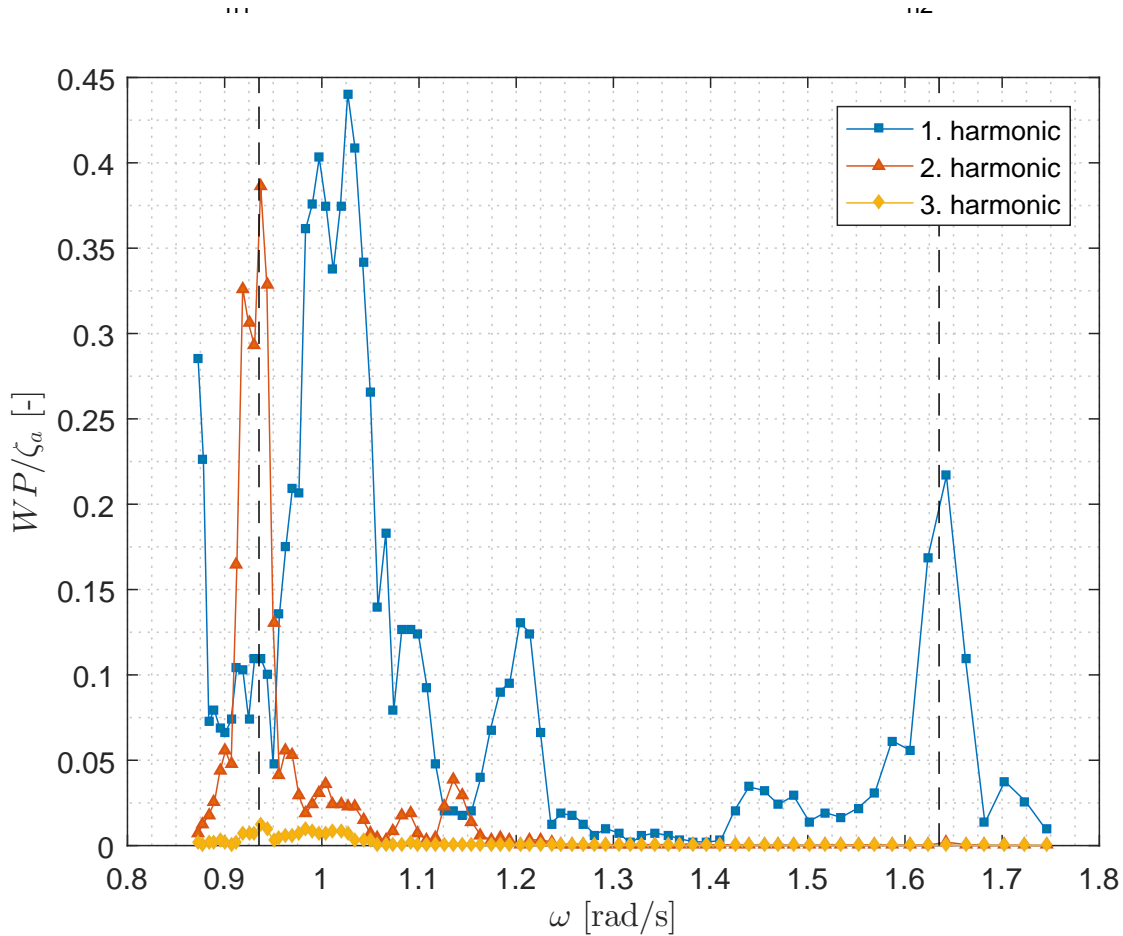
Figure 6.6: RAOs of the first, second and third harmonic body-fixed free-surface elevation at WP1 for wave steepness $H/\lambda = 1/60$. The linear natural frequencies of the first and second sloshing modes are marked as ω_{n1} and ω_{n2}, respectively.

The nonlinear analysis shows that nonlinearities are present in the experimental free-surface elevation inside the fish cage for $\omega = (0.90-0.97)$rad/s. This violates the assumptions of linear modal theory. In addition, the sensistivy of the sloshing response according to linear modal theory is high for these frequencies. Linear modal theory can therefore not predict the sloshing response in the vicinity of the natural frequency of the first sloshing mode.

Chapter 7

Summary

This final chapter summarizes the present work and its most important findings. At the end a recommendation to possible extensions of the work is given.

7.1   Summary and Conclusions

In the present work, sloshing inside closed aquaculture plants at sea has been investigated by the means of experimental work and linear sloshing theory.

For the first objective, the hydrodynamics of a closed fish cage were presented assuming linear potential theory. The internal liquid was described by linear sloshing theory. A linearized boundary value problem of the internal tank liquid was formulated for an upright circular cylinder with a flat bottom and the natural sloshing modes and frequencies were found. Second, the dynamics of a closed aquaculture plant was described considering two degrees of freedom, surge and pitch.

The second objective is met in Chapter 3 and 5. The experiment investigating sloshing inside a closed aquaculture plant subjected to regular waves performed during fall 2016 was presented. A 1:81 scale model of an upright circular cylinder with full scale internal diameter of 38.9m and internal water height 19.2m was considered.

Violent sloshing occurs for incoming wave frequency $\omega = 1\text{rad/s}$, which is 6.4% higher than the calculated natural sloshing frequency of the first mode. This is due to coupling with the motions of the model. For $\omega = 1\text{rad/s}$, the body-fixed internal free-surface elevation

amplitude is $3-4$ times larger than the incoming wave amplitudes. Sloshing is also triggered for $\omega = 1.64$rad/s, but here the body-fixed free-surface elevation inside the model is lower than the amplitudes of the incoming waves. It is the natural frequency of the first mode that is of primary practical interest.

Surge and pitch motions both have a minimum near the frequency of when violent sloshing occur, $\omega = 1$rad/s. This is because the sloshing force cancels the motions.

The next objective was to create a numerical simulation of the free-surface elevation inside the plant assuming prescribed motions of the plant measured in the experiment. The numerical calculations overpredicted the sloshing response and the results were not satisfactory. This lead to the fifth objective; a sensitivity analysis of the numerical free-surface elevation inside the model regarding the prescribed motions were performed. The sensitivity of the response of the free-surface elevation calculated with modal theory is high in the vicinity of the natural frequency of the first mode regarding the prescribed motions.

Based on the sensitivity study, the motions were corrected. The numerical response amplitudes of the internal body-fixed free-surface elevation coincided with the experimental ones for a large frequency domain after adjustments of the motions were made. The violent sloshing response at $\omega = 1$rad/s are predicted well by the numerical calculations.

In the vicinity of the natural frequency of the first sloshing mode, the numerical and experimental results for the free-surface elevation inside the model do not fully agree, neither before nor after corrections of the motions have been made. Based on this, swirling and nonlinearities inside the model were investigated.

The swirling analysis indicated that both longitudinal and transverse waves inside the model, as well as swirling, occurs simultaneously for some wave tests.

Investigation of the second harmonic response amplitudes of the experimental body-fixed free-surface elevation inside the model showed that significant nonlinearities were present in the vicinity of the natural frequency of the first sloshing mode. For these frequencies, energy was transferred to higher modes and this is not modelled by linear sloshing theory. This agrees with Faltinsen and Timokha (2009), that resonant sloshing easily becomes nonlinear and linear sloshing theory therefore has strong limitations when it comes to estimating sloshing response near the natural frequency of the first sloshing mode. However, for nonresonant

sloshing it gives useful results for a large frequency domain.

The sixth objective has not been met as it was more troublesome than first assumed to simulate the internal free-surface elevation using modal theory.

7.2 Recommendations for Further Work

Suggestions to possible extensions of the present work follows.

A fully coupled analysis for surge, pitch and sloshing should be performed. A possible approach for the coupled analysis is given in Section 2.3, to use WAMIT to solve flow outside the fish cage and linear sloshing theory for the internal flow. The coupled natural frequency should be compared with the results from the experiment. If the results do not agree, nonlinear sloshing theory should be utilized for the internal flow problem.

Other, suggestions to extensions of the work is to conduct more experimental investigations. The experimental model could be fitted with one additional x-accelerometer and the same experiment as presented in the present work should be repeated. Based on the repeated experiments, the precision error of the motions could be calculated and a new sensitivity analysis of the numerical internal free-surface elevation regarding the prescribed motions could be performed. The uncertainty of the response of the numerical free-surface could then be found. Also, a new experiment with the same set-up, but replacing the water of the model with corresponding weights, could be carried out to investigate more closely the effect of sloshing on the response of the motions of the closed aquaculture cage.

Further, knowledge about for what frequencies violent sloshing occur with respect to the design parameters of the closed aquaculture plant would be of great practical interest for the industry. It is therefore suggested to perform a parameter study, investigating how the design parameters affect the natural sloshing frequency of the first sloshing mode and the natural frequency of the coupled system. Coinciding natural frequencies should be avoided for all designs. Suggestion of interesting parameters to study could be the cage diameter, internal water height, floater dimensions and mooring system.

Bibliography

Brugrand, C. S. (2015). Verdens største lukkede oppdrettsmerd. *Bergens Tidende*. Retrieved from `http://www.bt.no/`. Accessed 10.12.2016.

Cengel, Y. A. and Cimbala, J. M. (2010). *Fluid Mechanics - Fundamentals and Applications*. MCGraw-Hill, 2nd edition.

Chen, B.-F. and Chiang, H.-W. (2000). Complete two-dimensional analysis of sea-wave-induced fully non-linear sloshing fluid in a rigid floating tank. *Ocean Engineering*, 27.

Faltinsen, O. M. (1990). *Sea loads on Ships and Offshore Structures*. Cambridge University Press.

Faltinsen, O. M. and Timokha, A. N. (2009). *Sloshing*. Camebrigde University Press, 1st edition.

Fredriksson, D. W., Tsukrov, I., and Hudson, P. (2008). Engineering investigation of design procedures for closed containment marine aquaculture systems. *Aquacultural Engineering*, 39.

ICES (2017). Report of the working group on north atlantic salmon (wagnas). Technical report, International Council for the Exploration of the Sea. 29 March - 7 April 2017, Denmark, Copenhagen, ICES CM 2017/ACOM: 20, 296 pp.

Klebert, P., Lader, P., Gansel, L., and Oppedal, F. (2012). Hydrodynamic interactions on net panel and aquaculture fish cages: A review. *Ocean Engineering*, 58.

Kreyszig, E. (2006). *Advanced Engineering Mathematics*. John Wiley and Sons, 9th edition.

Kristiansen, T. (2016). Hydro 1. Lecture notes.

Kristiansen, T. and Faltinsen, O. M. (2014). Experimental and numerical study of an aquaculture net cage with floater in waves and current. *Journal of Fluids and Structures*, 54.

NS9415, N. S. Flytende oppdrettsanlegg, krav til lokalitetsundersøkelse, risikoanalyse, utforming, dimensjonering, utførelse, montering og drift.

Rognebakke, O. F. and Faltinsen, O. M. (2003). Coupling of sloshing and ship motions. *Journal of Ship Research*, 47.

Rosten, T. W., Terjesen, B., Ulgenes, Y., Henriksen, K., Biering, E., and Winther, U. (2013). Lukkede oppdrettsanlegg i sjø- økt kunnskap er nødvendig. *Vann*, 01.

SINTEF (2016). Sjøflo - sjøegenskaper og forankring til flytende lukkede oppdrettsanlegg. Retrived from `http://www.sintef.no/prosjekter/sjoflo/`. Accessed 21.05.2017.

Soltveit, T. (2016). Status utviklingskonsesjoner – innovasjonsbølgen slår inn over oppdretterne. *kyst.no*. Retrived from `http://kyst.no/nyheter/status-pa-utviklingskonsesjoner-innovasjonsbolgen-slar-inn-over-oppdretterne/i`. Accessed 20.06.2017.

Steen, S. (2014). *TMR7 Experimental Methods in Marine Hydrodynamics*. NTNU Institutt for Marin Teknikk.

Strand, M. I., Sørensen, J. A., Lader, P., and Volent, Z. (2013). Modelling of drag forces on a closed flexible fish cage. *9th IFAC Conference on Control Applications in Marine Systems*.

Appendix A

Experimental Graphs

A.1 Time series

Time series of the experimental data of incoming waves, surge, heave and pitch are presented.

A.1.1 Incoming Waves
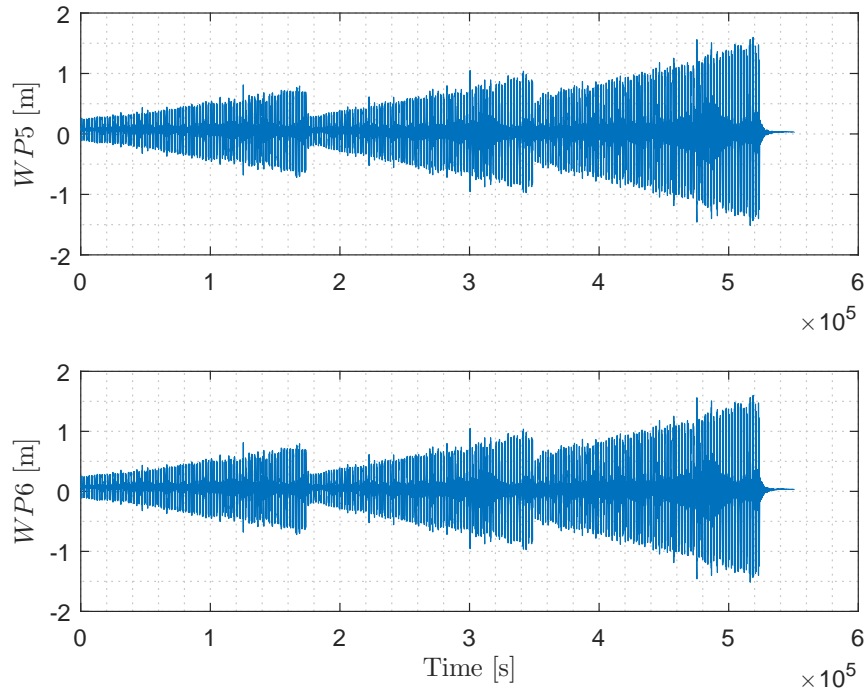
Figure A.1: Full scale time series of the incoming waves at WP5 and WP6.

A.1.2   Surge
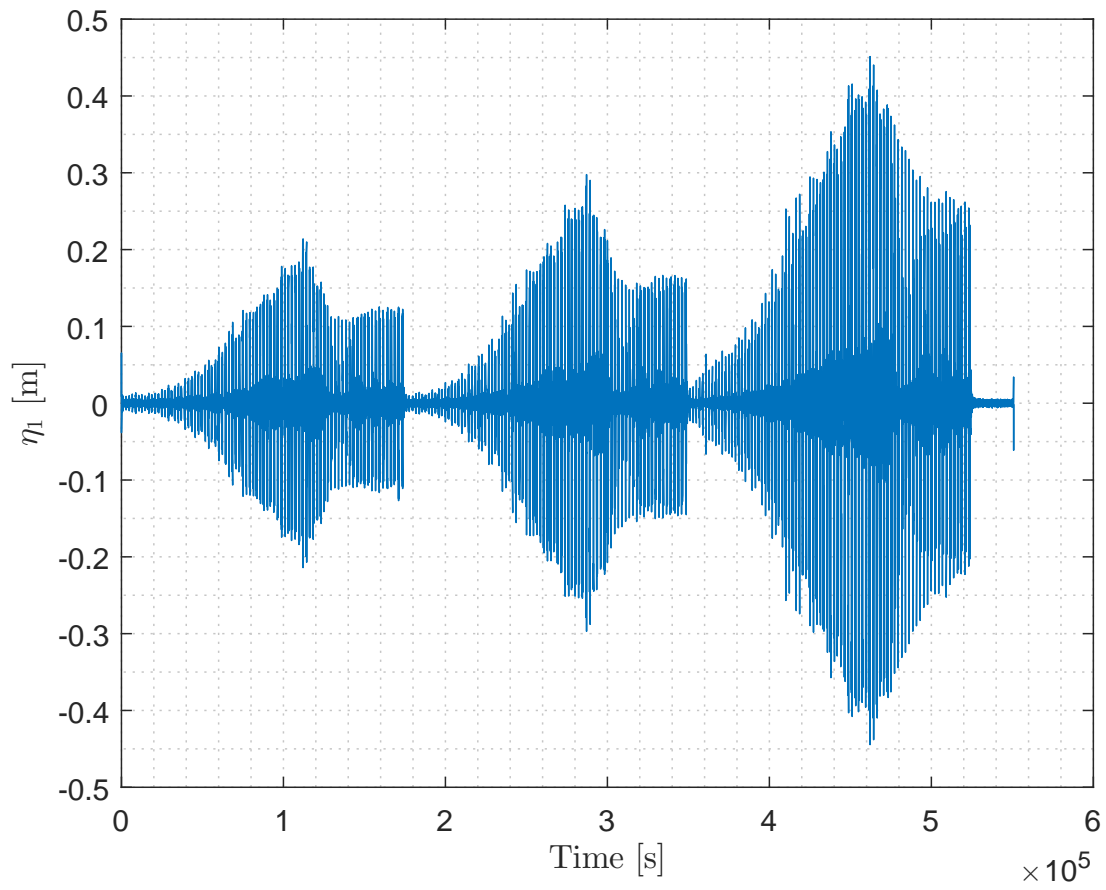
Figure A.2: Full scale time series of surge before adjustments have been made.

A.1.3 Heave
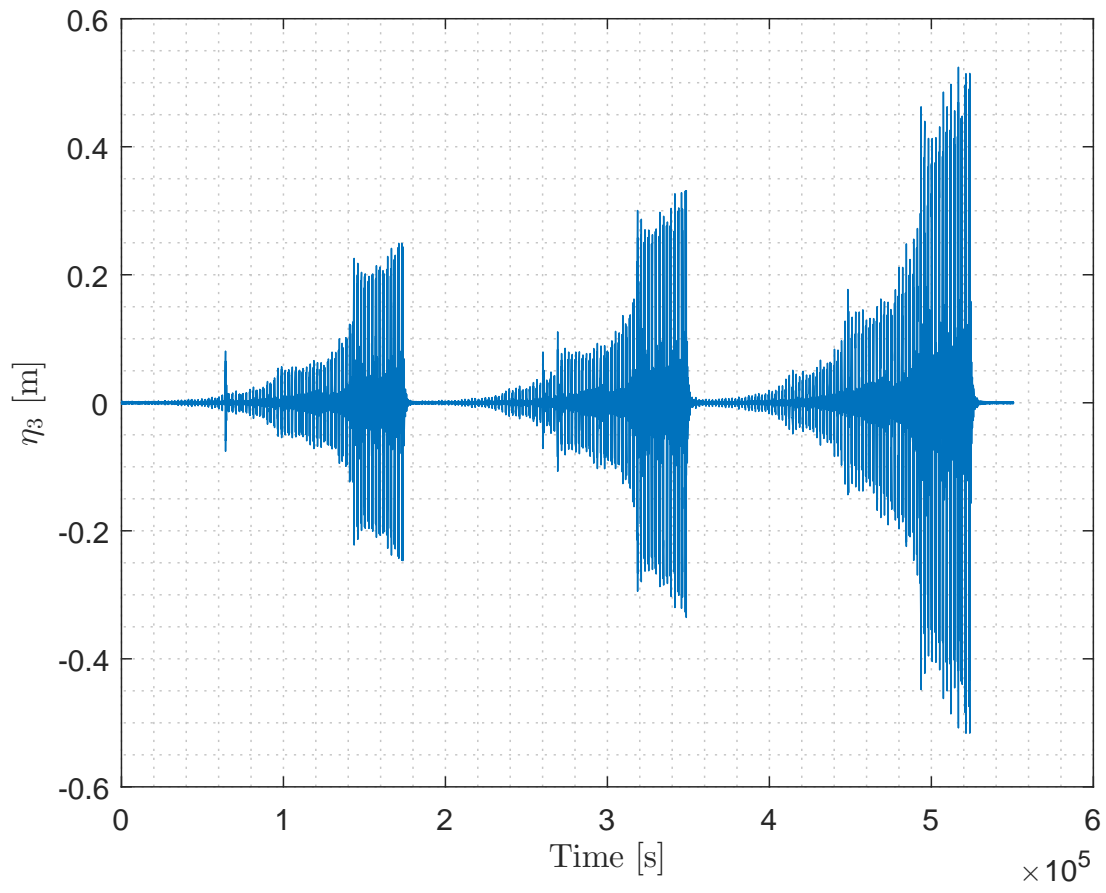
Figure A.3: Full scale time series of heave.

A.1.4 Pitch
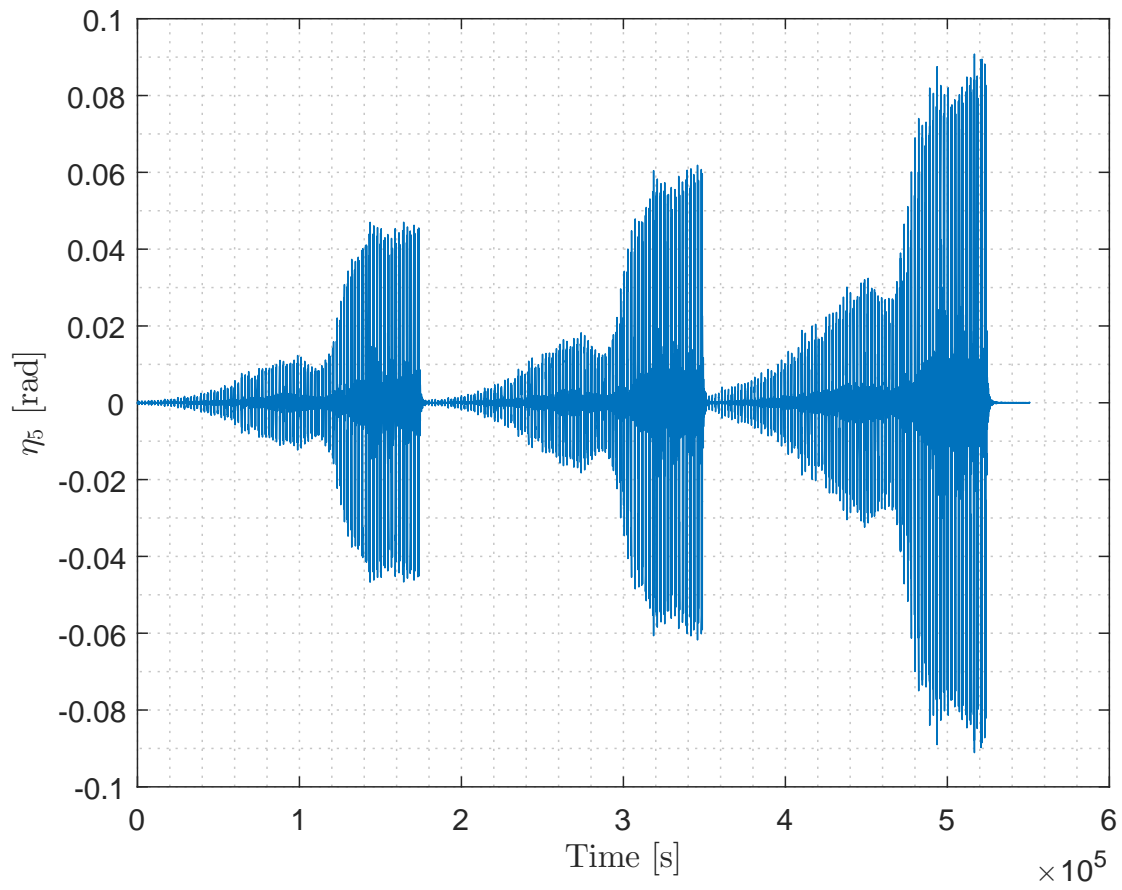
Figure A.4: Full scale time series of pitch.

A.2   Response Amplitude Operators

Plots of the first, second and third harmonic of the body-fixed free-surface elevation at WP(1-4) for all three wave steepnesses are given below. Further, the plot of the first, second and third harmonics of surge, heave and pitch are given.
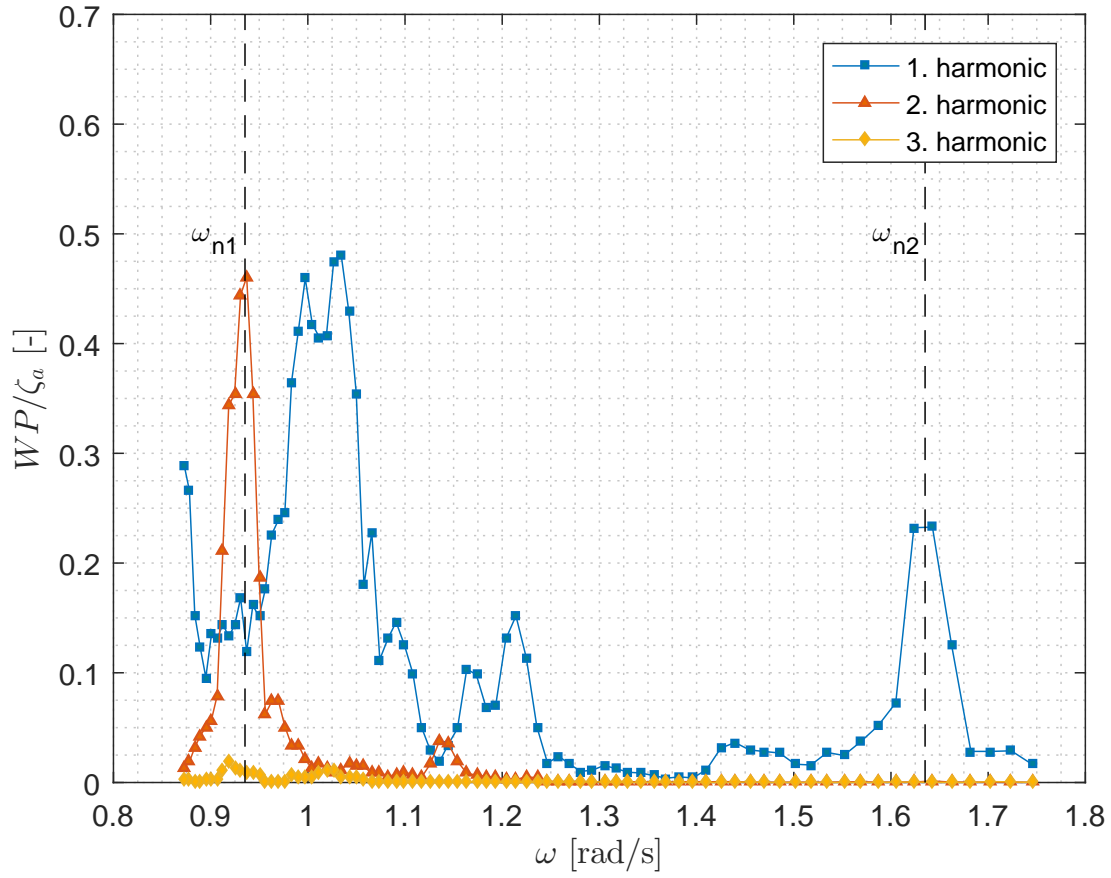
A.2.1   Wave Probe 1
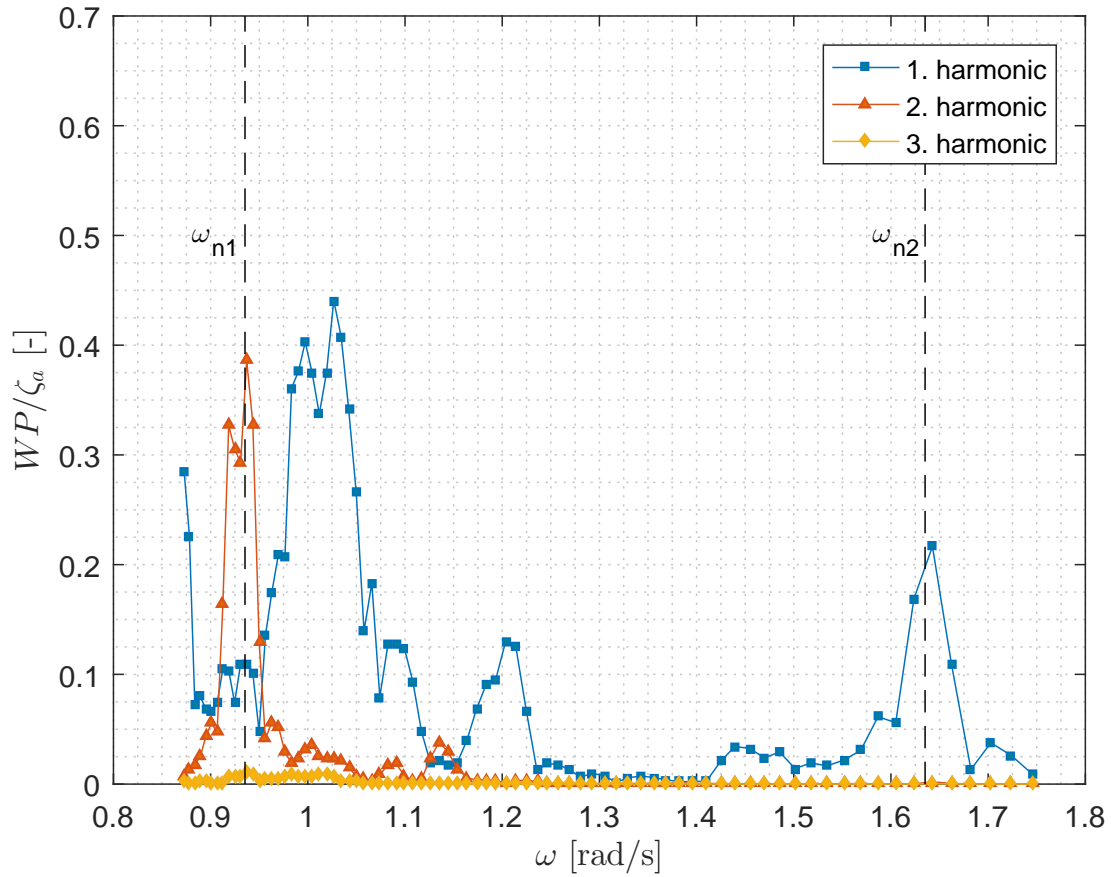
Figure A.5: RAOs for the first, second and third harmonics of the experimental body-fixed free-surface elevation at WP1 for wave steepness $H/\lambda = 1/60$. All the harmonic components are linearized by dividing with the incoming wave amplitude, ζ_a.
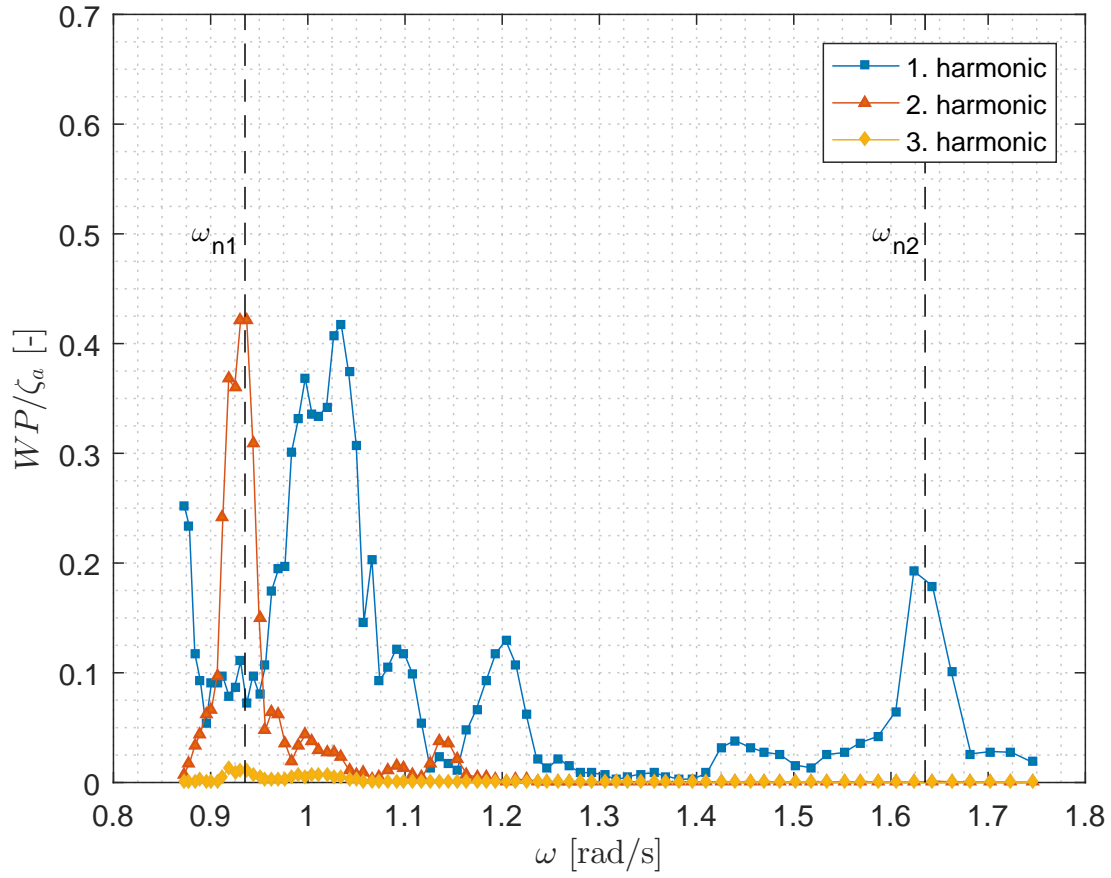
Figure A.6: RAOs for the first, second and third harmonics of the experimental body-fixed free-surface elevation at WP1 for wave steepness $H/\lambda = 1/45$. All the harmonic components are linearized by dividing with the incoming wave amplitude, ζ_a.
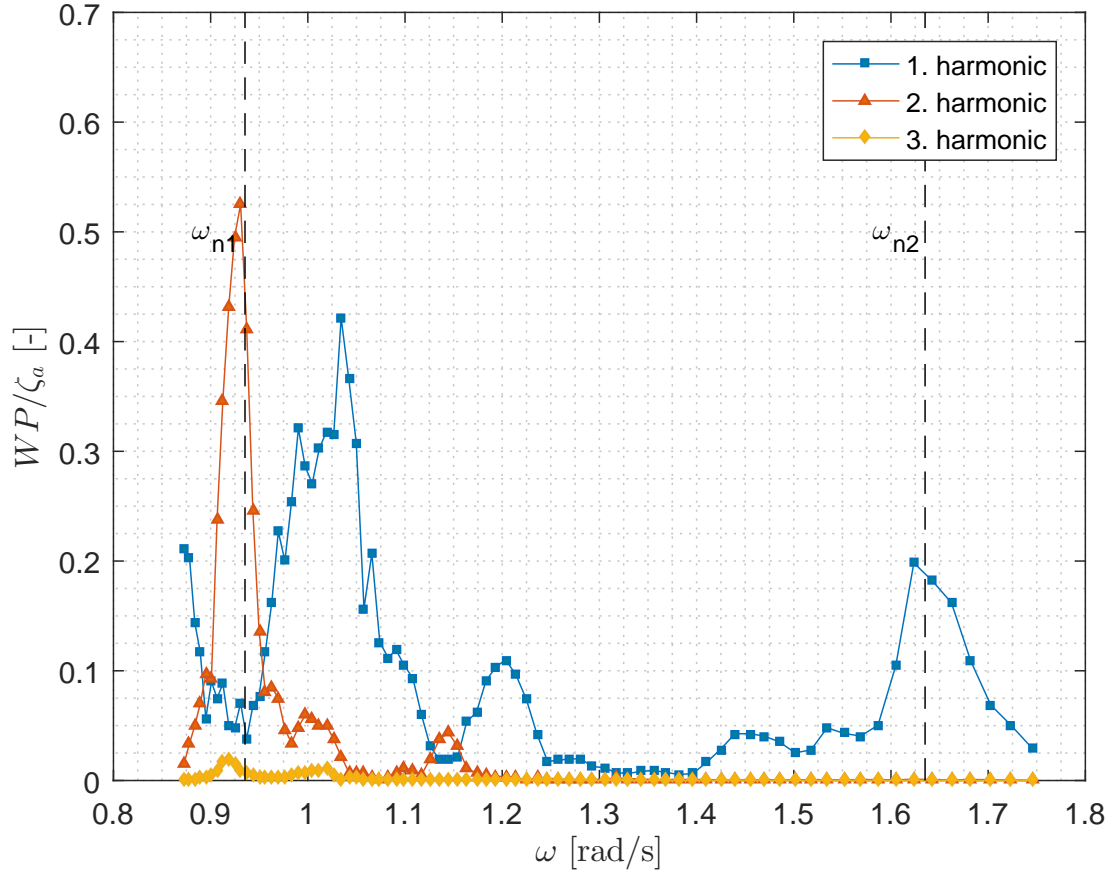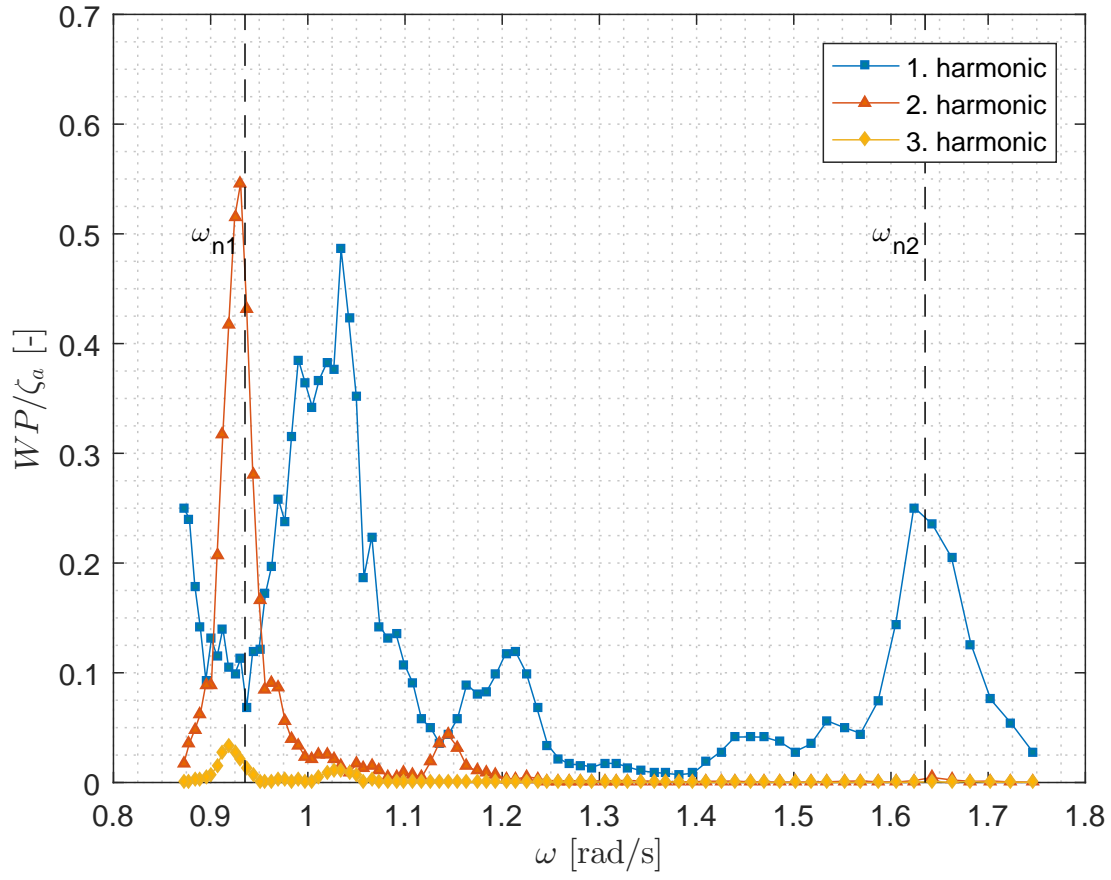
Figure A.7: RAOs for the first, second and third harmonics of the experimental body-fixed free-surface elevation at WP1 for wave steepness $H/\lambda = 1/30$. All the harmonic components are linearized by dividing with the incoming wave amplitude, ζ_a.
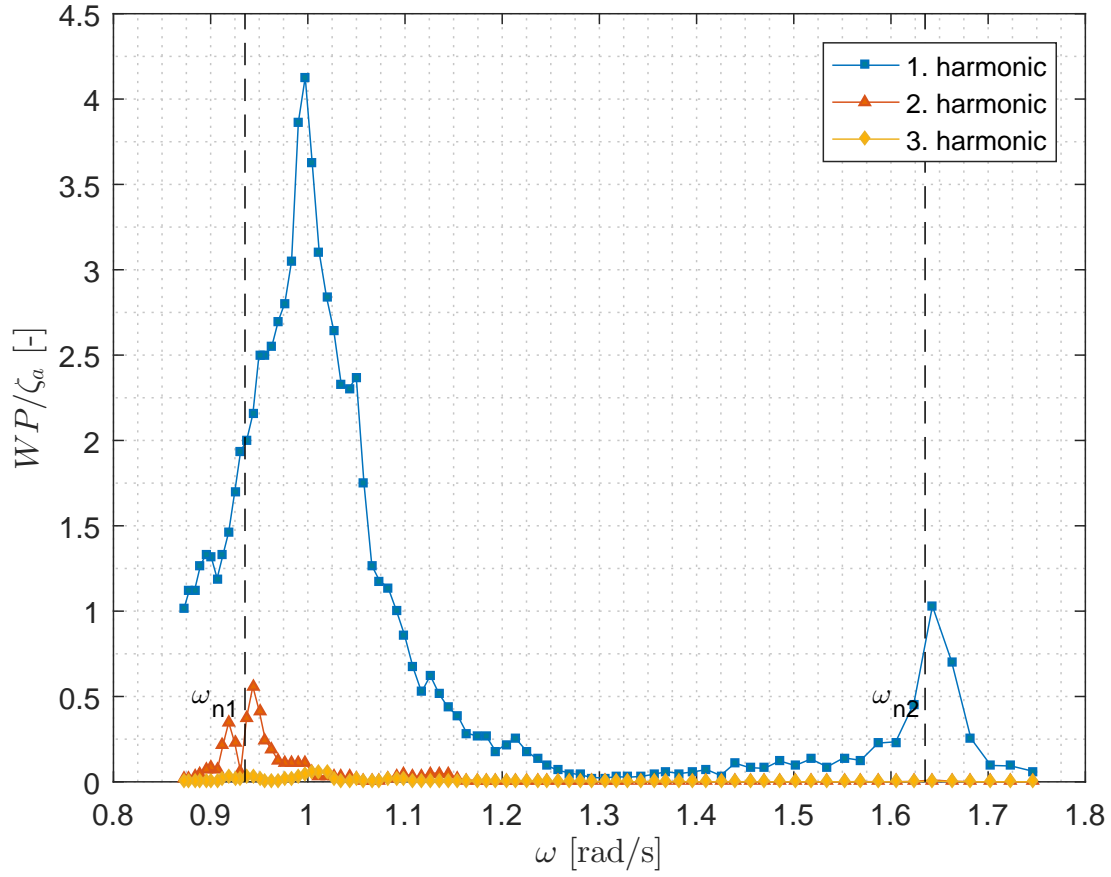
A.2.2   Wave Probe 2
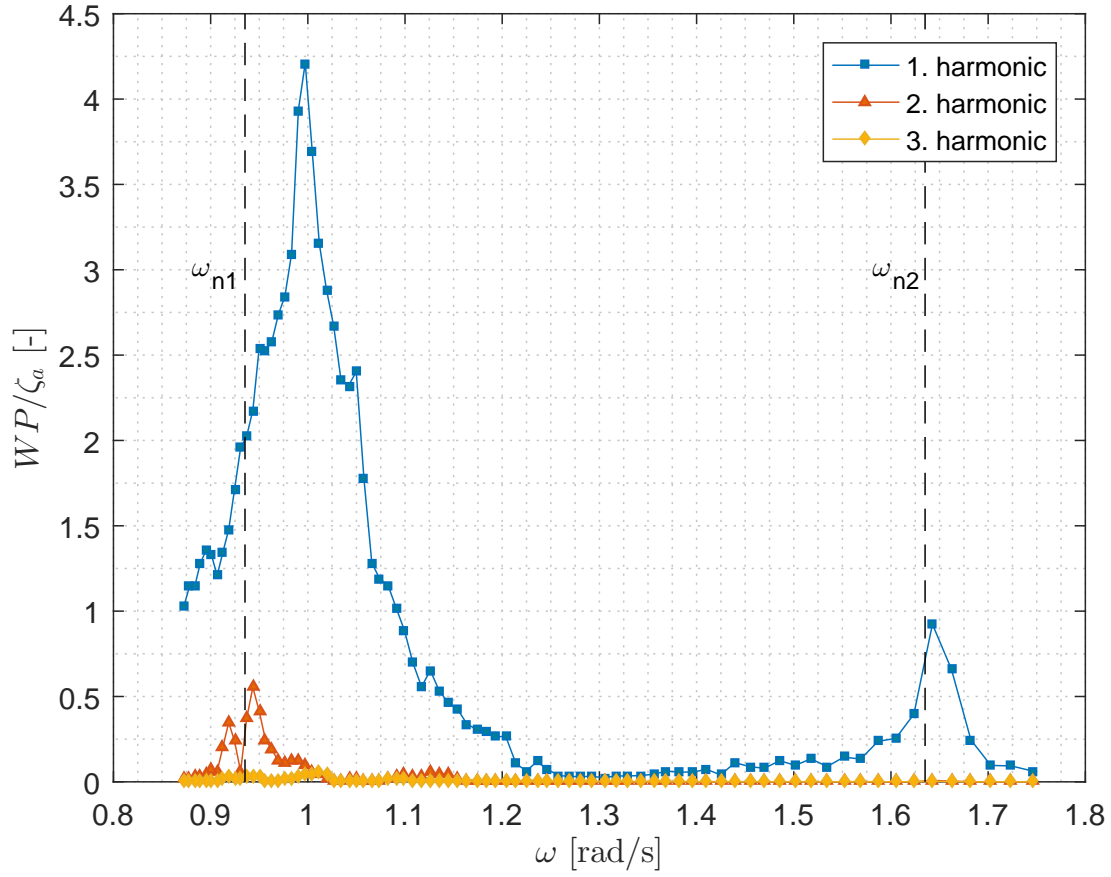
Figure A.8: RAOs for the first, second and third harmonics of the experimental body-fixed free-surface elevation at WP2 for wave steepness $H/\lambda = 1/60$. All the harmonic components are linearized by dividing with the incoming wave amplitude, ζ_a.
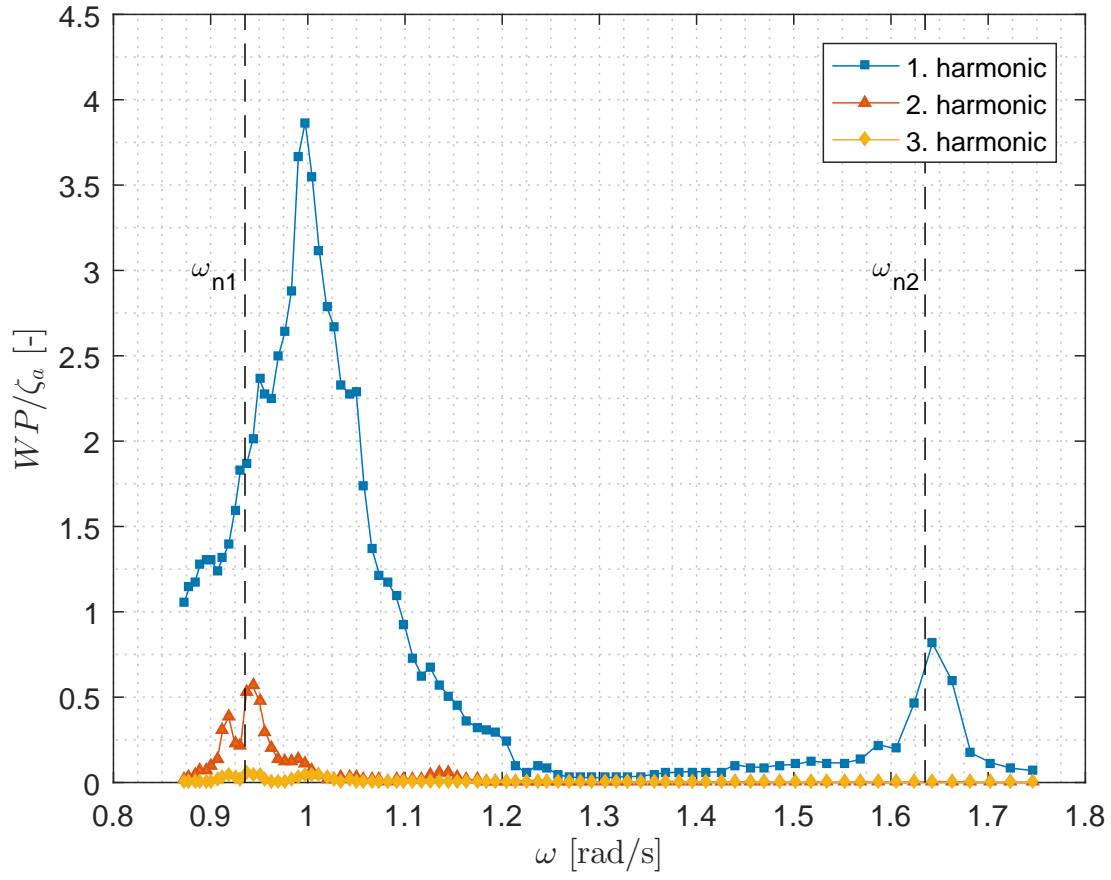
Figure A.9: RAOs for the first, second and third harmonics of the experimental body-fixed free-surface elevation at WP2 for wave steepness $H/\lambda = 1/45$. All the harmonic components are linearized by dividing with the incoming wave amplitude, ζ_a.
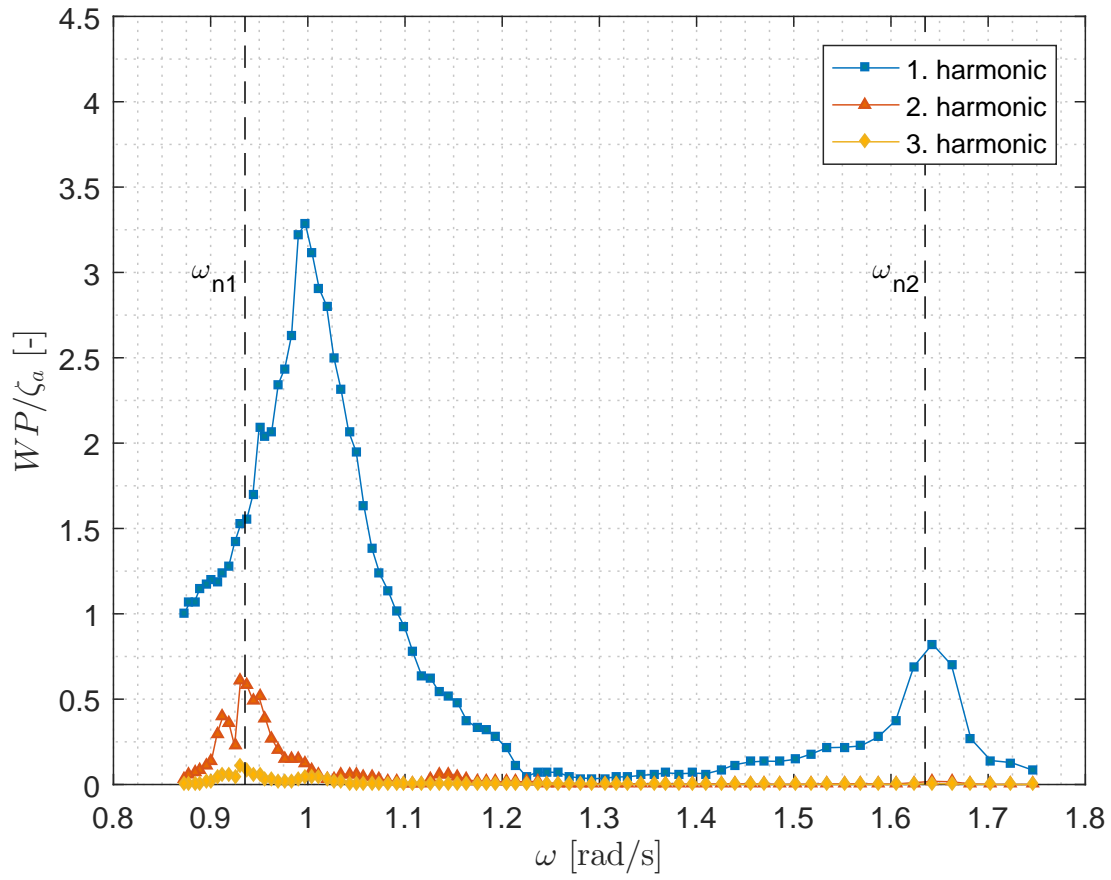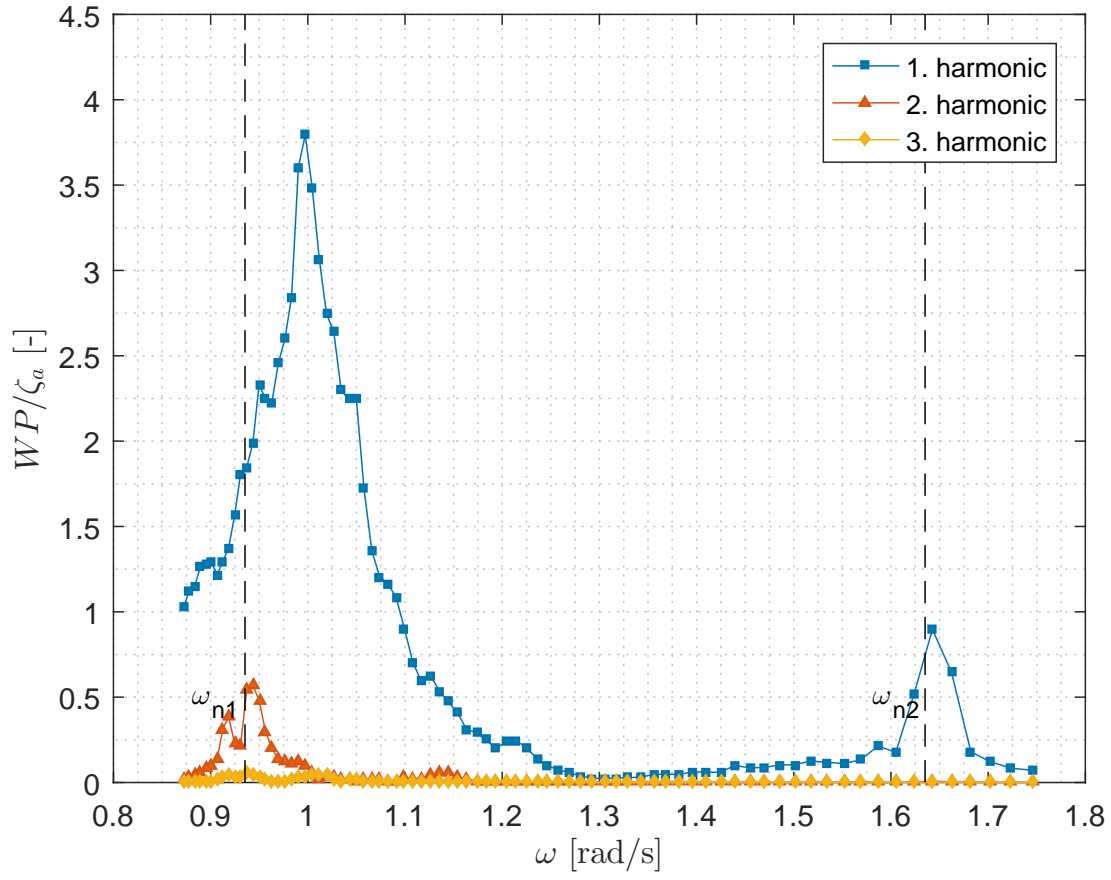
Figure A.10: RAOs for the first, second and third harmonics of the experimental body-fixed free-surface elevation at WP2 for wave steepness $H/\lambda = 1/30$. All the harmonic components are linearized by dividing with the incoming wave amplitude, ζ_a.
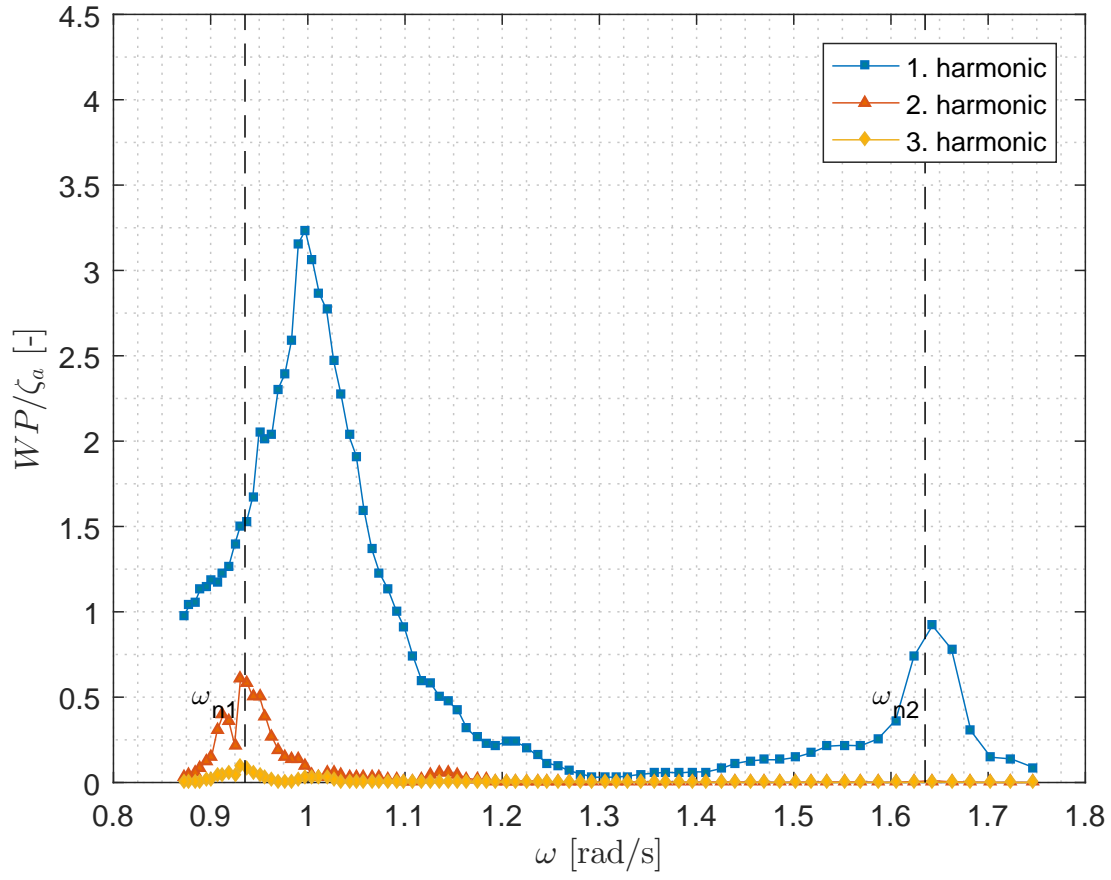
A.2.3   Wave Probe 3
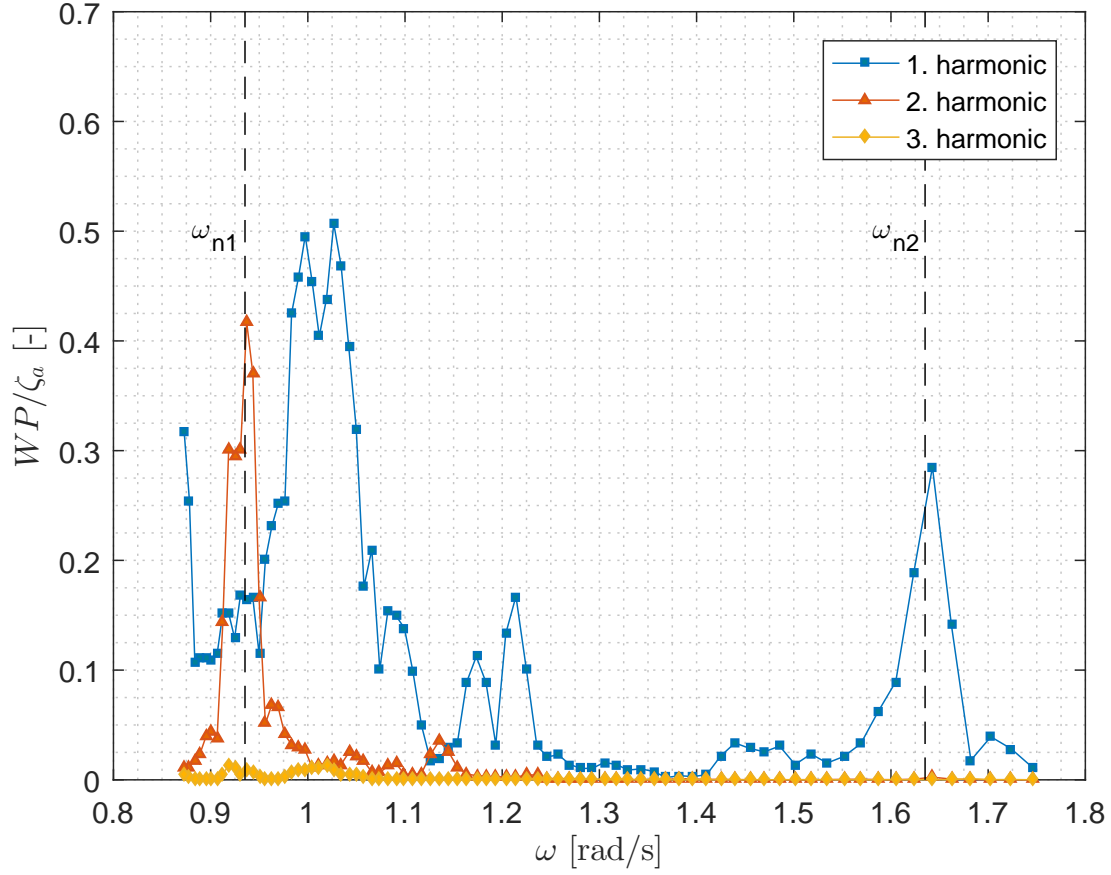
Figure A.11: RAOs for the first, second and third harmonics of the experimental body-fixed free-surface elevation at WP3 for wave steepness $H/\lambda = 1/60$. All the harmonic components are linearized by dividing with the incoming wave amplitude, ζ_a.

Figure A.12: RAOs for the first, second and third harmonics of the experimental body-fixed free-surface elevation at WP3 for wave steepness $H/\lambda = 1/45$. All the harmonic components are linearized by dividing with the incoming wave amplitude, ζ_a.
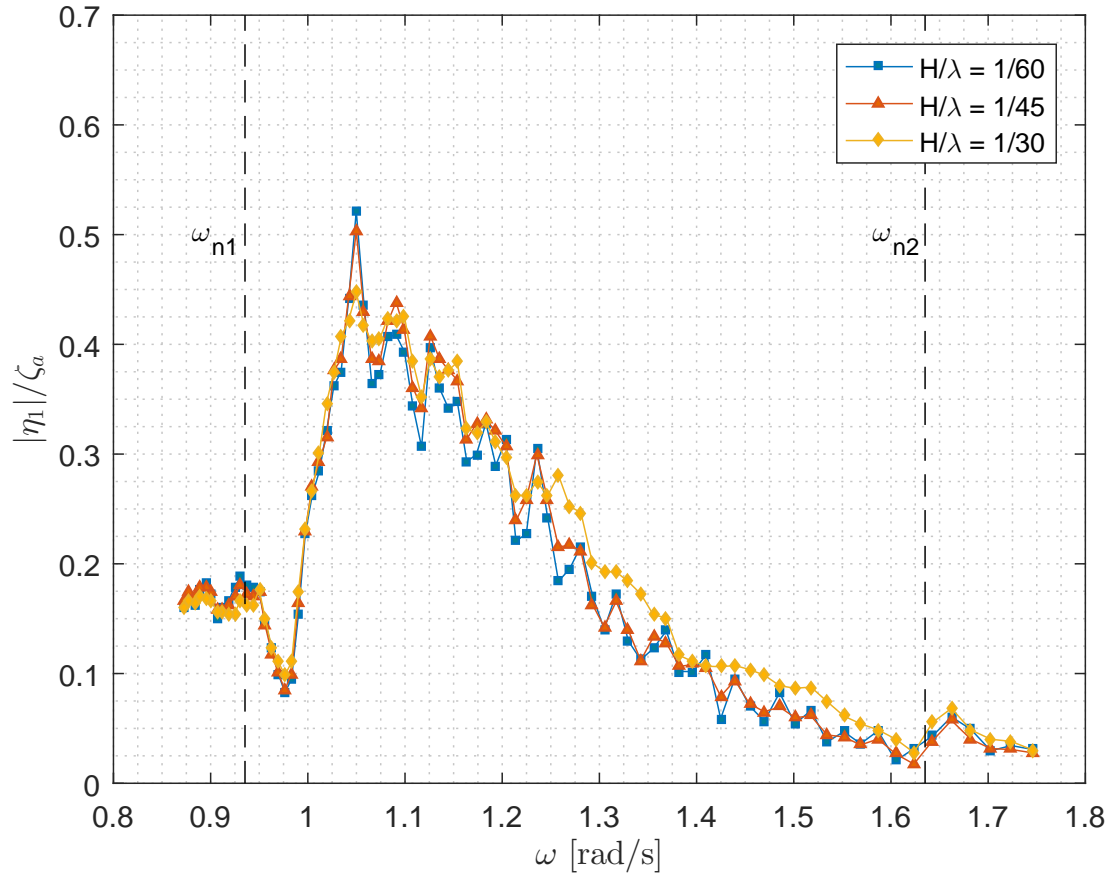
Figure A.13: RAOs for the first, second and third harmonics of the experimental body-fixed free-surface elevation at WP3 for wave steepness $H/\lambda = 1/30$. All the harmonic components are linearized by dividing with the incoming wave amplitude, ζ_a.

A.2.4   Wave Probe 4

Figure A.14: RAOs for the first, second and third harmonics of the experimental body-fixed free-surface elevation at WP4 for wave steepness $H/\lambda = 1/60$. All the harmonic components are linearized by dividing with the incoming wave amplitude, ζ_a.

Figure A.15: RAOs for the first, second and third harmonics of the experimental body-fixed free-surface elevation at WP4 for wave steepness $H/\lambda = 1/45$. All the harmonic components are linearized by dividing with the incoming wave amplitude, ζ_a.

Figure A.16: RAOs for the first, second and third harmonics of the experimental body-fixed free-surface elevation at WP4 for wave steepness $H/\lambda = 1/30$. All the harmonic components are linearized by dividing with the incoming wave amplitude, ζ_a.
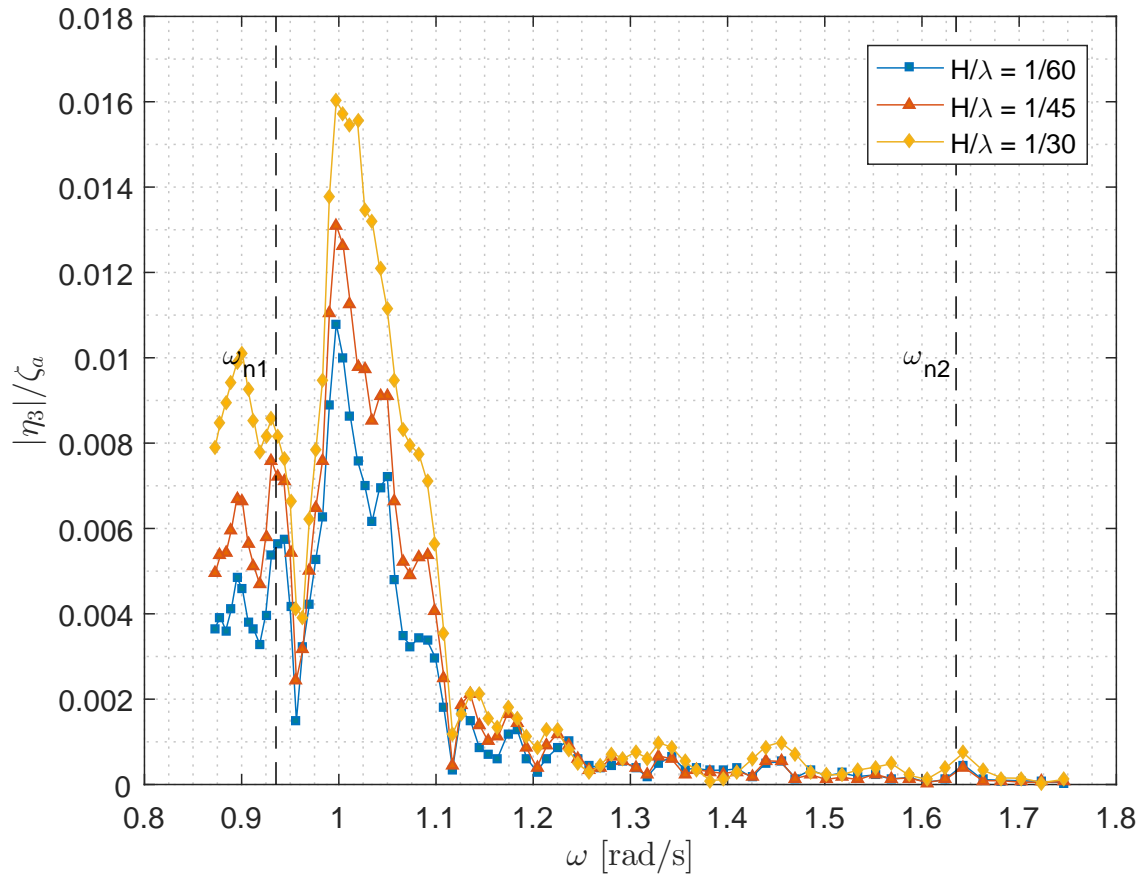
A.2.5 Surge

Figure A.17: RAOs for the first harmonic of surge for all the wave steepnesses.
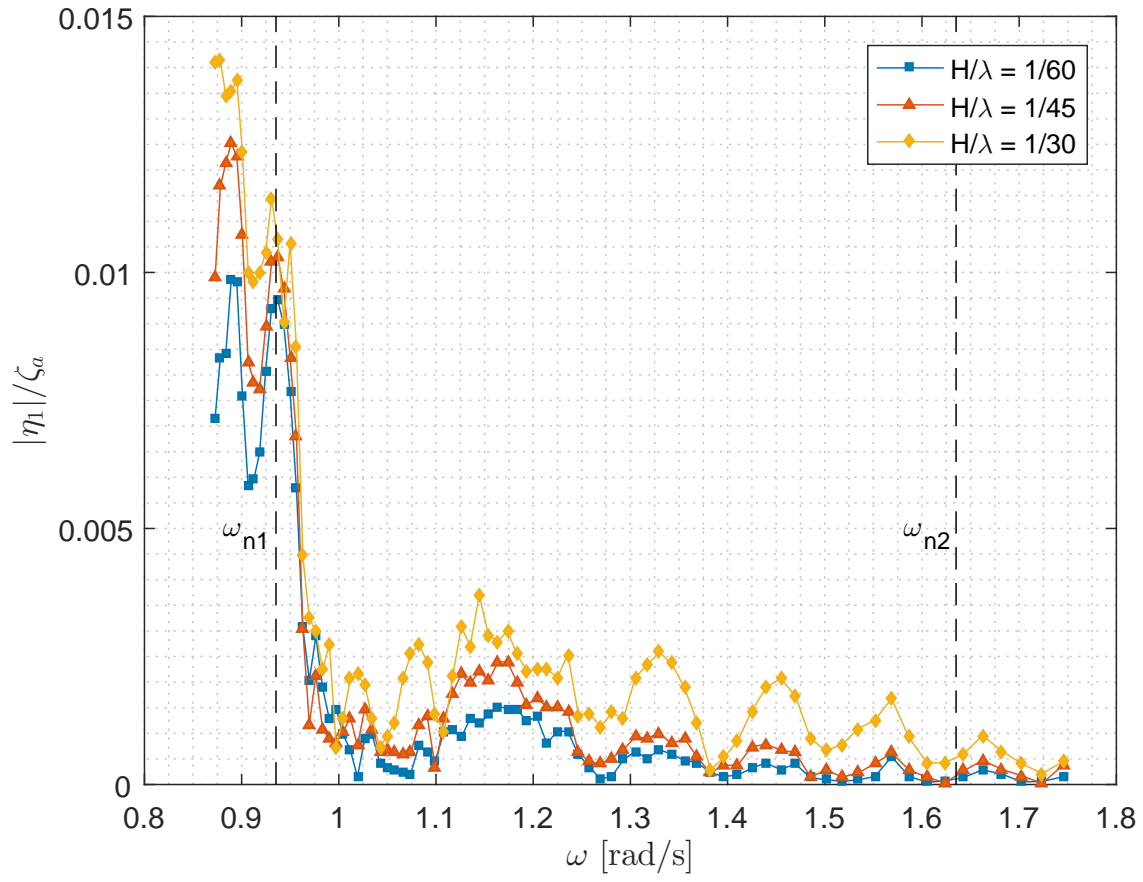
Figure A.18: RAOs for the second harmonic of surge for all the wave steepnesses.
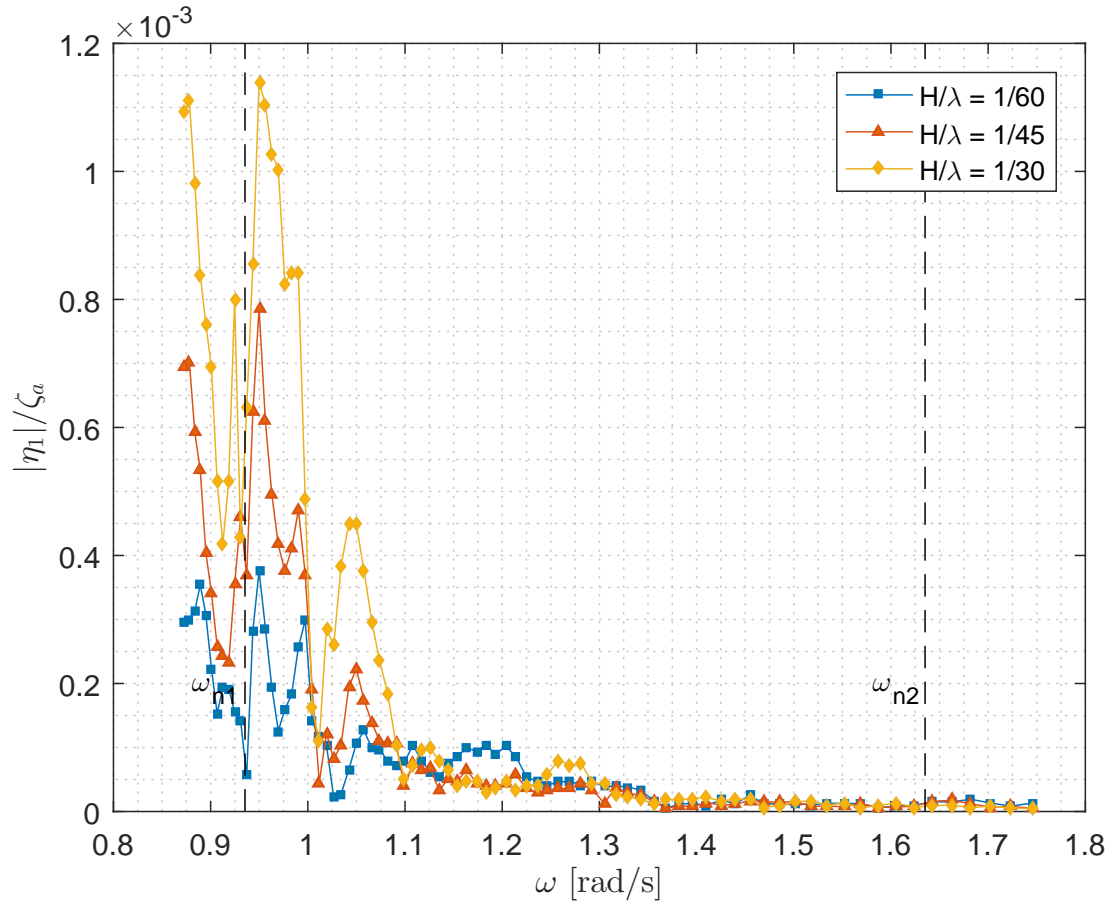
Figure A.19: RAOs for the third harmonic of surge for all the wave steepnesses.

A.2.6   Heave
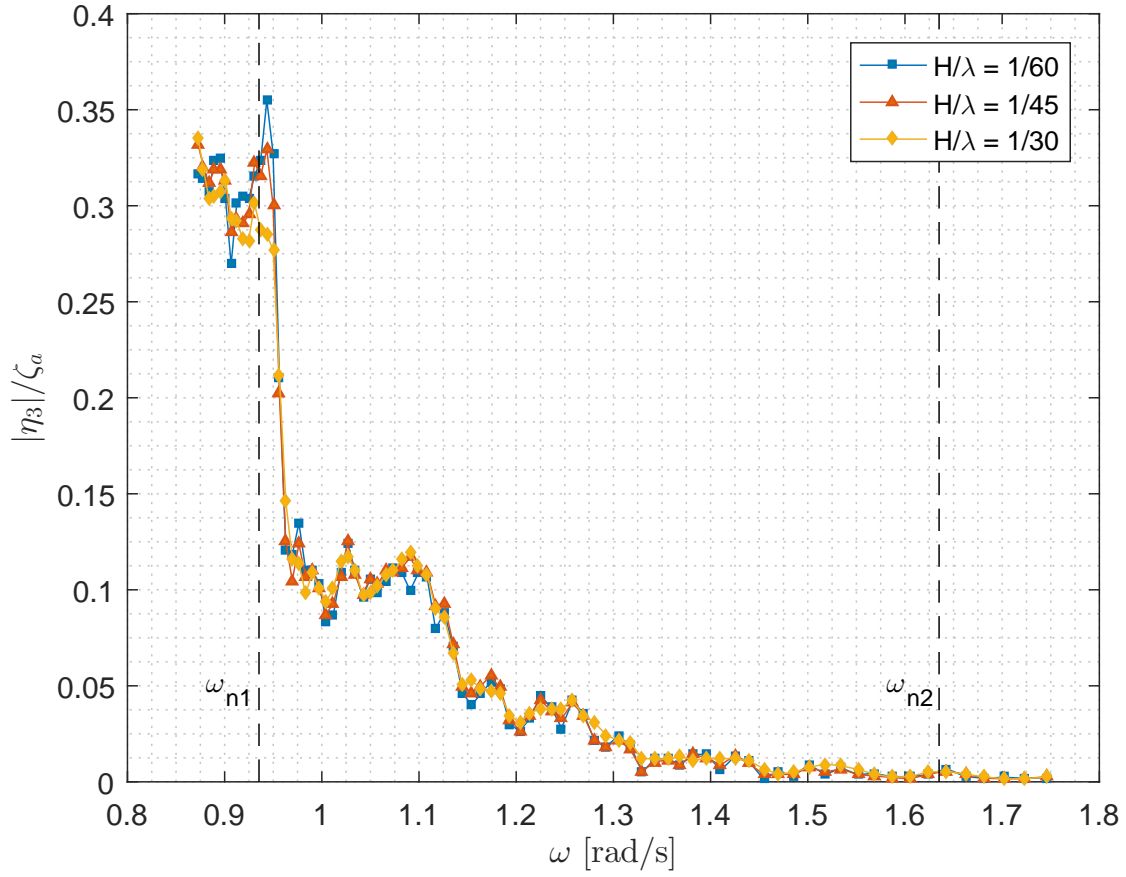
Figure A.20: RAOs for the first harmonic of heave for all the wave steepnesses.

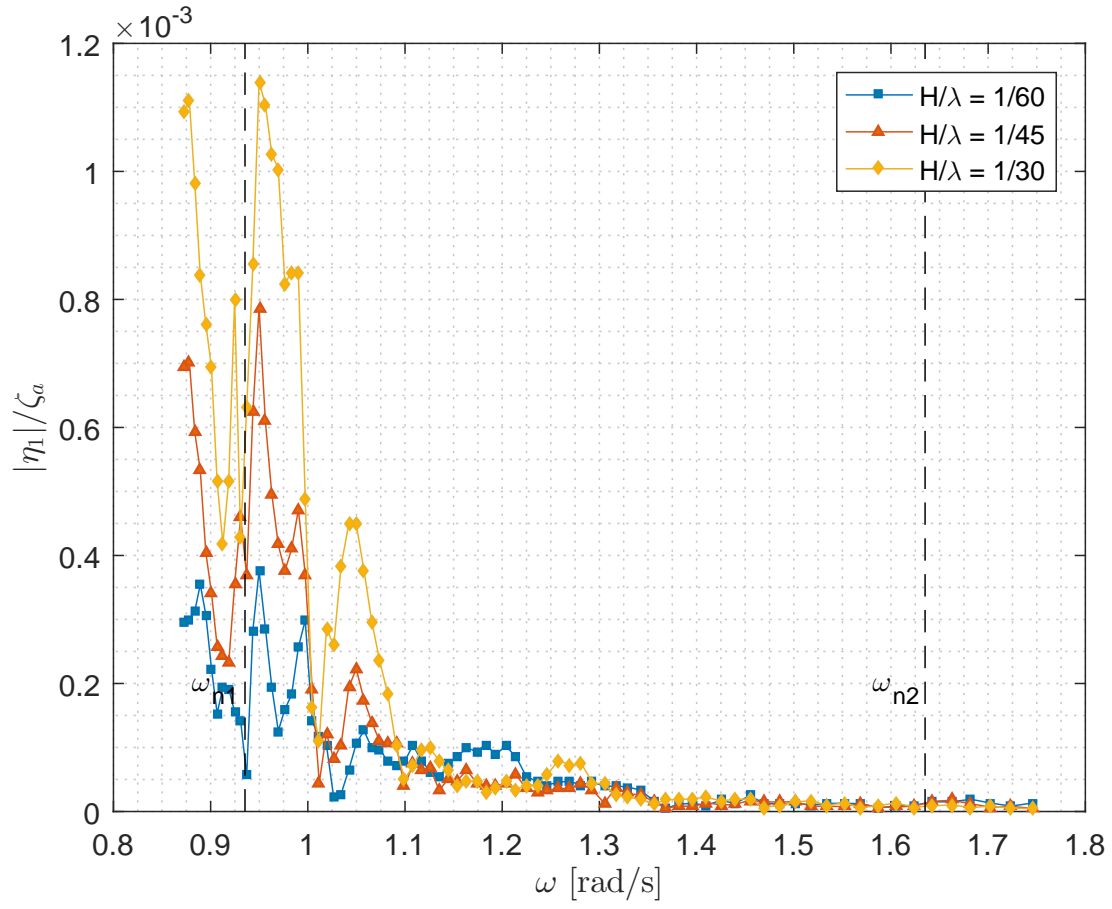Figure A.21: RAOs for the second harmonic of heave for all the wave steepnesses.

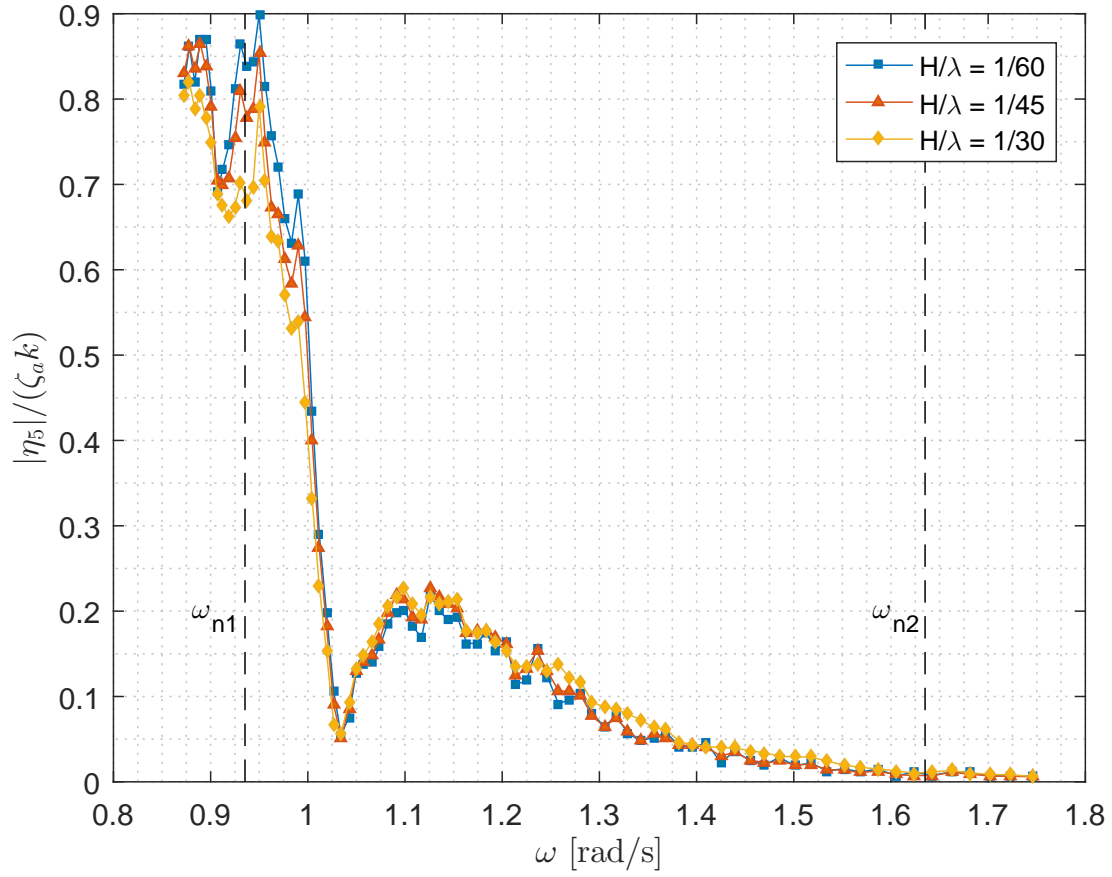Figure A.22: RAOs for the third harmonic of heave for all the wave steepnesses.

A.2.7   Pitch

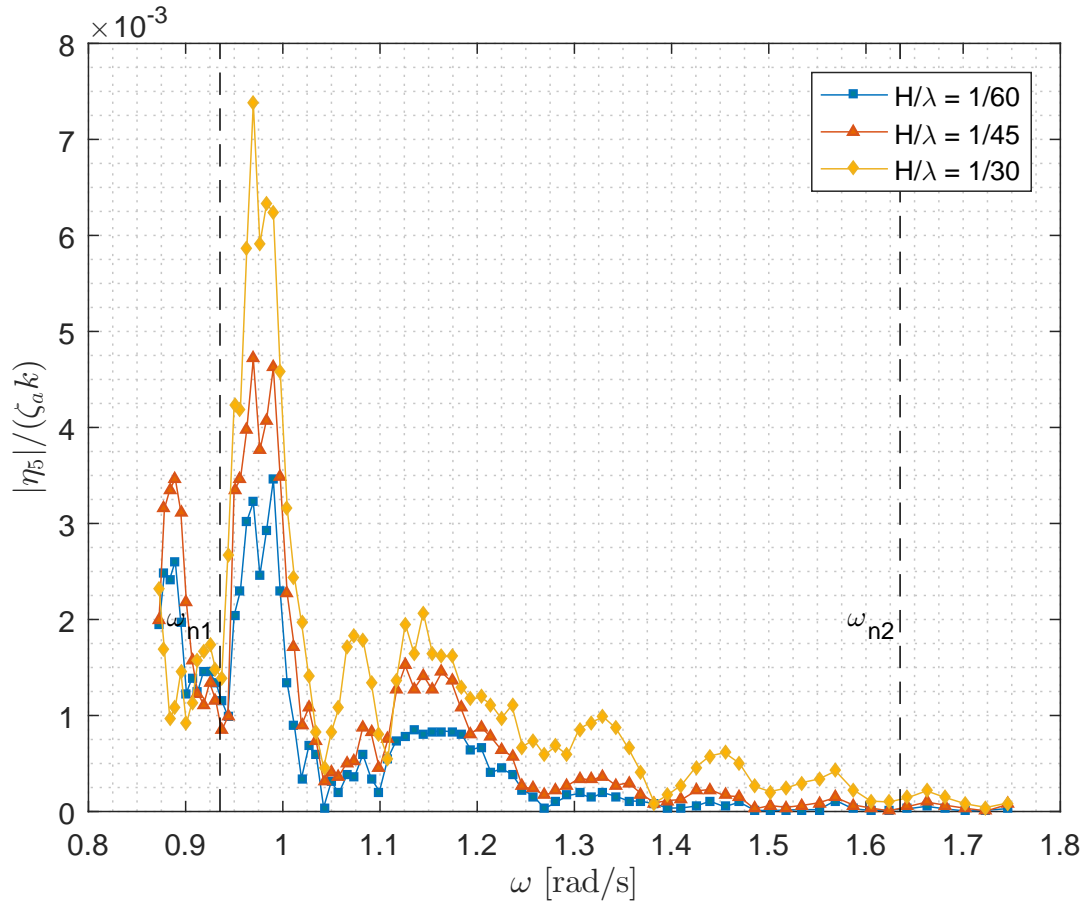Figure A.23: RAOs for the first harmonic of pitch for all the wave steepnesses.

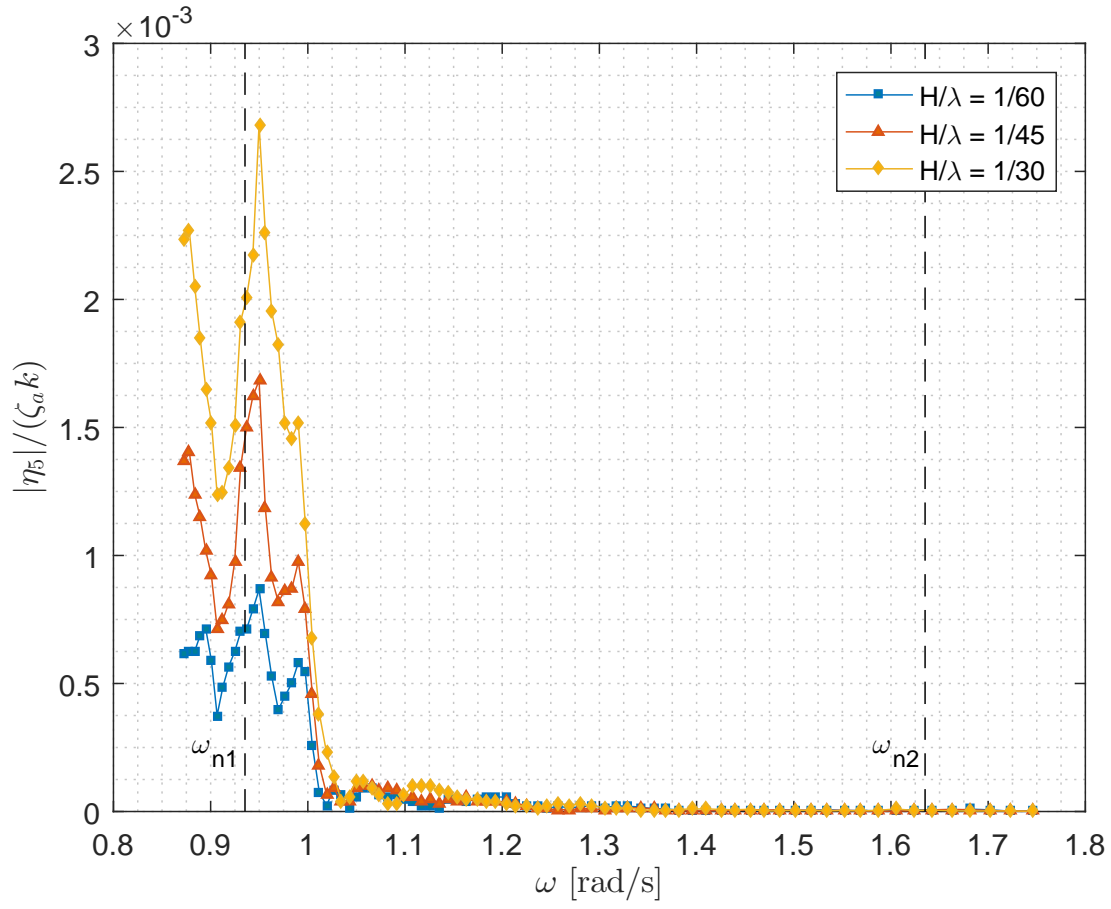Figure A.24: RAOs for the second harmonic of pitch for all the wave steepnesses.

Figure A.25: RAOs for the third harmonic of pitch for all the wave steepnesses.